

# The fouling behavior on PEEK surfaces during heat transfer

Vom Fachbereich Maschinenbau und Verfahrenstechnik  
der Rheinland-Pfälzischen Technischen Universität Kaiserslautern-Landau  
zur Erlangung des akademischen Grades

**Doktor-Ingenieur (Dr.-Ing.)**

genehmigte

**Dissertation**

vorgelegt von

M.Sc. Philipp-Lukas Laurentius Pelz

aus Gütersloh

Dekan: Prof. Dr. rer. nat. Roland Ulber

Prüfungskommission:

Prüfungsvorsitzender: Prof. Dr.-Ing. Fabian Jirasek

1. Berichterstatter: Sen. Prof. Dipl.-Ing. Dr. techn. Hans-Jörg Bart

2. Berichterstatter: Prof. Dr.-Ing. Erik von Harbou

3. Berichterstatter: Prof. Dr.-Ing. Stephan Scholl

Tag der mündlichen Prüfung: 04.06.2025

Kaiserslautern 2025

D386



# Abstract

Fouling in heat exchangers is a major challenge in many industrial processes due to increased energy costs, environmental pollution and shortened cleaning cycles. One strategy to avoid the growth of deposits is the use of alternative materials such as polyether ether ketone (PEEK) instead of the conventionally used stainless steel (SS). In this thesis, the fouling behavior of PEEK-based heat exchangers is therefore compared qualitatively and quantitatively with SS heat exchangers. The behavior of crystallization (calcium sulfate) and organic (whey protein concentrate, WPC) fouling are considered. The experimental studies show that PEEK has a lower susceptibility to fouling and better cleanability compared to SS under various process conditions, making it a promising material for preventing fouling. By modeling the fouling behavior of WPC, a deeper understanding of the process was achieved and predictions were made for the fouling behavior of non-tested operating conditions. In calcium sulfate solutions, PEEK exhibited asymptotic fouling behavior, with a fouling factor half that of SS, while talc-filled PEEK (TKT) had higher fouling rates due to increased surface roughness. Cleaning experiments confirmed the advantage of PEEK over SS, as deposits could be removed more quickly from the surface compared to SS. PEEK also showed a significant reduction in the effects of whey protein deposits, with up to a 40 percent reduction of heat resistance compared to stainless steel. The cause of the reduction in thermal resistance was the removal of the deposit layer caused by evaporation, so that the thermal resistance remained limited to PEEK surfaces and longer operating times were possible. Scale-up experiments confirmed that these results are scalable and showed consistent behavior. A mechanistic and an empirical model were developed to predict the deposition behavior. Both models were able to predict the experimental data well. The mechanistic model took into account protein denaturation and boiling effects and was able to extrapolate from the data better than the empirical model, even though significant deviations were observed during validation. The empirical model showed higher accuracy in predicting behavior under untested operating conditions within the limits of the experimental data compared to the mechanistic model. Symbolic regression further correlated the model parameters with operating conditions. These results show that PEEK heat exchangers reduce the costs associated with fouling and improve sustainability, making them a viable alternative to conventional materials in energy-intensive processes. The investigations show that PEEK is a competitive alternative to conventional stainless steels and can contribute to optimize processes.



# Kurzfassung

Die Bildung von Ablagerungen in Wärmeübertragern stellt aufgrund der erhöhten Energiekosten, der Umweltbelastung und den verkürzten Reinigungszyklen eine große Herausforderung in vielen industriellen Prozessen dar. Eine Strategie den Aufwuchs von Ablagerungen zu vermeiden, ist die Verwendung von alternativen Materialien wie Polyetheretherketon (PEEK) anstatt des herkömmlich verwendeten Edelstahl (SS). In dieser Arbeit wird daher das Ablagerungsverhalten von PEEK basierenden Wärmeübertragern mit SS Wärmeübertragern qualitativ und quantitativ verglichen. Hierfür werden Kristallisationsablagerungen (Calciumsulfat) und organische Ablagerungen (Molkenproteinkonzentrat, WPC) betrachtet. In den Studien zeigte sich unter verschiedenen Prozessbedingungen, dass PEEK im Vergleich zu SS eine geringere Anfälligkeit für Ablagerungen und eine bessere Reinigungsfähigkeit aufweist, was es zu einem vielversprechenden Material für die Vermeidung von Ablagerungen macht. Durch die Modellierung des Ablagerungsverhaltens von WPC konnte ein tieferes Verständnis des Prozesses erzielt und Vorhersagen für das Ablagerungsverhalten von nicht getesteten Betriebsbedingungen getroffen werden. In Calciumsulfat Lösungen zeigte PEEK ein asymptotisches Ablagerungsverhalten, bei dem der Ablagerungsfaktor halb so hoch war wie bei SS, während talkgefülltes PEEK (TKT) aufgrund der erhöhten Oberflächenrauheit höhere Ablagerungsraten aufwies. Reinigungsexperimente bestätigten den Vorteil von PEEK gegenüber SS, da sich Ablagerungen im Vergleich zu SS schneller von der Oberfläche entfernen ließen. Auch beim Molkenprotein zeigte PEEK eine signifikante Minderung der Auswirkungen von Ablagerungen, mit einer bis zu 40-prozentigen Verringerung des Wärmewiderstands im Vergleich zu Edelstahl. Ursache für die Verringerung des Wärmewiderstands war die durch Verdampfen verursachte Ablösung der Ablagerungsschicht, so dass der Wärmewiderstand auf PEEK-Oberflächen begrenzt blieb und längere Betriebszeiten möglich waren. Scale-up Experimente bestätigten die Übertragbarkeit dieser Ergebnisse und zeigten ein konsistentes Verhalten. Zur Vorhersage des Ablagerungsverhaltens wurde ein mechanistisches und ein empirisches Modell entwickelt. Beide Modelle konnten die experimentellen Daten gut vorhersagen. Das mechanistische Modell berücksichtigte die Denaturierung von Proteinen und Siedeeffekte und konnte aus den Daten besser Extrapolieren als das empirische Modell. Das empirische Modell zeigte eine höhere Genauigkeit bei der Vorhersage des Verhaltens unter nicht getesteten Betriebsbedingungen innerhalb der durch experimentelle Daten vorgegebenen Grenzen im Vergleich zum mechanistischen Modell. Die symbolische Regression korrelierte die Modellparameter weiter mit den Betriebsbedingungen. Diese Ergebnisse zeigen, dass PEEK-Wärmeübertrager die durch Ablagerungen verursachten Kosten senken und die Nachhaltigkeit verbessern, wodurch sie eine praktikable Alternative zu herkömmlichen Materialien in energieintensiven Prozessen darstellen. Die durchgeführten Untersuchungen zeigen, dass PEEK eine konkurrenzfähige Alternative zu herkömmlichen Edelstählen ist und einen Beitrag zu optimierten Prozessen liefern kann.



# Contents

<b>Abstract</b>	<b>I</b>
<b>Kurzfassung</b>	<b>III</b>
<b>1. Introduction</b>	<b>1</b>
<b>2. Comparing calcium sulfate fouling on polymeric and metal heat transfer surfaces</b>	<b>5</b>
2.1. Abstract . . . . .	5
Abstract . . . . .	5
2.2. Introduction . . . . .	5
2.3. Materials and Methods . . . . .	6
2.3.1. Experimental setup . . . . .	6
2.3.2. Materials . . . . .	10
2.3.3. Experimental procedure . . . . .	10
2.4. Results . . . . .	12
2.4.1. Standard Operating conditions . . . . .	12
2.4.2. Variation of process parameters . . . . .	14
2.4.3. Apparatus comparison and cleanability . . . . .	17
2.5. Conclusion . . . . .	19
<b>3. Whey protein fouling on polymeric heat exchangers</b>	<b>21</b>
Abstract . . . . .	21
3.1. Introduction . . . . .	22
3.2. Experimental setup . . . . .	22
3.3. Data Reduction . . . . .	23
3.4. Materials . . . . .	23
3.5. Experimental procedure . . . . .	24
3.6. Results . . . . .	24
3.7. Conclusions . . . . .	33
<b>4. Predicting the fouling behavior of whey protein concentrate in polymeric heat exchangers</b>	<b>35</b>
Abstract . . . . .	35
4.1. Introduction . . . . .	36
4.2. Modeling . . . . .	37
4.2.1. Mechanistic model . . . . .	37
4.2.2. Empirical model . . . . .	44

4.3. Experimental data . . . . .	44
4.3.1. Experimental setup . . . . .	44
4.3.2. Methods and materials . . . . .	45
4.3.3. Operating procedure . . . . .	45
4.3.4. Data post-processing . . . . .	46
4.3.5. Accuracy of the measurements . . . . .	46
4.3.6. Optimization . . . . .	47
4.3.7. Symbolic regression . . . . .	48
4.3.8. Parameter estimation . . . . .	48
4.3.9. Implementation . . . . .	49
4.4. Results . . . . .	49
4.5. Conclusions . . . . .	57
<b>5. Conclusion and Outlook</b>	<b>59</b>
<b>Nomenclature</b>	<b>61</b>
<b>References</b>	<b>71</b>
<b>Supplementary Information</b>	<b>71</b>
<b>A. Supplementary Information for Chapter 2</b>	<b>73</b>
A.1. Velocity Profiles . . . . .	73
A.2. Streamlines . . . . .	78
A.3. Mesh independence study . . . . .	84
A.4. Experimental CFD validation using PIV Laser . . . . .	84
<b>B. Supplementary Information for Chapter 3</b>	<b>93</b>
B.1. Velocity Profiles . . . . .	94
B.2. Streamlines . . . . .	100
<b>C. Supplementary Information for Chapter 4</b>	<b>107</b>
<b>Detailed Contributor Roles Taxonomy</b>	<b>111</b>
<b>Publication List</b>	<b>113</b>
Journal Articles . . . . .	113
Lectures and Speeches . . . . .	113
Conference Posters . . . . .	113
<b>Supervised Student Theses</b>	<b>115</b>
<b>Curriculum Vitae</b>	<b>118</b>

# 1. Introduction

Heat exchangers are ubiquitous in almost all chemical processes. Metals, such as stainless steel and copper, have been preferred materials for heat exchangers (HE) due to their favorable attributes such as high thermal and mechanical performance. However, these materials face challenges such as corrosion susceptibility, high weight and cost. A further problem in many chemical processes is the deposition of dissolved substances on the heat exchanger surface. The deposition results in a number of undesirable consequences that affect operating, capital, and environmental cost. Higher operational cost results from increased maintenance, frequent downtime to clean the heat exchanging surfaces and waste disposal [1]. The capital cost increases primarily due to the enlargement of heat exchanger surface area, which is implemented to mitigate the effects of fouling and provide a margin of safety to ensure continuous operation under fouling conditions. Additionally, capital expenditure rises as a result of shortened equipment life cycle, necessitating more frequent replacement. Fouling also increases environmental cost by increasing CO<sub>2</sub> emissions and the disposal of chemical cleaning agents commonly used to remove deposits [2]. Since many substances tend to form deposits when heated or cooled, fouling impacts almost all industrial branches. The diversity of fouling types, such as scaling, biological fouling, chemical reaction fouling, organic fouling and particle fouling, and their dependence on various operating parameters complicates the mitigation of fouling and the prediction of deposit behavior. Furthermore, fouling types can have distinct fouling mechanisms which may depend on various material properties such as roughness [3], surface energy [4] or thermal conductivity [5], which adds further complexity to understanding fouling processes. Consequently, the fouling resistance  $R_f$ , which represents additional heat resistance due to fouling, may exhibit varying behavior over time as shown in Figure 1.1. The degree of fouling resistance exhibited by a deposit is dependent on its structural integrity. Deposits that are weaker in nature typically display an asymptotic fouling resistance, whereas those that are harder and more resilient tend to display a linear or decreasing rate tendency. The first three curves in Figure 1.1 illustrate idealized conditions, while the saw-tooth pattern represents oscillations due to deposit break-off, as observed in some experimental and industrial data. Besides the main deposit growth phase, the figure illustrates an initiation phase and a roughness control phase, which may not be visible in experimental data [3]. The initiation or induction phase represents a period of delay between the initial contact of the fouling fluid and the heat exchanger wall and the subsequent onset of measurable fouling.

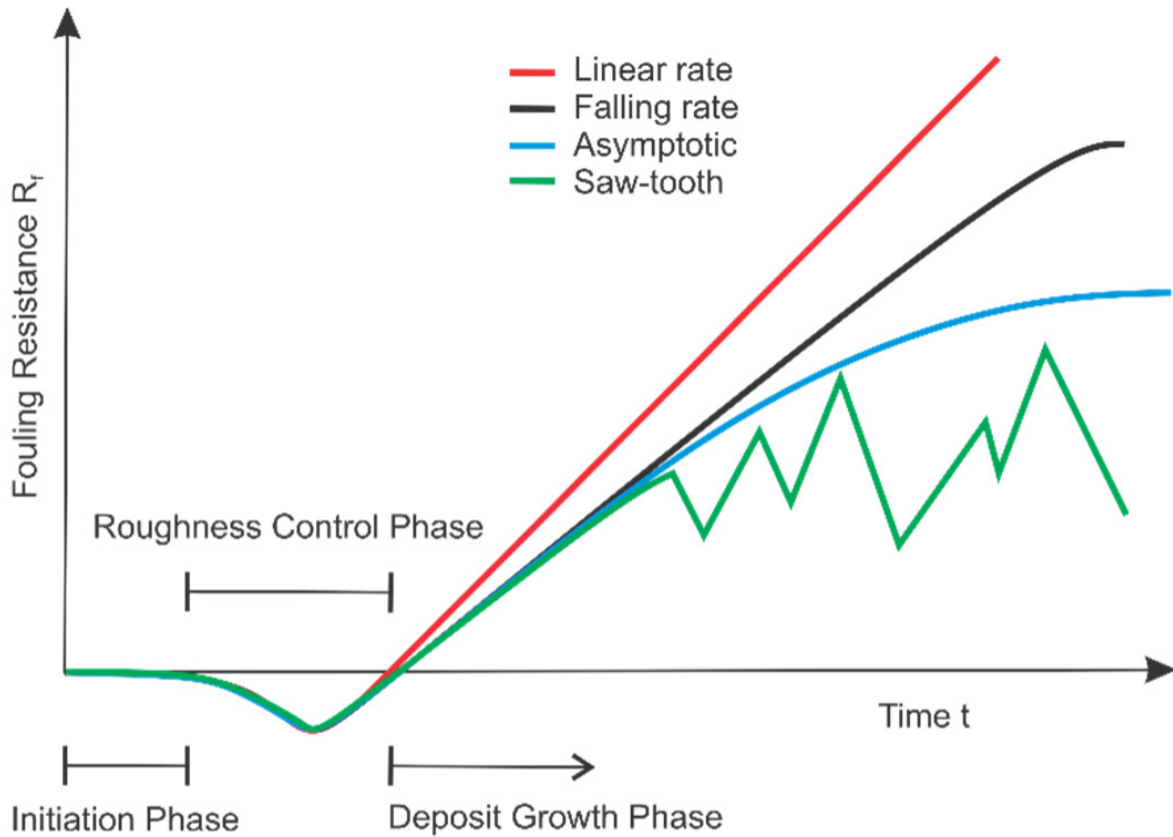


**Figure 1.1.:** Examples of typical fouling resistance curves [6].

Despite decades of research, understanding these mechanisms and developing effective mitigation strategies remains a critical area of investigation. In addition, as industries continue to push the limits of energy efficiency and process intensification, the demand for innovative materials and more efficient heat exchanger designs is growing, highlighting the need for a deeper understanding of fouling mechanisms and fouling mitigation strategies. However, developing effective mitigation strategies is complex because fouling is influenced by multiple factors, including fluid composition, surface characteristics, operating conditions, and environmental variables [7]. Traditional fouling control methods, such as mechanical scrubbing, and operational adjustments, which try to optimize flow dynamics [8], while effective in some cases, often have drawbacks, including high costs, environmental risks, and limited long-term effectiveness. The use of additives, such as polyamines, acrylamide or lead particles can be viable mitigation alternatives in some processes. The materials can reduce fouling in a number of ways, such as increasing the solubility of the fouling component, inhibiting the activity of the foulant or destabilizing an already existing fouling layer [3]. Multiple disadvantages arise from incorporating additives: the product usually needs an additional purification step to remove the additives, which can be cost intensive and additives are often harmful to the environment, which makes them unsuitable for a range of processes such as food processes. More recently strategies for fouling mitigation have focused on the development of antifouling coatings, surface modifications to alter wettability and reduce adhesion as well as the use of alternative heat exchanger materials that facilitate cleaning-in-place (CIP) procedures. In particular, polymeric materials offer several advantageous properties for reducing fouling,

including low susceptibility to corrosion, enhanced flexibility in design, and improved chemical resistance, making them promising candidates for fouling-resistant applications [9–11]. A major drawback for polymers is the poor thermal performance of these materials which has prohibited their widespread use. The thermal conductivity usually lies in the area of 0.1 to 0.5  $\text{W m}^{-1} \text{K}$  [12], which is roughly two orders of magnitude lower than that of metals [13]. Despite this disadvantage polymeric heat exchangers are used in highly corrosive environments, where expensive metal alloys would be needed otherwise, and have advantages due to a better cleanability in fouling susceptible systems. Another important disadvantage of using innovative heat exchanger materials to mitigate fouling is the resource-intensive experimental work required to confirm effectiveness for each specific fouling system. Since deposition mechanisms vary widely, different surface properties and therefore materials may be required for an effective mitigation. Therefore, the testing of a wide variety of materials is necessary to tailor the heat exchanger surface to the fouling type. This necessitates techniques to reduce the required experimental work. To address this, the testing time can be reduced by developing experimental setups that enable the simultaneous evaluation of multiple materials. Furthermore, operating conditions that accelerate or intensify fouling can further reduce the time required to assess material performance. Predictive modeling is another frequently used technology to support, compliment and reduce experimental testing by anticipating deposit formation and enabling more proactive maintenance strategies. Fouling modeling plays a critical role in addressing these challenges by providing a theoretical and computational framework for understanding and predicting fouling behavior. By simulating fouling behavior under different operating conditions, fluid properties, and material choices, it enables better design, optimization, and operation of heat exchangers. This reduces the need for costly trial-and-error approaches as well as the number of experiments required and allows for more effective implementation of fouling mitigation strategies. The objective of this thesis is to demonstrate that the utilization of polyether ether ketone (PEEK) based heat exchangers in fouling susceptible processes is a viable and competitive alternative to conventional steel materials. Therefore, the deposition behavior of two distinct fouling types, crystallization and organic fouling, is examined. An experimental setup is developed that allows the simultaneous testing of multiple materials. A range of process conditions are investigated using this setup and results are compared to benchmark stainless steel. Additionally, the thesis investigates cleanability of the mentioned materials and seeks to attribute fouling mechanisms to the specific surface properties of each material. In order to reduce the time required to gather experimental data, a predictive fouling model is presented, which estimates whey protein deposition on PEEK surfaces and aims to predict fouling behavior for unseen operating conditions.

Chapter 2 introduces a testing rig for the simultaneous testing of different materials and focuses on crystallization fouling, specifically calcium sulfate ( $\text{CaSO}_4$ ) fouling. This type of fouling presents significant challenges in salt water desalination plants and a range of chemical processes. Beside investigating the impact of various process conditions such as  $\text{CaSO}_4$  concentration, heat flux and velocity on the fouling behavior, a cleaning in place strategy is examined for each material. The scalability of the results is evaluated by comparing outcomes from two distinctly sized experimental setups. To address the challenges of employing a material based mitigation strategy, process conditions are chosen in a way that promotes fouling to

reduce the amount of time required to generate meaningful fouling behavior. This is achieved through over-saturation of  $\text{CaSO}_4$  as well as high wall temperatures.

Chapter 3 uses the previous chapter's setup to investigate whey protein fouling, a type of organic fouling. Whey is considered the main component that facilitates deposition in milk based products. Deposits contribute excessively to operational expenditure in the dairy industry, with fouling related cost as high as 80% of operational cost [1]. Similarly to the previous chapter the fouling behavior of the same materials is investigated under a range of process conditions, including heat flux and whey protein concentration. The scalability of the findings as well as implementing a cleaning in place strategy are also evaluated. As described in Chapter 2 the operating conditions are chosen to promote fouling with high wall temperatures and whey concentrations.

In Chapter 4 the data from the previous chapter is used to develop a mechanistic and an empirical model, which predict the behavior of whey protein fouling in PEEK heat exchangers. The models help to reduce the experimental effort needed to accurately describe the fouling behavior. Both models are trained on data from chapter 3 as well as on additional experiments that were conducted for this purpose. A set of validation experiments were carried out to verify predictions obtained through estimation of optimization parameters.

## 2. Comparing calcium sulfate fouling on polymeric and metal heat transfer surfaces

*Contributor Roles Taxonomy*

Philipp Pelz: conceptualization; data curation; investigation; methodology; visualization; writing – original draft; writing – review & editing

*Chapter redrafted after the following main publication:*

P. Pelz, J. Schulz, P. Mavaddat, C. Meyer, K. Jasch, S. Scholl, E. von Harbou, and H.-J. Bart "Comparing Calcium Sulfate Fouling on Polymeric and Metal Heat Transfer Surfaces," *Chem. Ing. Tech.*, 2024. DOI: <https://doi.org/10.1002/cite.202300216>.

### 2.1. Abstract

Fouling mitigation provides many challenges in process equipment, especially in heat exchangers. In this work, the fouling behaviors of two polymers are compared to 1.4301 stainless steel in calcium sulfate solutions. An experimental setup that allows to classify the materials quickly and under varying process conditions is used to determine the fouling behavior. Results are compared to a screening apparatus which can test up to 3 materials simultaneously. Lastly, the cleaning behavior of all three materials is investigated. Results show that polyether ether ketone (PEEK) is superior to SS in mitigating fouling and is easier to clean, however polyether ether ketone with 30% talcum (TKT) is not. This is attributed to the surface roughness of the materials.

### 2.2. Introduction

Crystallization fouling, also called scaling, is considered to be the most harmful form of fouling for heat exchangers (HX) [6]. Scaling occurs when dissolved salts precipitate on the HX surfaces. The precipitation follows the supersaturation of the salts in the solvent. This in turn may derive from a variation of pH, mixing solutions of different compositions, evaporation of the solvent, cooling or heating of the fluid. Whether heating or cooling leads to precipitation depends on the solubility behavior of the salts, which may decrease with lower temperatures (normal soluble salts, such as NaCl, CaCl<sub>2</sub>) or with higher temperatures (inversely soluble salts, such as CaSO<sub>4</sub>, CaCO<sub>3</sub>).

Common fouling mitigation strategies includes the selection of process parameters and the addition of fouling prohibiting chemicals. However, both strategies are often complicated to implement or not feasible due to economic or process quality constraints. Consequently, alternative materials, such as PEEK, are needed to provide stable and reliable heat transfer in fouling susceptible systems.

Crystallization fouling is a relatively slow process, which makes measurements traditionally extremely time consuming. Experimental runs can last up to multiple days [14, 15], which provides challenges to gather reproducible and reliable data. Furthermore, the crystallization mechanisms are not completely understood [16], which prevents general statements of the impact of material surface properties such as roughness or free surface energy on fouling behavior.  $\text{CaSO}_4$  fouling on PEEK surfaces has been previously investigated by Dreiser and Bart [11]. However, to the authors knowledge, no research on flow channels and short experimental run times have been conducted. This chapter therefore focuses on assessing the suitability of novel HX materials and their abilities to mitigate calcium sulfate fouling. For this purpose, two PEEK surfaces and benchmark stainless steel 1.4301 (SS) are used. The materials can be mounted into a flow channel, which is the main part of the experimental setup that monitors the fouling behavior under varying process conditions of Reynolds number, heat flux and  $\text{CaSO}_4$  concentration. High heat flux and supersaturated  $\text{CaSO}_4$  solutions are used to reduce the run time to a maximum of 20 hours. In order to obtain results quicker a smaller, bench-top sized screening apparatus is used that allows the simultaneously testing of up to 3 materials. With these two setups it is possible to evaluate if a similar fouling behavior can be obtained under different geometrical constraints.

## 2.3. Materials and Methods

### 2.3.1. Experimental setup

The experimental setup is shown in Figure 2.1. A 60-liter tank is used as a bulk fluid reservoir. A constant fluid flow is maintained via a flow meter-controlled pump, (MPN170, Schmitt Kreiselpumpen GmbH & Co. KG, Ettlingen, Germany). The liquid is then transported to either the screening channel (1) or the main channel (2), where the fluid contacts the heat transferring materials. Before the fluid is fed back into the tank a temperature-controlled thermostat (Lauda RP 1845, Lauda Dr. R. Wobser GmbH & Co. KG, Lauda-Königshofen, Germany) ensures that the bulk fluid temperature remains constant throughout the experiment. Construction details of the channels can be found in Figure 2.2. The main channel (b) features a single copper block (3) of 100 mm by 90 mm length and 25 mm depth, giving a total heat transferring surface of 90 cm<sup>2</sup>. Two bore holes were drilled through the block to facilitate heating cartridges (550 W, 100 mm, 6 mm diameter, Resistencias Industriales Maxi watt S.L, Elche, Spain) and 6 PT100 (9) thermocouples (class A, 4-wire, 50 mm length, 3 mm diameter) measure temperatures throughout the block. A 10mm thick insulation frame (4) was manufactured to ensure that the produced heat is transferred only into the liquid. The tested materials are placed between the two halves of channel (7,8), covering the whole

length of the flow channel. The cross-flow area is of 7 mm height and 116 mm width and has a length of 549 mm. Each channel half has an o-ring running along its circumference to provide sealing. A polymethylmethacrylate (PMMA) lid (6) allows for visual inspection of the fouling process.

The screening apparatus (a) consists of a 3D printed PVDF inlet and outlet as well as a central PEEK channel cell. The inlet (1) contours over 80 mm from the 3/4" nozzle to the 116 mm by 7 mm crossflow area of the channel, which is followed by a 113mm inlet length to ensure a developed fluid flow. The heat exchanger materials are located in the central channel cell (5), which connects to the inlet. Up to 3 materials can be tested simultaneously. Each probe is heated with a copper block (3) of 80 mm length, 20 mm width and 29 mm depth, giving a total heat transferring surface of 16 cm<sup>2</sup>. The heating blocks have two bore holes for heating cartridges (350 W, 80 mm, 6.5 mm diameter, Resistencias Industriales Maxi watt S.L, Elche, Spain), as well as 3 evenly spread holes that hold PT100 (9) thermocouples (Class A, 4-wire, l = 50 mm, d = 3 mm). The cartridges provide a constant heat flux, which is controlled via a eurotherm controller. The tested materials are placed above the copper blocks and are fixated with sealing tape (4411N, 3M, Saint Paul, USA), which also prevents contact between the liquid and the copper block. The copper blocks are seated inside a 1 cm thick insulation frame (4). The outlet (2) has a length of 60 mm and then contours back over a length 67 mm to the 3/4" nozzle. The fouling process can be observed through a PMMA lid (6). The screening apparatus was also used by Meyer, Pelz, Jasch, Bart, Harbou, and Scholl [17] to investigate the fouling behavior of surface treated metals. The main dimensions of the two channels can be found in Tab. 2.1. Figure 2.3 shows a photograph capturing the experimental setup as implemented. Since the hydrodynamics influence fouling behavior, it is essential to ensure that material samples experience similar flow conditions. This is particularly important for the screening channel where variations along the width of the channel may lead to differing flow characteristics. The Computational Fluid Dynamics (CFD) Software ANSYS Fluent was used to estimate flow conditions in the screening channel. Figure 2.4 shows the velocity across the width of the channel at a Reynolds number of 2000. Due to the symmetry of the channel only one half of the channel needs to be investigated. Results show that the fluid velocities are similar across the channel width at  $Re = 2000$ . For higher Reynolds numbers larger deviations in velocity occur across the channel width(s. Chapter A). Therefore, at  $Re = 8000$  the center heating block not used to ensure comparability between the samples. The CFD model was experimentally validated using a Particle Imaging Velocimetry (PIV) Laser (s. Chapter A), which showed good agreement with the model, with velocity deviations around 9% above the probes.

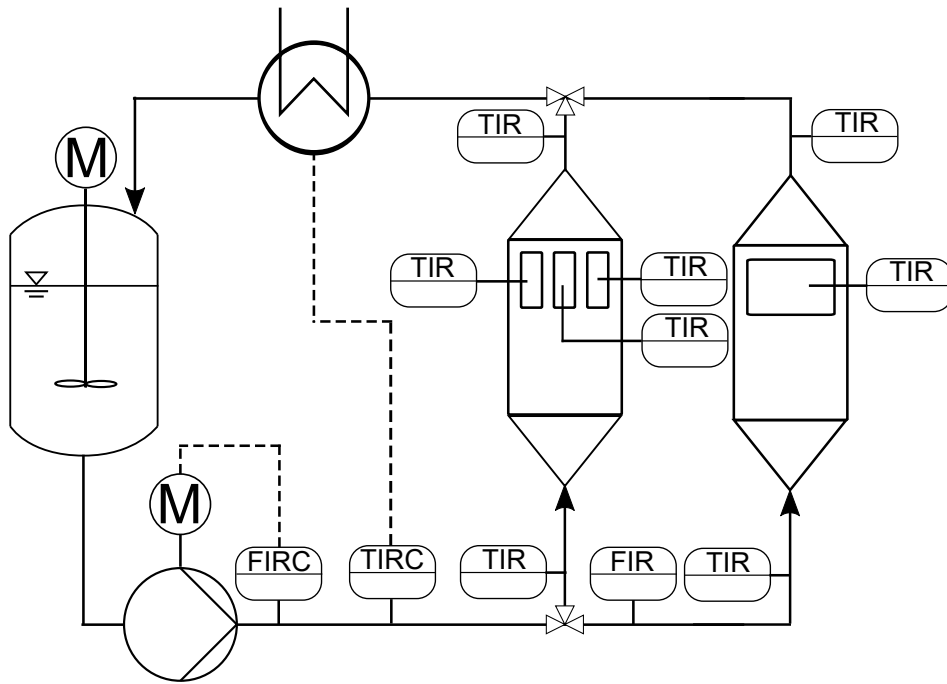


**Figure 2.1.:** Process flow diagram of the used experimental setup with screening channel (1) and main channel (2).

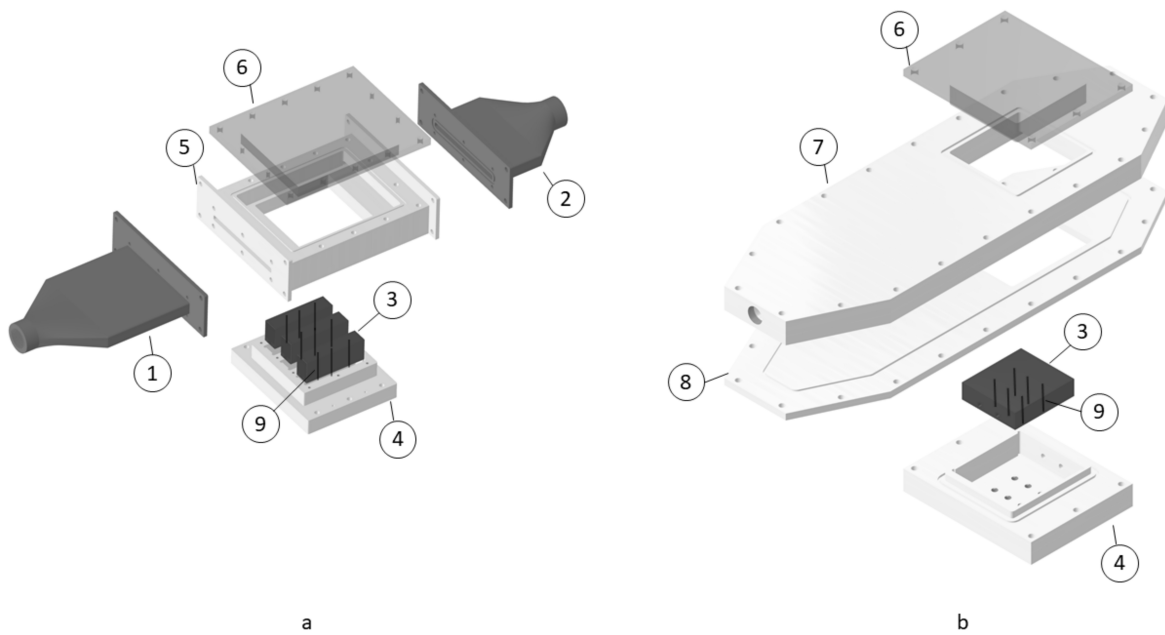


**Figure 2.2.:** Set up of the screening channel (a) and scale-up channel (b) with inlet (1), outlet (2), copper blocks (3), heating insulation (4), channel cell (5), lid (6), upper channel half (7), lower channel half (8) and temperature sensors (9).

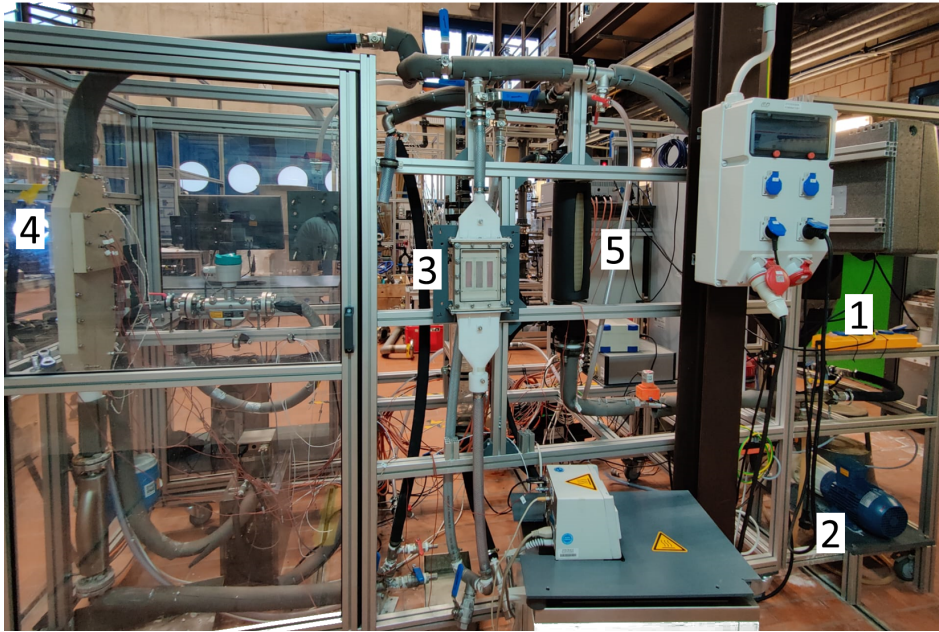


**Figure 2.3.:** Photograph of the experimental setup consisting of a tank (1), a pump (2), the screening (3) and scale-up (4) channel and a heat exchanger (5) to maintain bulk temperature during operation.

**Table 2.1.:** Dimensions for screening and scale-up channel.

Parameter	Screening channel	Scale up channel
Inlet length [mm]	193	395
Outlet length [mm]	127	154
Inlet/outlet diameter [inch]	3/4	3/4
Channel height [mm]	7	7
Channel width [mm]	116	116
Probe width [mm]	20	90
Probe length [mm]	80	100
Copper block width [mm]	20	90
Copper block length [mm]	80	100
Copper block height [mm]	29	25

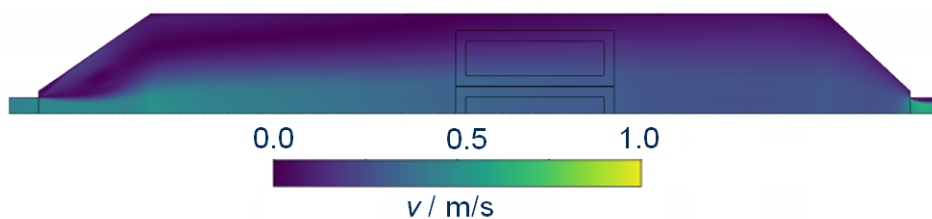


**Figure 2.4.:** Velocity profile across screening channel at  $Re = 2000$ .

### 2.3.2. Materials

Investigated heat transfer materials are a PEEK variant called LITE TK (henceforth PEEK), a talcum added PEEK (30% talcum) called LITE TKT30 (henceforth TKT) and 1.4301 stainless steel (SS). Relevant material properties are listed in Table 2.2. The polymers were obtained from Lite GmbH, Waidhofen a.d. Ybbs, Austria, and the SS from Record Metallfolien GmbH, Mühlheim am Main, Germany.

Since  $\text{CaSO}_4$  solubility is low, dissolving it is extremely time consuming. Therefore, the  $\text{CaSO}_4$  solution was obtained by mixing  $\text{Ca}(\text{NO}_3)_2 \cdot 4\text{H}_2\text{O}$  and  $\text{Na}_2\text{SO}_4$  (both purchased from Carl Roth GmbH + Co. KG), as reported by other researchers [18–22]. This is possible as  $\text{CaSO}_4$  is the only inversely soluble salt in the mixture, which prevents the precipitation of the other salts.  $\text{CaSO}_4$  can precipitate in three different forms: as anhydrite ( $\text{CaSO}_4$ ), hemihydrate ( $\text{CaSO}_4 \cdot 0.5 \text{H}_2\text{O}$ ) and dihydrate ( $\text{CaSO}_4 \cdot 2 \text{H}_2\text{O}$ ), each having a different solubility at a given temperature. Even though anhydrite is the least soluble, and should therefore mainly precipitate, its nucleation is considered a slow process [23] and gypsum was found to be primarily depositing [24].

**Table 2.2.:** Material properties [9].

Material	Thickness $\mu\text{m}$	Thermal conductivity $\text{W m}^{-1} \text{K}$	Surface free energy $\text{mN m}^{-1}$	Roughness $S_a$ $\mu\text{m}$	Roughness $S_q$ $\mu\text{m}$
PEEK	25	0.25	40.57	0.06	0.08
TKT	35	0.43	43.55	0.59	0.74
SS	25	15.00	32.38	0.13	0.16

### 2.3.3. Experimental procedure

Each experiment was started by placing an unused sample of the investigated material on the heating block. The surface was cleaned with isopropanol to prevent dust or other materials to contaminate the surface. Then deionized water was heated to  $30^\circ\text{C}$  and  $\text{Na}_2\text{SO}_4$  was dissolved in the water. The heating cartridges were set to the desired heat flux and switched on. After reaching thermal equilibrium,  $\text{Ca}(\text{NO}_3)_2 \cdot 4\text{H}_2\text{O}$  was stoichiometrically added to reach the desired  $\text{CaSO}_4$  concentration. Every 30 seconds an image of the HX surface was taken by a camera (Nikon D5600, F/4.5 aperture, 1/60 s exposure time, ISO-800, 50 mm focal length). The process was then monitored for 20 hours. Standard operating conditions were set to  $30^\circ\text{C}$  bulk temperature,  $70 \text{ kW/m}^2$ ,  $30 \text{ mmol L}^{-1}$  concentration of  $\text{CaSO}_4$  and a Reynolds number of  $\text{Re} = 2000$ . The complete set of process parameters used can be found in Table 2.3. Scanning electron microscope (SEM) images were taken of some deposits obtained from the experiments with a Philips REM XL 40. Figure 2.8 a shows a SEM picture taken of the obtained deposit of a PEEK surface at standard operating conditions. The needle like structure of the crystals is consistent with the formation found in gypsum [19].

**Table 2.3.:** Process parameters.

Re	Bulk temperature °C	Heat flux kW m <sup>-2</sup>	CaSO <sub>4</sub> concentration mmol L <sup>-1</sup>
2000; 8000	30	70; 90	25; 30

The fluid flow is characterized by the Reynolds number, which is given as

$$Re = \frac{vd_h}{\nu} = \frac{\dot{V}d_h}{A\nu} \quad (2.1)$$

Where

$$d_h = \frac{4A_s}{C} \quad (2.2)$$

The thermal performance of the heat exchanger is monitored by measuring the fouling resistance  $R_f$

$$R_f = \frac{1}{U_t} - \frac{1}{U_0} \quad (2.3)$$

Where  $U_0$  is the clean overall heat transfer coefficient at the beginning of the experiment

$$U_0 = \frac{1}{\frac{1}{\alpha_i} + \frac{d_p}{\lambda_p}} \quad (2.4)$$

And  $U_t$  is the overall heat transfer coefficient during the experiment ( $t > 0$ ), which is reduced by the additional thermal resistance from the fouling layer

$$U_t = \frac{1}{\frac{1}{\alpha_i} + \frac{d_p}{\lambda_p} + \frac{d_f}{\lambda_f}} \quad (2.5)$$

Since  $U$  is also

$$U = \frac{\dot{q}_{\text{const}}}{T_w(t) - T_{\text{bulk}}} \quad (2.6)$$

and  $T_{\text{bulk}}$  can be considered constant over time,  $R_f$  can be easily evaluated via

$$R_f = \frac{T_w(t) - T_w(t=0)}{\dot{q}_{\text{const}}} \quad (2.7)$$

$T_w(t=0)$  is determined at the start of the experiment and  $T_w(t)$  is constantly evaluated during the run. If fouling occurs then  $U_t < U_0$  and  $R_f > 0$ . The fouling resistance is linked to the fouling mass  $m_f$  [25]

$$m_f = R_f \rho_f \lambda_f \quad (2.8)$$

Where  $\rho_f$  is the density and  $\lambda_f$  is the heat conductivity of the deposit. According to the Kern and Seaton fouling model [26]  $m_f$  is a net deposition given by the formation of deposit  $\dot{m}_d$  and the removal of deposit  $\dot{m}_r$  from the surface

$$\frac{dm_f}{dt} = \dot{m}_d - \dot{m}_r \quad (2.9)$$

Theoretically,  $\dot{m}_d$  is considered to be dependent on the concentration of the foulant  $c_f$ , the stickability  $S$ , density of the fluid  $\rho$ , the cross-sectional area  $B$ , a proportional constant  $k_1$ , and the heat transfer surface area  $A_s$  [27]:

$$\dot{m}_d = \frac{k_1 c_f S \rho \nu B}{A_s (1 + k_1 (1 - S))} \quad (2.10)$$

$\dot{m}_r$  is considered to be dependent on  $u$  and the adhesion force  $\varphi$  [27]:

$$\dot{m}_r = K d_f \rho \rho_f \frac{\nu^2}{\varphi} \quad (2.11)$$

Where  $K$  is a proportional constant and  $d_f$  is the average fouling layer thickness.

## 2.4. Results

### 2.4.1. Standard Operating conditions

Impact of the three surface materials on the fouling resistance  $R_f$  for standard operating conditions are shown in Figure 2.5. For all three materials no induction phase was observed and fouling starts almost instantly. However, the extend of fouling varies greatly between the materials. For SS an asymptotic value of 0.3 m<sup>2</sup>K/kW is observed. Arbitrary scaling removal and growth after approximately 10 hours of run time are visible, which lead to a deviation from the asymptotic value. For PEEK the average  $R_f$  remains asymptomatic and constant at 0.15 m<sup>2</sup>K/kW, which is less than half of SS. The scaling behavior of TKT shows fast crystal growth in the early stages of the experiment, which is followed by a phase of scaling removal after 3 h of run time. This also causes the fouling resistance to be quasi-stationary at 0.5 m<sup>2</sup>K/kW for several hours. Contrary to SS, removal seems to decrease abruptly, leading to excessive scaling. This may be due to detached scaling particles reattaching to the deposit layer instead of being completely removed from the heat surface by the bulk fluid. After 18 h the experiment had to be terminated for safety reasons due to the heat buildup in the heating block.

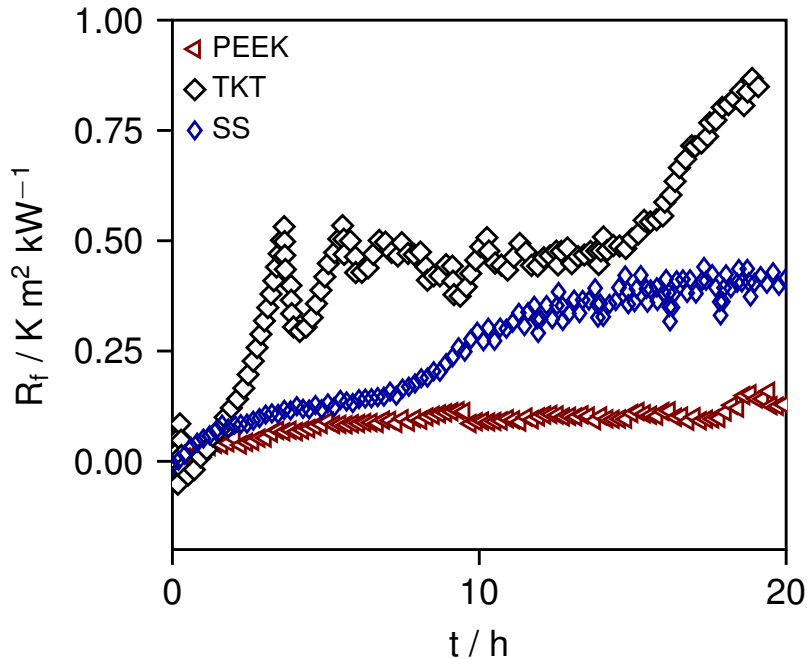


**Figure 2.5.:** Fouling resistance  $R_f$  as a function of time for SS, TKT and PEEK under standard operating conditions in the main channel.

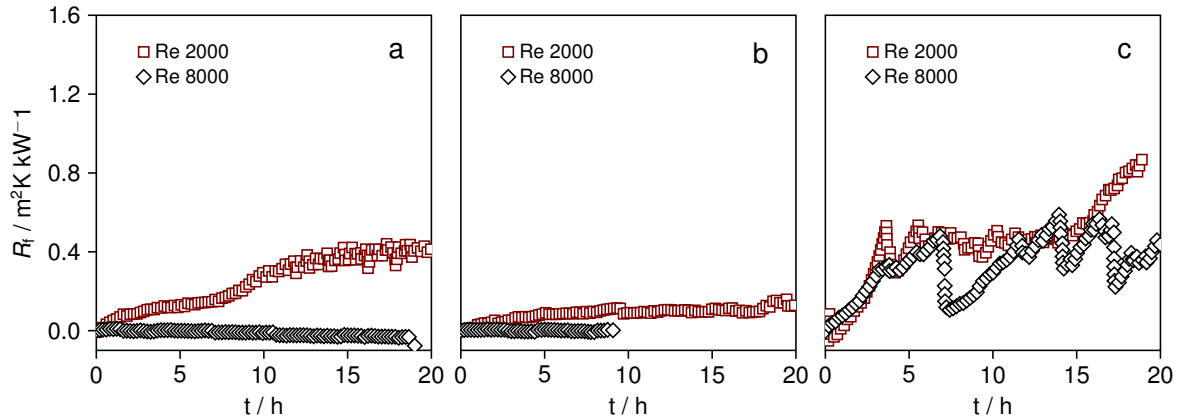
These experiments were repeated three times to validate the reproducibility. Table 2.4 shows the mean values and standard deviation of  $R_f$  at the end of the experiment for the three materials. For PEEK and SS small deviations of the mean value were found. However, for TKT higher deviations occurred, which can be attributed to a delay in the safety shutdown times. Table 2.2 shows surface free energy and roughness of the three materials. When considering these properties, there seems to be a trend between the roughness of the material and the amount of deposit forming on it. Material roughness can impact fouling behavior, when deposits are forming directly on the material surface. This is the case during the initial fouling stage and after detached deposits expose the surface material. In this study rougher surfaces lead to an increased fouling rate. A similar behavior was observed by several researchers [9, 28–30], however others found that fouling correlated better with other surface properties [15, 25]. In this study no direct influence of any other parameters such as surface free energy was found. Since low roughness correlates to low adhesion force [28], these results fit well with the theoretically predicted behavior of fouling removal formulated in Eq. 2.11, where  $m_r$  increases with low adhesion ( $\varphi$ ) between the surface and the fouling layer. Similarly, low stickability  $S$  leads to lower deposit mass according to Eq. 2.10, explaining why less fouling was observed for SS and PEEK.

**Table 2.4.:** Mean (M) and standard deviation (SD) of  $R_f$  at the end of the experiments for each material at standard operating conditions.

	SS		PEEK		TKT	
	M	SD	M	SD	M	SD
$R_f$ ( $\text{m}^2 \text{K kW}^{-1}$ )	0.34	0.06	0.18	0.07	1.03	0.22

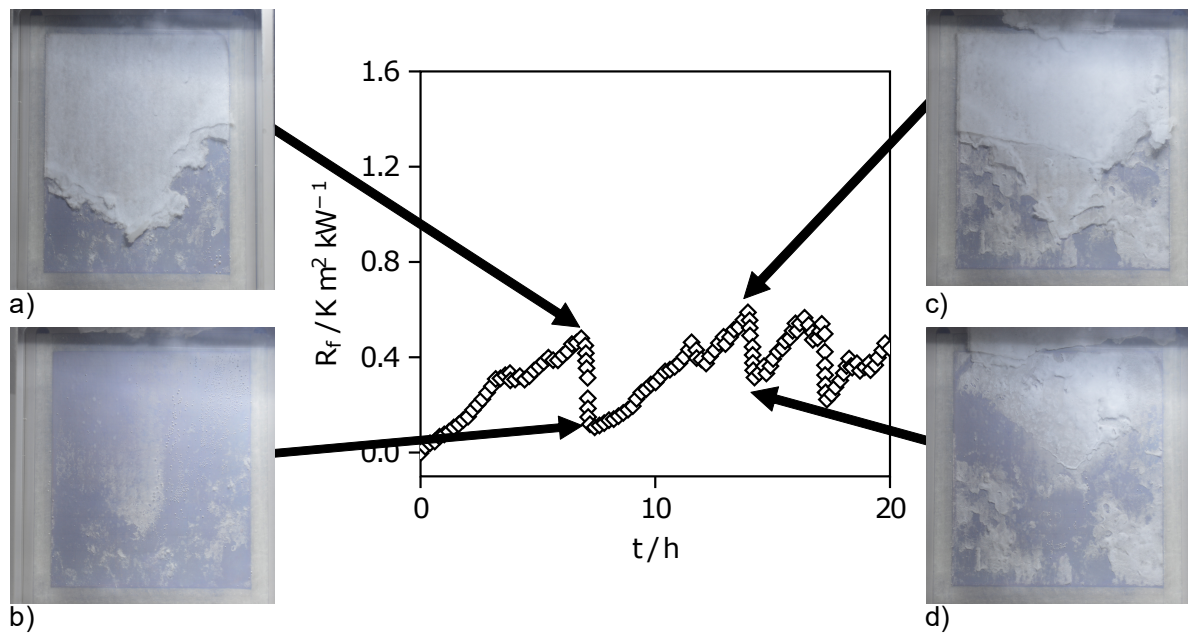
### 2.4.2. Variation of process parameters

Further experiments were conducted under variation of the process parameters. Figure 2.6 shows the effect of higher flow rates at  $Re = 8000$  on the fouling behavior of the three surfaces. Contrary to  $Re = 2000$  no fouling was detected at  $Re = 8000$  during the experiment. With little deviation of the  $R_f$  value it is also unlikely that any deposit formed at all on the surface. Similar results were obtained for the PEEK, where  $Re = 2000$  already showed very little fouling, therefore the experiment was terminated after 10h of run time. For the TKT run a saw-tooth fouling behavior was observed for  $Re = 8000$ . In the beginning of the experiment an almost identical fouling rate was observed compared to  $Re = 2000$ . However, the  $R_f$  drops multiple times sharply after reaching approximately  $0.5 \text{ m}^2\text{K}/\text{kW}$ , which indicates that significant amounts of deposit detach from the surface. Each drop in  $R_f$  is then followed by renewed fouling growth. For the duration of the experiment this was a quasi-stationary process. These results fit well with the theoretically predicted behavior of fouling removal formulated in Eq. 2.11, where  $\dot{m}_r$  increases with higher velocities ( $v$ ).



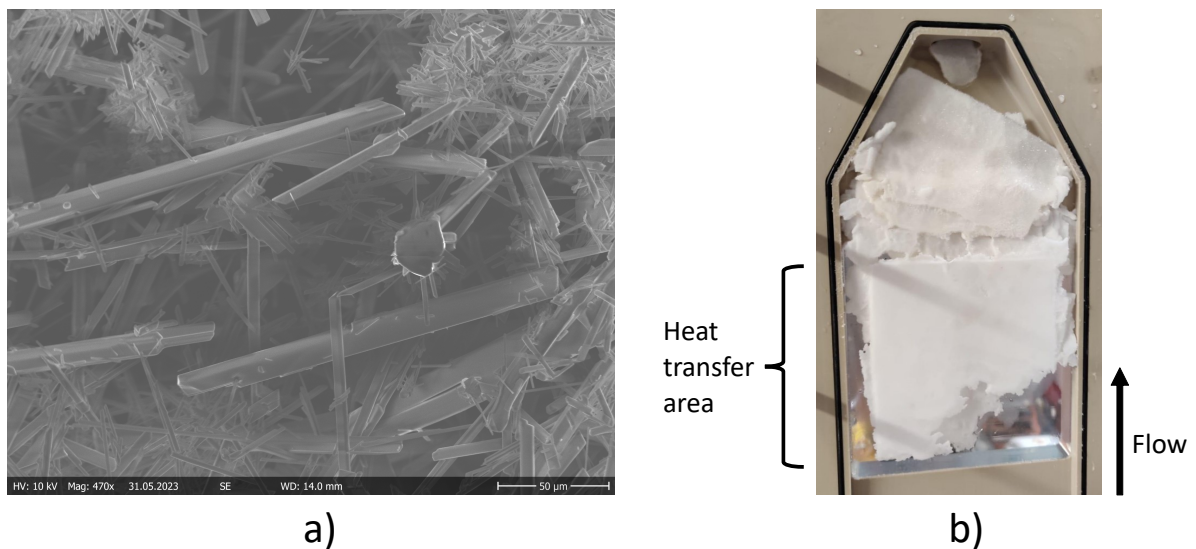
**Figure 2.6.:** Fouling resistance  $R_f$  as a function of time for SS, TKT and PEEK under standard operating conditions conditions and increased flow rate in the main channel.

Figure 2.7 shows images of the surface during the experimental run of TKT. The images confirm that large parts of the fouling layer do detach from the surface, explaining the sudden drop of the fouling resistance. In image a), right before the first drop in  $R_f$ , about two thirds of the heat exchanger surface are already covered with deposit. After the drop the surface shown in image b) is almost completely clean, which correlates with a  $R_f$  of  $0.1 \text{ m}^2\text{K}/\text{kW}$ . After 14 hours of run time another drop occurs. Here, image c) shows that the surface shortly before the removal has slightly more fouling than in a), corresponding to a higher measured  $R_f$ . After the removal in d) more deposit remains compared to b), which can also be seen in the corresponding  $R_f$  value. Besides showing that the measured fouling resistance correctly represents the amount of fouling on the surface, this indicates that the experimental run times should be kept short, to avoid blocking the channel outlet with fouling deposit.



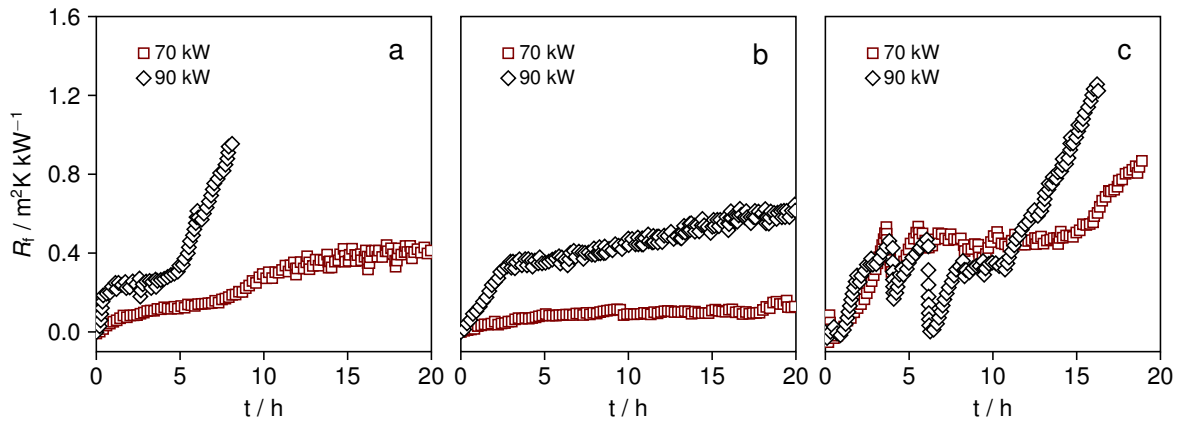
**Figure 2.7.:** Fouling resistance  $R_f$  as a function of time for SS, TKT and PEEK under standard operating conditions and increased flow rate in the main channel.

Figure 2.8 shows the deposit that has accumulated in the channel after a TKT run of 60 hours. Multiple deposit layers that have detached from the HX surface have accumulated downstream in the channel. The blockage prevents further deposition removal, resulting in excessive fouling on the heat exchanger surface that completely covers the height of the channel. This phenomenon drastically increases the heat transfer resistance, although it is not directly caused by the fouling, but rather a combination of the fouling and the channel design. These results confirm that experimental run times for these process conditions should be kept short to avoid secondary effects. Similar behavior can be expected in an industrial-sized heat exchanger, where the flow volume is often smaller and the geometry more confined than in the present setup.



**Figure 2.8.:** SEM image of calcium sulfate deposit (a) and deposit agglomeration after 60 hours with  $\text{Re} = 8000$  and TKT (b).

Besides the Reynolds number the heat flux was varied to study the influence of surface temperature on the fouling behavior. Figure 2.9 shows the result for an increased heat flux of 90 kW/m<sup>2</sup> compared to the standard operating conditions. For SS the fouling behavior changes significantly. Instead of asymptotic behavior, now a linear increase is observed. After the faster initial increase in  $R_f$ , compared to 70kW, a short period of removal keeps the  $R_f$  almost constant, as was observed with TKT for 70 kW/m<sup>2</sup>. This is followed by another phase of linear increase in  $R_f$ , also similar to TKT at 70 kW/m<sup>2</sup>, until the safety switch is triggered. Increased fouling was also observed for PEEK, where now substantial fouling was observed. The initial linear increase in fouling is reduced to a lower incline by the onset of removal. For TKT the fouling behavior is similar to 70 kW/m<sup>2</sup>, except for slightly increased inclines and harsher drops in  $R_f$ , suggesting that deposits are removed in larger flakes.



**Figure 2.9.:** Fouling resistance  $R_f$  as a function of time for SS (a), PEEK (b) and TKT (c) under standard operating conditions and increased heat flux in the main channel.

The last process parameter that was varied is the calcium sulfate concentration. A concentration of calcium sulfate of 25 mmol L<sup>-1</sup> was used to investigate the effect on the fouling behavior. At this concentration the solution is still supersaturated and should therefore deposit under heating. Results are shown in Figure 2.10. For SS a slightly lower fouling resistance was measured, with smaller deviations in  $R_f$  compared to a calcium sulfate solution of 30 mmol L<sup>-1</sup>, indicating the removal of smaller deposit flakes from the heat transfer surface. Surprisingly, for PEEK a slightly higher fouling resistance was measured throughout the experiment, which drops back to the  $R_f$  of 30 mmol L<sup>-1</sup> at the end of the experiment. TKT is the only material where significant changes in the fouling behavior occur. The fouling resistance remains much lower than for a CaSO<sub>4</sub> concentration of 30 mmol L<sup>-1</sup> and is in fact very similar to that of PEEK and SS. The results indicate that indifferently of the surface material, very little fouling will form, which highlights the impact of salt concentration on the fouling behavior. Similar results were found elsewhere [21, 31].

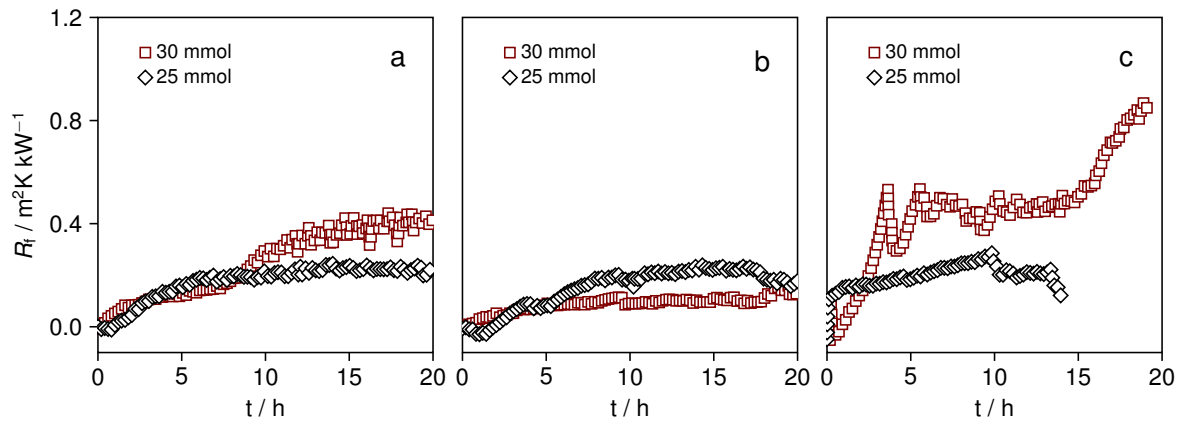


**Figure 2.10.:** Fouling resistance  $R_f$  as a function of time for SS (a), PEEK (b) and TKT (c) under standard operating conditions and decreased  $\text{CaSO}_4$  concentration in the main channel.

### 2.4.3. Apparatus comparison and cleanability

The two setups were used to check if similar results could be obtained from the smaller setup that can hold multiple samples simultaneously. The results are shown in Figure 2.11. For SS the fouling curve shows a much more pronounced S-shape. Therefore, smaller  $R_f$  values were observed in the beginning of the experiment and slightly larger values were measured at the end of the run. For both setups an asymptotic behavior was found. For PEEK differences were seemingly much smaller, but this might be due to small amount of deposit forming in both setups. For TKT the fouling behavior of the screening apparatus shows a large induction phase of approximately 11h, where  $R_f$  remains almost constant. Only in the second half of the experiment fouling seems to occur. Then a similar fouling rate is achieved. In the latter stages of the experiment deposit removal seems to start, as was observed with the standard setup. The variation in induction times between the setups indicates that the nucleation rates may be dependent on the testing rig. A possible reason for this is sealing tape in the screening apparatus, which forms a 0.8 mm barrier for the fluid right before the heat transfer surface begins. This may affect the flow locally and limit nucleation. However, both setups deliver the same qualitative fouling behaviors depending on the used material and a similar qualitative behavior.

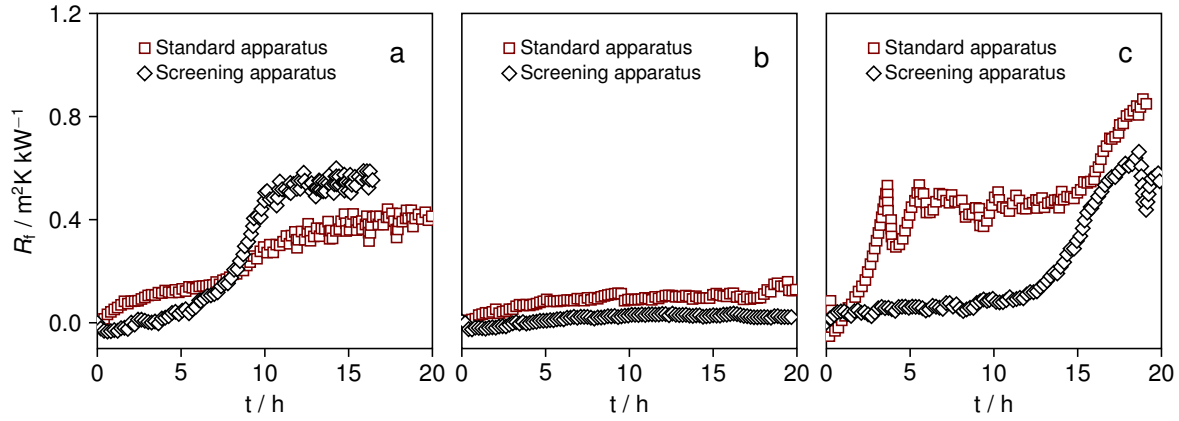


**Figure 2.11.:** Fouling resistance  $R_f$  as a function of time for SS (a), PEEK (b) and TKT (c) under standard operating conditions in the main and screening channel.

The screening apparatus can also be used to investigate the cleanability of the surfaces. Ideally, the heat transfer surface is cleaned without the use of detergents such as sodium hydroxide or by manually scraping deposits from the surface. An alternative is the usage of the process solution or pure water (cleaning in process, CIP) at high volumetric flow rates to induce a higher shear stress and thus foster detachment. In this study no cleaning effect could be observed by simply increasing the volumetric flow of the solution. Instead an approach with deionized (DI) water was applied to clean the surfaces. At first a fouling run under standard operating conditions is performed, until all materials have a similar fouling layer. Then the solution is drained and exchanges for DI water, which flows with a tenfold increase in volumetric flow through the channel. Figure 2.12 (a) shows the fouled surfaces at the beginning of the cleaning process, and (b) shows the surfaces after 10 minutes of cleaning. The water has by then slowly dissolved parts of the deposit, which is visible on SS and TKT. For PEEK no fouling remains, as the adhesion force between surface and deposit was not strong enough. A similar process was observed for TKT and SS, however only after 40 minutes, respectively 30 minutes of cleaning. This results shows the impact of the different roughness values of these materials, which in turn affects the adhesion force of the crystals.

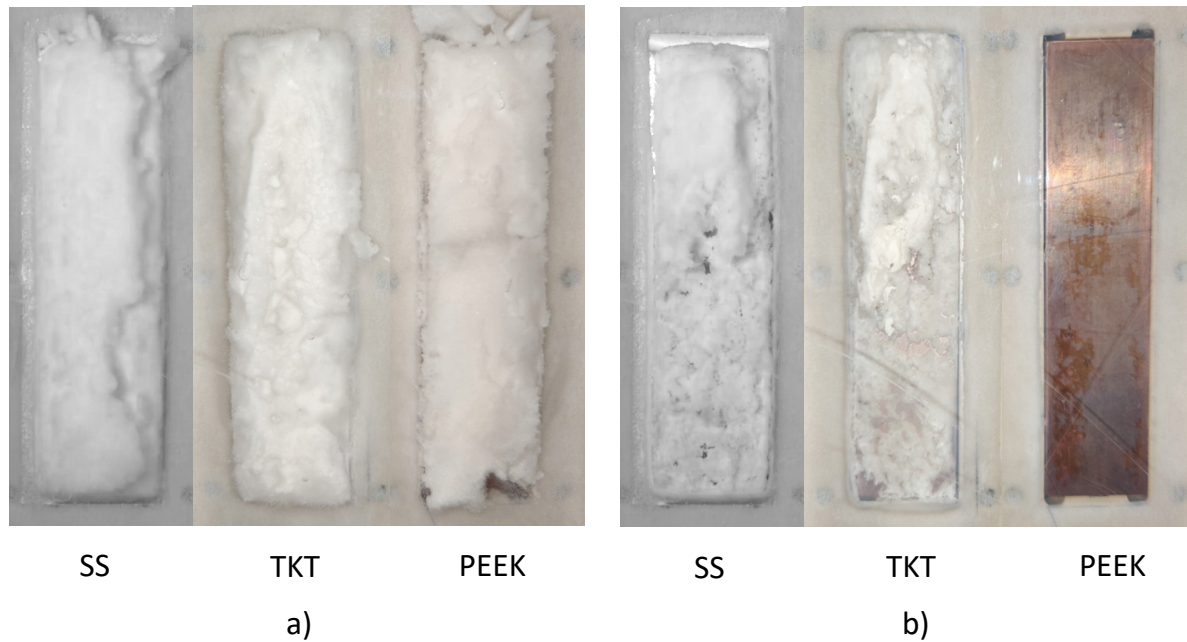


**Figure 2.12.:** Deposits after experimental run with  $Re = 2000$ ,  $70 \text{ kW/m}^2$ ,  $30 \text{ mmol L}^{-1}$ ,  $30^\circ\text{C}$  bulk temperature at the beginning (a) and after 10 minutes (b) of cleaning with DI water.

## 2.5. Conclusion

The aim of this study was to assess the ability of two novel heat exchanger materials (PEEK, TKT) to mitigate calcium sulfate fouling and compare results to benchmark steel (SS). The thermal resistance  $R_f$  was used to quantify this susceptibility under variation of process parameters. These parameters were chosen so that fouling would develop quickly and that the runtime could be minimized. Results were compared to a second, smaller apparatus which allows the simultaneous testing of up to three materials to reduce the amount of experiments needed. Finally, the cleanability of the materials was investigated. The results clearly showed differences in fouling susceptibility, with PEEK showing the highest fouling mitigation, followed by SS and TKT. Reproducibility tests conducted for the standard operating conditions showed low deviations between the runs and therefore confirmed this ranking of materials. While different process conditions increased or decreased the deposits overall, the ranking of the materials based on the fouling resistance remained the same. Moreover, the same results were qualitatively obtained from the second testing rig, however different quantitative values were observed. Similar results were also observed for the cleaning procedure with deionized water, where PEEK surfaces were cleaned the fastest, followed by SS and finally TKT. These differences were attributed to the roughness of each material, which affects the adhesion force between the deposit layer and the surface material.



# 3. Whey protein fouling on polymeric heat exchangers

## *Contributor Roles Taxonomy*

Philipp Pelz: conceptualization; data curation; investigation; methodology; visualization; writing – original draft; writing – review & editing

*Chapter redrafted after the following main publication:*

P. Pelz, J. Noß, E. von Harbou, and H.-J. Bart "Whey protein fouling on polymeric heat exchangers," *Heat Transfer*, 2024. DOI: <https://doi.org/10.1002/htj.23070>.

## **Abstract**

The fouling behavior of whey protein concentrate (WPC) in food-grade polyether ether ketone (PEEK) heat exchangers was compared to benchmark stainless steel (SS) to evaluate if fouling can be better mitigated by using PEEK. No research has been conducted on WPC fouling behavior of PEEK at WPC concentrations of 2 to 6 g/L and heat flux densities of 45 to 55 kW/m<sup>2</sup>. It was found that PEEK materials led to a reduction in heat resistance of up to 40%. At WPC concentrations of 6 g/L a fouling resistance of 0.9 m<sup>2</sup>K/kW was measured for PEEK compared to 1.6 m<sup>2</sup>K/kW for SS. Despite a constant heat flux, fouling curves for PEEK showed an asymptotic behavior, whereas linear fouling was observed for SS. In order to achieve a comparable heat resistance between PEEK and SS heat exchangers, the operating time could be extended by 9 hours when using PEEK materials. Investigations of the deposit mass showed that even though the heat transfer resistance is limited on PEEK, fouling continued to grow at a decreased rate. It was found that the fluid started to evaporate underneath the fouling layer, which led to a partial detachment of the fouling layer and therefore mitigated the heat resistance effects of fouling. To test whether these results are transferable to larger setups, experiments on a scale-up apparatus were conducted. A very similar behavior was qualitatively observed, however measured deposition deviated on average by 18%. PEEK surfaces also showed great promise regarding cleanability, with fouling layers detaching completely after drying for 10 minutes and restarting the process. This restored the heat transfer coefficient to its clean state. A cleaning in place therefore seems feasible. In contrast fouling layers on SS did not detach through drying and had to be chemically cleaned to restore its heat transfer capacity.

### 3.1. Introduction

Fouling has a major impact in the dairy industry, which needs to heat its products to meet stringent quality and hygiene requirements. The constantly increasing raw milk production grew by 1.8-2.3 % p.a. over the last decade, which amounts to 897 million tons for 2022 [32]. During dairy processing severe fouling occurs in heat exchangers, which leads to frequent downtime and cleaning cycles of 24 hours or less [33]. Since these production interruptions are a dominant cost factor [34, 35], reducing in-situ or cleaning in place procedure times are of great interest to minimize plant downtime and costs [36].

Milk is subject to composition change depending on source origin and season [37–39]. To achieve more consistent fouling results model fluids such as whey protein concentrate (WPC), whey protein isolate or simulated milk ultrafiltrate are used to ensure constant substance properties [40, 41]. Furthermore, whey proteins are heat sensitive and are a major contributor to fouling in milk [42]. Fouling can be classified in two categories known as type A and type B [43, 44]. Type A deposits are formed at temperatures up to 110°C have a white, soft, spongy appearance and consist mostly of proteins [45]. Type B deposits are formed at temperatures over 110°C, have a hard, compact, grey appearance and consist mostly of minerals [1].

Measures taken to compensate economic and environmental losses are often limited to equipment oversizing and increased energy input, which drives capital or operational costs. Instead, losses can also be reduced by utilizing less fouling susceptible heat exchanger materials such as polymers [11, 29]. Polyether ether ketone (PEEK) is a high-performance polymer that has good tensile strength, a low susceptibility to crystallization and biological fouling [9, 15, 24, 46] and is FDA (US Food and Drug Administration) approved for food grade applications [47, 48]. However very little data has been published on the effectiveness of PEEK on dairy product fouling [48] and no work was found on continuous heat exchanger operation.

This study therefore explores the behavior of WPC fouling on two PEEK surfaces in a screening apparatus and compares results to benchmark stainless steel 1.4301 (SS). To check whether the fouling behavior is applicable to larger heat exchangers, the results are tested against a scale-up apparatus. Finally, in-situ cleaning was investigated for all tested materials.

### 3.2. Experimental setup

The experimental setup described in Section 2.3.1 which consists of a screening channel and a scale-up channel is used to perform the experiments. Here too, a Nikon D5600 camera (F/4.5 aperture, 1/60 s exposure time, ISO-800, 50 mm focal length) is used to visually monitor the fouling process. The camera is placed in front of the PMMA lid and takes a picture every 30 seconds during each run.

### 3.3. Data Reduction

The following equations, which are explained in detail by Verein Deutscher Ingenieure [13], are used to calculate fouling. The Reynolds number inside the channel is calculated using Eq. 2.1. Accordingly, the hydraulic diameter  $d_h$  can be calculated via Eq. 2.2. The heat flow  $\dot{Q}$  can be calculated with

$$\dot{Q} = AU\Delta T \quad (3.1)$$

Here,  $A$  is the heat transferring surface and  $\Delta T$  is the temperature difference between the hot and cold interface where the heat transfer occurs. The heat flow is supplied electrically via heating cartridges to keep it constant and can be calculated by monitoring the voltage  $V$  and current  $I$

$$\dot{Q}_{\text{const}} = IV \quad (3.2)$$

The thermal performance of the heat exchanger is monitored by measuring changes in the  $R_f$  value (s. Eq. 2.3, where the clean overall heat transfer coefficient  $U_0$  is calculated using Eq. 2.4 and  $U_t$  is calculated using Eq. 2.5 at different times of the experiment. When fouling occurs then  $U_t < U_0$  and  $R_f > 0$ .

### 3.4. Materials

The investigated heat transfer materials were SS, PEEK and TKT, which were obtained as described in Section 2.3.2. High grade whey protein with a whey protein content of over 77 mass-% was used to carry out experiments. Table 3.2 shows the components of the purchased whey protein concentrate Bayolan P80 from Bayerische Milchindustrie eG, Landshut, Germany.

**Table 3.1.:** Material properties [9].

Property	PEEK	TKT	SS	Unit
Thickness	25	35	25	$\mu\text{m}$
Thermal conductivity	0.25	0.43	15	W/mK
Surface roughness $S_a$	0.06	0.59	0.13	$\mu\text{m}$
Surface free energy	40.57	43.55	32.38	mN/m
Polarity	10.40	10.47	12.29	%

**Table 3.2.:** Properties of the used Bayolan P 80 WPC as provided by Bayerische Milchindustrie eG [49].

Ingredient	mass-%	Method
Whey protein in dry mass	>80	calculated
Whey protein	77.7	DIN EN ISO 8968
Lactose	2-5	calculated
Ash	2.7	DIN 10477
Fat	5.5	Weibull-Stoldt

### 3.5. Experimental procedure

The heat transferring materials are cleaned with isopropanol and deionized water before being placed on the copper blocks and fixated by the sealing tape (screening channel) or O-ring seals (scale-up channel). 80 liters of deionized water are filled into the system and are heated to 40 °C. Then the desired heat flux is fed through the copper blocks into the water.  $U_0$  is determined after a constant temperature profile is observed via the thermocouples. Then 2 liters of water are taken out of the plant to dissolve the WPC powder. The mixture is then fed back into the system and the fouling process starts. Temperatures in the copper blocks are constantly monitored during the run. The system is cleaned multiple times with deionized water and visually inspected after each run to ensure that no WPC traces are left in the experimental setup. The deposits and heat transferring surfaces are then extracted from the channel. The fouling layers were removed from the surface by scraping the deposits off or by dissolving the layer in sodium hydroxide. The heat transfer materials were disposed after use and the deposits were weighted using a Sartorius 1712 fine scale. A comprehensive list of process parameters can be found in Table 3.3.

**Table 3.3.:** Process parameters.

Re	Bulk temperature	Heat flux	WPC concentration
-	°C	kW/m <sup>2</sup>	g/L
2000	40	45; 55	2; 4; 6

### 3.6. Results

Results for the fouling resistance  $R_f$  at Re 2000, 2 g/L, 45 kW/m<sup>2</sup> and 40 °C bulk temperature are shown in Figure 3.1. Similar values for all three materials were measured throughout the experiment. However, PEEK materials show asymptotic curves whereas the steel has two distinct linear curves. At the end of the experiment both PEEK materials have slightly higher  $R_f$  -values than steel (TKT:  $R_f = 0.91$  K m<sup>2</sup>/ kW, PEEK:  $R_f = 0.9$  K m<sup>2</sup>/ kW, SS:  $R_f = 0.86$  K m<sup>2</sup>/ kW). This experiment was repeated 3 times to check the reproducibility. Only small deviations were found. Results can be found in Table 3.4.

**Table 3.4.:** Reproducibility of experiment at Re 2000, 2 g/L, 45 kW/m<sup>2</sup>, and 40 °C bulk temperature.

Material	Mean $R_f$	Standard deviation $\sigma$
-	m <sup>2</sup> K/kW	m <sup>2</sup> K/kW
PEEK	1.04	$\pm 0.066$
TKT	0.96	$\pm 0.084$
SS	0.84	$\pm 0.040$

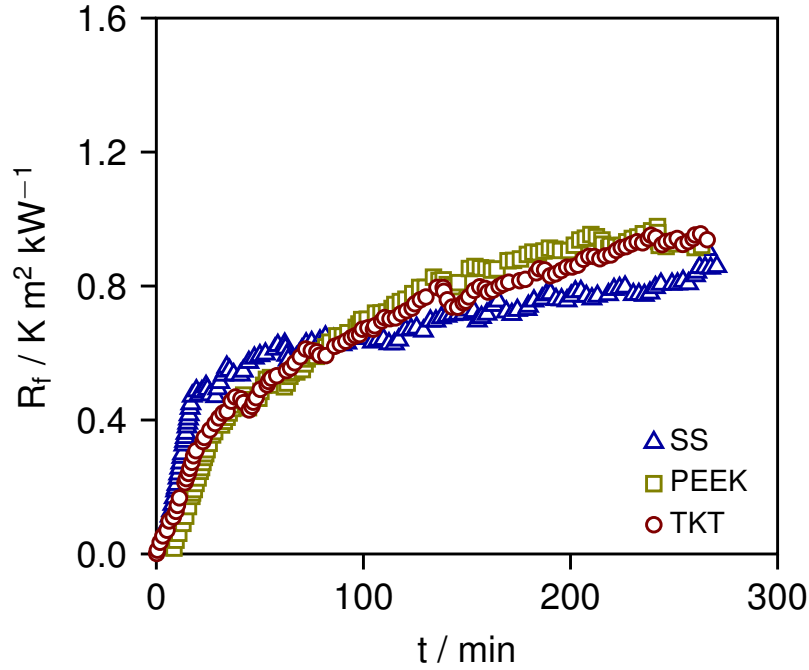


**Figure 3.1.:**  $R_f$  values for PEEK, TKT and SS at Re 2000, 2 g/L, 45 kW/m<sup>2</sup> and 40 °C bulk temperature.

In Figure 3.2a higher WPC concentrations were tested on SS. Increasing the concentration should also increase fouling as the reaction kinetics can be described by a first order Arrhenius reaction, which is concentration dependent [1, 40].  $R_f$  increases sharply, with a longer initial growth phase and a steeper incline during these fouling runs. Especially the increase from 2 g/L to 4 g/L seems to effect fouling with the  $R_f$ -value more than doubling at the end of the experiment. Increasing the concentration from 4 g/L to 6 g/L leads to even faster fouling, with a 25% increase in the fouling resistance. Increasing the heat flux increases the interfacial temperature at the liquid solid interface, which should promote fouling as the reaction kinetics are temperature dependent [1, 40]. The figure indeed shows that for a heat flux of 55 kW/m<sup>2</sup> the fouling rate increases compared to 45 kW/m<sup>2</sup>. The measured heat resistance remains lower than at a WPC concentration of 4 g/L. The high fouling rates measured for 4 and 6 g/L led to experiments being prematurely terminated for safety reasons due to high temperature built up in the copper blocks.

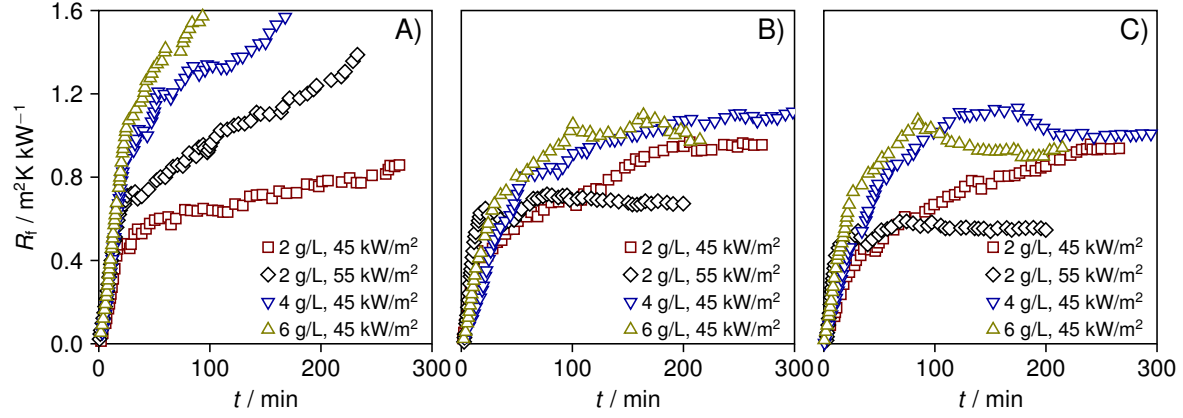


**Figure 3.2.:**  $R_f$  values for SS (a), PEEK (b) and TKT (c) at Re 2000, 40°C bulk temperature.

In comparison Figure 3.2b also shows the  $R_f$  values for the same operating conditions on PEEK. All runs have a falling curve and lower  $R_f$ -values were measured compared to SS. At a concentration of 4 g/L the  $R_f$  increases only slightly from 0.9 to 1.1 m<sup>2</sup>K/kW. Similar results were observed for 6 g/L with the  $R_f$  falling slightly at the end of the run. Remarkably, at a higher heat flux the  $R_f$  values are lower than for 45 kW/m<sup>2</sup>, indicating that at higher heat flux values the heat transfer is less compromised by fouling than at 45 kW/m<sup>2</sup>.

Similar results were obtained for TKT (s. Figure 3.2c). Again, no significant effect of WPC concentration on the fouling resistance was observed. At 55 kW/m<sup>2</sup> lower  $R_f$  values were measured than at 45 kW/m<sup>2</sup>. The data shows that SS, PEEK and TKT have an almost identical fouling behavior for low WPC concentrations.

However, SS has a linear increase in  $R_f$  throughout the experiment, whereas PEEK and TKT have a falling curve, indicating that for longer runs the heat transfer on PEEK and TKT will be less compromised by fouling than on steel. At higher WPC concentrations this becomes significant, as the fouling rate increases substantially on SS, whereas no additional effect on  $R_f$  was measured for PEEK and TKT. At higher heat flux densities, the heat transfer was also less obstructed on PEEK and TKT compared to SS, showing that longer operating times are possible with PEEK and TKT materials.

This behavior can be explained when the temperature profiles  $T_w(t)$  are considered. Figure 3.3a shows that for SS  $T_w(t)$  is increasing over time as expected, whereas temperatures are limited to 120°C ± 4°C for PEEK and TKT in all experiments, including the runs at an increased heat flux. Since  $T_w(t = 0)$  is higher at 55 kW/m<sup>2</sup> than at 45 kW/m<sup>2</sup>, the  $R_f$  values must be lower according to equation 2.7. Images taken during the fouling runs (s. Figure 3.4) explain why the temperature is limited. The fouling layer partly detaches from the polymer surfaces as the fluid starts to boil underneath the layer. Evaporation bubbles are moving upwards further detaching the fouling layer. The fouling layer may be detaching due to lower adhesion forces between the layer and polymer surfaces compared to SS. Common parameters that influence adhesion are surface roughness, surface free energy and surface polarity. However, measurements (s. Tab.3.1) are inconclusive, as roughness and surface free energy values show no clear dependency on adhesion behavior. Even though a slight decrease in surface polarity

was measured for the polymers, it is unlikely to cause the significant adhesion change that was experimentally observed.

The low  $R_f$  values of TKT and PEEK indicate that heat can be transferred efficiently at lower temperatures, which means the utilities required to facilitate the heat transfer in an industrial process, such as hot water or steam can be of lower temperature as well. Therefore, they can be produced more cost effectively than the high temperature utilities needed for SS. The asymptotic fouling behavior of TKT and PEEK also suggests that there is a heat resistance will not increase over time, potentially extending operating times of the heat exchanger, which also decreases cost.

While heat transfer can be maintained throughout the runs,  $R_f$  values might not accurately describe the amount of fouling accumulating on the surfaces.

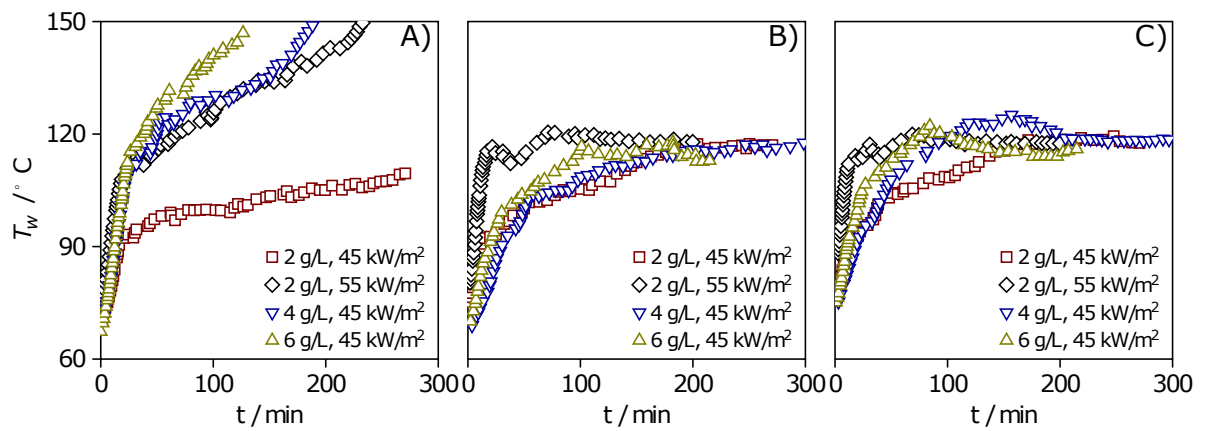


**Figure 3.3.:** Block temperatures for SS (a), PEEK (b) and TKT (c) at Re 2000, 40 °C bulk temperature.

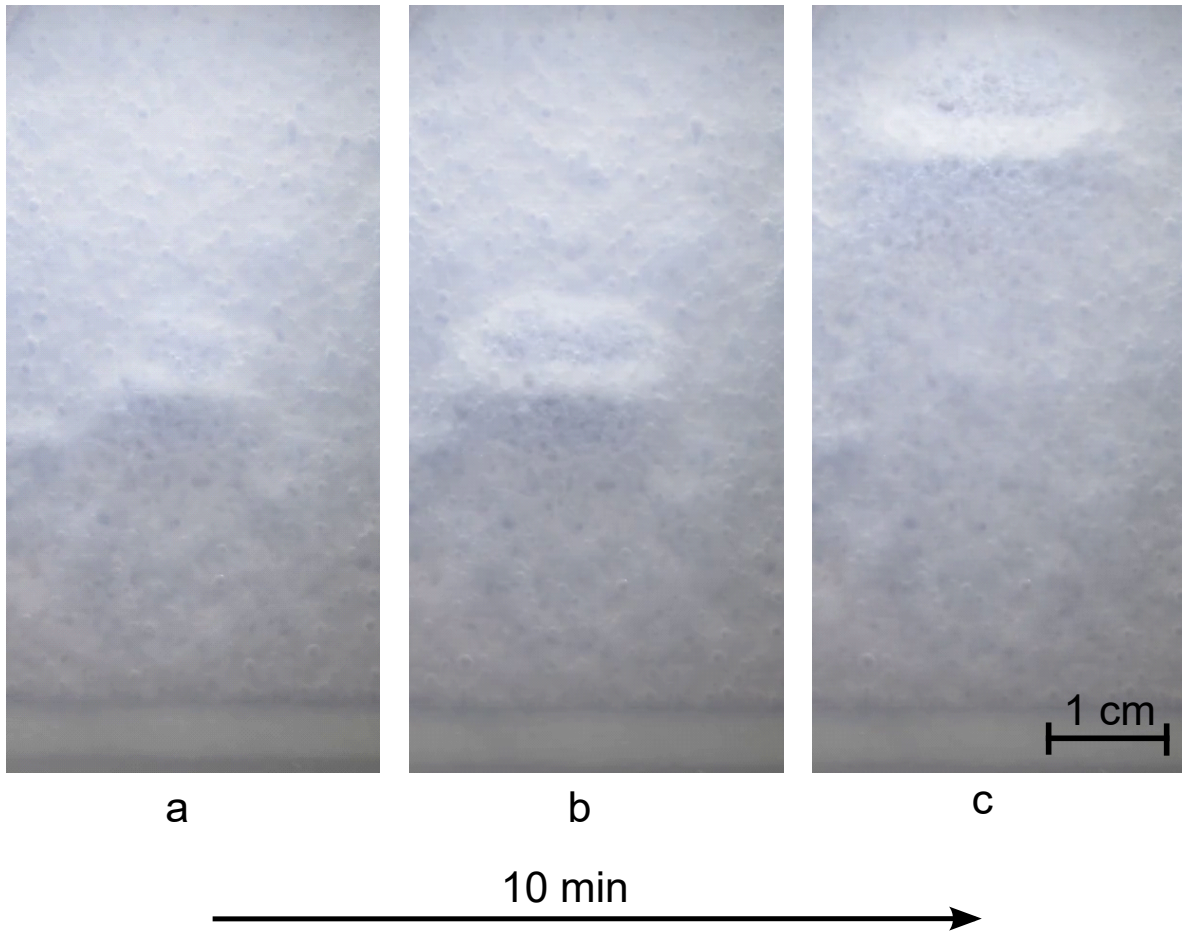


**Figure 3.4.:** Evaporation bubbles forming underneath fouling layer (a, b) and bubbles partly detaching deposit layer as they move upwards (c) in the scale-up apparatus at operating conditions of  $Re$  2000,  $55 \text{ kW/m}^2$ ,  $40^\circ\text{C}$  bulk temperature,  $c_{\text{wpc}}$  of  $2 \text{ g/L}$ .

To validate the  $R_f$  results, deposit mass on PEEK and TKT were measured after each experiment. Figure 3.5 shows the results, where error bars indicate the standard deviation. Each experiment was performed at least 2 times. Figure 3.5a shows that the deposition increases from  $2$  to  $4 \text{ g/L}$  at  $45 \text{ kW/m}^2$  by  $75\%$  (s. Tab. 6). The high deviation in the measured data for  $6 \text{ g/L}$ ,  $45 \text{ kW/m}^2$  does not allow an analysis for the increase from  $4$  to  $6 \text{ g/L}$ . Increasing the concentration from  $2$  to  $4 \text{ g/L}$  at a heat flux of  $55 \text{ kW/m}^2$  increases  $m_f$  by  $60\%$  and the increase from  $4$  to  $6 \text{ g/L}$  showed an increase of  $103\%$ . Lower deviations were measured for all  $55 \text{ kW/m}^2$  experiments compared to  $45 \text{ kW/m}^2$ . The higher deviations at  $45 \text{ kW/m}^2$  may be caused by the low interfacial temperature of  $70\text{-}80^\circ\text{C}$ , which is right at the temperature limit of whey protein denaturation at  $70\text{-}74^\circ\text{C}$  [1]. Therefore, no aggregation or delays in the formation of deposits may occur.

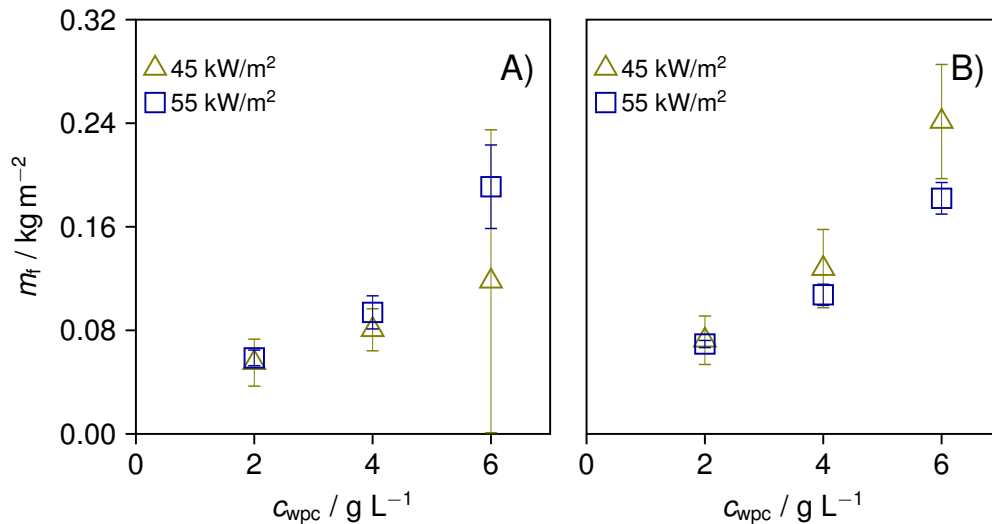


**Figure 3.5.:** Deposit mass for PEEK (a) and TKT (b) at Re 2000, 40°C bulk temperature.

Similar results were observed for the deposition on TKT. The data shows that the mass increases with higher WPC concentrations for both heat flux densities. For 45 kW/m<sup>2</sup> deposition increased by 77% when the concentration was increased from 2 to 4 g/L. At 6 g/L an increase of 89% in deposition mass was measured compared to 4 g/L (s. Tab. 3.5). Similar results were obtained for 55 kW/m<sup>2</sup> with a 55% and 69% increase when increasing the concentration to 4 g/L, respectively 6 g/L. On average lower depositions of 18% were measured on PEEK compared to TKT for all experiments.

The results are in good agreement with measured depositions found in literature. For example, Khaldi, Blanpain-Avet, Guérin, Ronse, Bouvier, André, Bornaz, Croguennec, Jeantet, and Delaplace [50] and Liu, Chen, Jeantet, André, Bellayer, and Delaplace [51] reported 0.26-0.62 kg/m<sup>2</sup> on a plate heat exchanger. Since operating conditions, materials and working principle differ from the setup in this work, detailed comparisons are not applicable.

**Table 3.5.:** Experimental data of  $m_f$  for screening apparatus.

Material	Heat flux kW m <sup>-2</sup>	WPC concentration g L <sup>-1</sup>	Deposition kg m <sup>-2</sup>	Standard deviation kg m <sup>-2</sup>
PEEK	45	2	0.05505	0.01814
PEEK	45	4	0.09669	0.01624
PEEK	45	6	0.11729	0.11699
PEEK	55	2	0.05873	0.00601
PEEK	55	4	0.09388	0.01279
PEEK	55	6	0.19094	0.03226
TKT	45	2	0.07235	0.01871
TKT	45	4	0.12771	0.03022
TKT	45	6	0.24131	0.04409
TKT	55	2	0.06945	0.00276
TKT	55	4	0.10747	0.00816
TKT	55	6	0.18200	0.01220

Different conclusions have to be drawn from the results of  $R_f$  and  $m_f$ . The latter has a clear dependency of concentration on fouling, whereas  $R_f$  shows none.  $m_f$  indicates no dependency of heat flux on fouling, whereas  $R_f$  is much lower for the higher heat flux. This means that the detaching fouling layer allows the heat transfer to continue on polymer surfaces even though fouling still continues to grow. To validate that fouling continues to grow on polymer surfaces and to examine whether the heat transfer continues to be possible over longer periods of time an experimental run of 15 hours was performed. Figure 3.6 shows the fouling resistance for PEEK compared to SS. After 3 hours of run time a  $R_f$  of  $0.77 \text{ m}^2\text{K/kW}$  is reached, which increased only slightly by  $0.1 \text{ m}^2 \text{ K/kW}$  until the end of the run. This shows that polymer surfaces allow a continued heat transfer even for long fouling runs. The measured deposit mass was  $0.1222 \text{ kg/m}^2$ , which is much higher than the  $0.055 \text{ kg/m}^2$  measured for the regular 5 hours run, confirming that fouling is still growing after boiling occurs on the polymer. It also shows that the fouling rate is reduced, with  $0.011 \text{ kg}/(\text{m}^2 \text{ h})$  depositing on a regular run compared to  $0.0081 \text{ kg}/(\text{m}^2 \text{ h})$  for the long run, a 26% reduction.

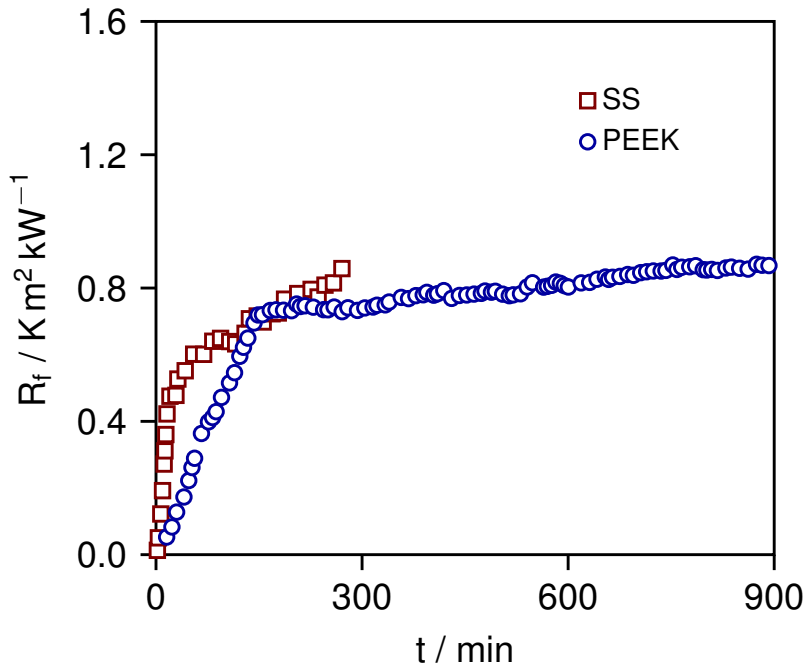


**Figure 3.6.:**  $R_f$  of PEEK long term experiment and SS for comparison at  $\text{Re } 2000$ ,  $40^\circ\text{C}$  bulk temperature.

To investigate whether the results are scale able, experiments were performed on a larger heat transfer surface. Figure 3.7 shows experimental data for  $R_f$  and  $m_f$  of the scale-up. Error bars for the  $m_f$  indicate the standard deviation. Each experiment was performed at least 2 times. Results show a similar curve for the fouling resistance  $R_f$ , with almost identical values at the end of the run. The deposition (s. Tab. 3.6) for  $45 \text{ kW/m}^2$ ,  $2 \text{ g/L}$  is 27% higher than that of the screening apparatus. For a concentration of  $4 \text{ g/L}$  and  $6 \text{ g/L}$  a 51%, respectively 21% reduction in deposit mass was measured. For the  $55 \text{ kW/m}^2$  the increase in deposit mass was 11% for  $2 \text{ g/L}$  and 4% for  $4 \text{ g/L}$ . For  $6 \text{ g/L}$  a decrease of -5% was measured.

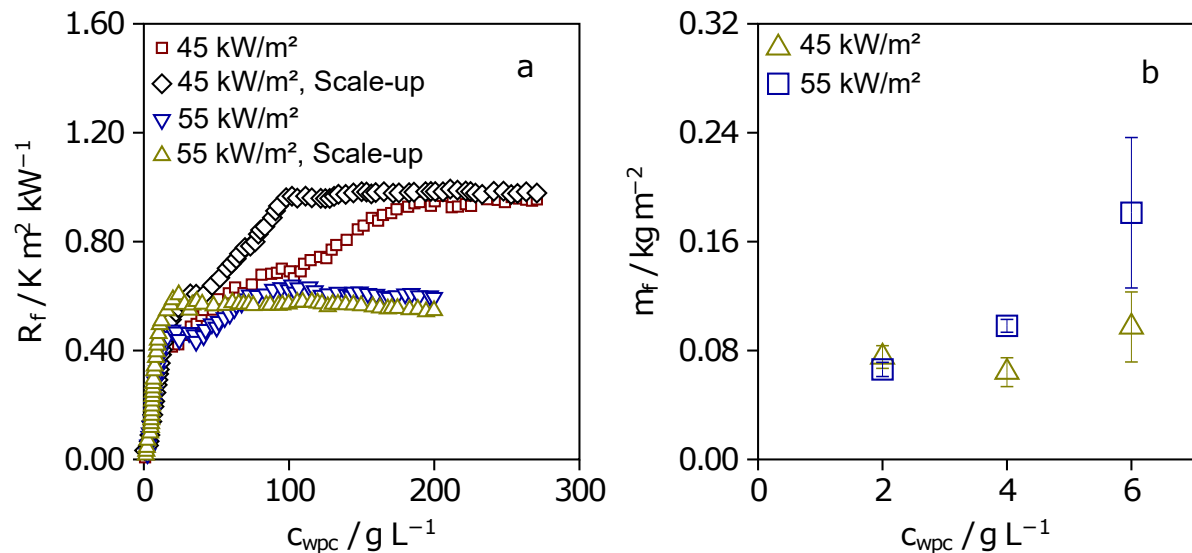


**Figure 3.7.:** Comparison of  $R_f$  for experimental set up versus scale-up at  $\text{Re } 2000$ ,  $40^\circ\text{C}$  bulk temperature (a) and  $m_f$  (b) of scale-up.

The scale-up results show a high deviation from the screening apparatus for  $45 \text{ kW/m}^2$ . This may be a reproducibility issue due to the low interfacial temperature and the small number of runs for each concentration. Also,  $m_f$  does not show the expected increase over  $c_{wpc}$  for  $45 \text{ kW/m}^2$ . For  $55 \text{ kW/m}^2$  results are consistent with the screening apparatus, showing the same dependency of  $c_{wpc}$ . Results of cleaning experiments are shown in Figure 3.8. After 250 minutes the fouling run end, heating is suspended and the channel is cleared of the fluid. The deposit is left to dry (s. Figure 3.9a). After 10 minutes (s. Figure 3.9b) the process is started again and heat transfer is resumed. While the process is heating up, the fouling resistance of SS returns to its value at the end of the fouling run, whereas the polymers remain near zero. Photos taken during the drying process show that within minutes the deposits contract on the polymer surfaces, whereas on SS no effect is visible. After restarting the process, fouling is easily removed from the polymers by the shear forces of the fluid, while the deposits remain on SS (s. Figure 3.9c). The cleaning of SS was only possible through chemical agents, such as sodium hydroxide solutions, as reported in literature [52–55]. This highlights another economic advantage TKT and PEEK have over SS, as plant downtime for cleaning can be reduced and no additional detergents are needed to run the polymer heat exchanger.

**Table 3.6.:** Experimental data of  $m_f$  for scale-up apparatus.

Material	Heat flux [ $\text{kW m}^{-2}$ ]	Concentration [ $\text{g L}^{-1}$ ]	$m_f$ [ $\text{kg m}^{-2}$ ]
PEEK	45	2	0.07523
PEEK	45	4	0.06411
PEEK	45	6	0.09732
PEEK	55	2	0.06613
PEEK	55	4	0.09815
PEEK	55	6	0.18122

Results of cleaning experiments are shown in Figure 10. After 250 minutes the fouling run

end, heating is suspended and the channel is cleared of the fluid. The deposit is left to dry (s. Figure 11a). After 10 minutes (s. Figure 11b) the process is started again and heat transfer is resumed. While the process is heating up, the fouling resistance of SS returns to its value at the end of the fouling run, whereas the polymers remain near zero. Photos taken during the drying process show that within minutes the deposits contract on the polymer surfaces, whereas on SS no effect is visible. After restarting the process, fouling is easily removed from the polymers by the shear forces of the fluid, while the deposits remain on SS (s. Figure 11c). The cleaning of SS was only possible through chemical agents, such as sodium hydroxide solutions, as reported in literature [7, 8, 25, 29]. This highlights another economic advantage TKT and PEEK have over SS, as plant downtime for cleaning can be reduced and no additional detergents are needed to run the polymer heat exchanger.

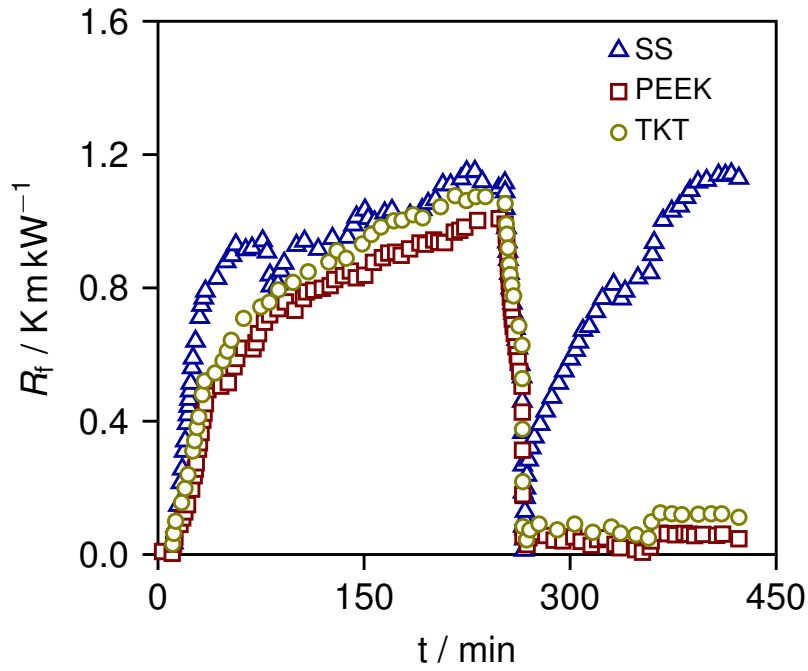


**Figure 3.8.:** Cleaning experiment on SS, PEEK, TKT at  $Re$  2000,  $45 \text{ kW/m}^2$ ,  $2 \text{ g/L}$ ,  $40^\circ\text{C}$  bulk temperature.

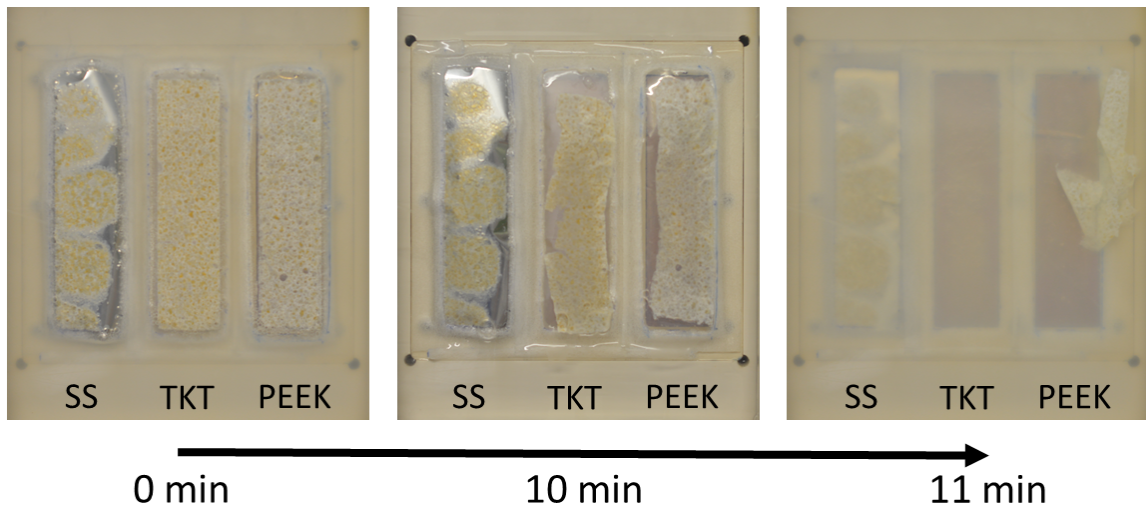


**Figure 3.9.:** Cleaning in process for SS, TKT, PEEK at  $Re$  2000,  $45 \text{ kW/m}^2$ ,  $2 \text{ g/L}$ ,  $40^\circ\text{C}$  bulk temperature starting at (a), after 10 minutes (b) and after 11 minutes when restarting the process (c).

### 3.7. Conclusions

Fouling is a major cost driver in the dairy industry, leading to frequent plant downtime and increased energy demand. In this paper the fouling behavior of PEEK and TKT was compared to benchmark stainless steel to find materials that mitigate fouling. For the first time PEEK and TKT were tested under technically relevant conditions of  $Re$  2000,  $40^\circ\text{C}$  bulk temperature,  $2\text{-}6 \text{ g/L}$  WPC concentration and  $45\text{-}55 \text{ kW/m}^2$  heat flux. Both polymers could maintain heat transfer under fouling conditions where steel could not. Using polymers led to a heat resistance reduction of up to 40%, making these materials an economically viable option for processes that have high whey protein concentration ( $\geq 4 \text{ g/L}$ ) or high heat fluxes ( $\geq 55 \text{ kW/m}^2$ ). Maintaining heat transfer is achieved through the evaporation of fluid under the fouling layer, which partly detaches the fouling from the surface. A long-term experiment showed that this behavior can be maintained for more than 15 hours of operation, without significantly decreasing the heat transfer at  $R_f$  values lower than  $1 \text{ Km}^2/\text{kW}$ , whereas a similar fouling resistance was measured on stainless steel after only 6 hours of run time. Experiments with a scale-up apparatus showed that these results are scalable. However, deposit mass showed that fouling continued to accumulate on the surface, and deposition increased by at least 50% when the WPC concentration was increased to 4 or 6 g/L. In contrast to stainless steel, the tested polymers enabled a fast and chemical-free cleaning in place procedure, in which the deposits were removed completely by restarting the process after a ten-minute drying phase. This allowed the heat transfer resistance to reset to its initial value at the start of the experiment. Both polymers showed great promise as a substitute for benchmark steel, as the polymers are economically and ecologically better alternatives to stainless steel.

No significant differences were measurable between TKT and PEEK. No effect of the higher roughness in TKT on fouling was observed. Therefore, TKT seems to be the most promising alternative to benchmark steel.



# 4. Predicting the fouling behavior of whey protein concentrate in polymeric heat exchangers

## *Contributor Roles Taxonomy*

Philipp Pelz: conceptualization; data curation; investigation; methodology; visualization; writing – original draft; writing – review & editing

*Chapter redrafted after the following main publication:*

P. Pelz, P. Egorov, J. Schulz, D. Lukas, S. Brune, R. Biedendieck, E. von Harbou, and H.-J. Bart "Predicting the fouling behavior of whey protein concentrate in polymeric heat exchangers," *Journal of Food Process Engineering*, 2025. DOI: <https://doi.org/10.1111/jfpe.70096>.

## **Abstract**

Fouling in heat exchangers, particularly in the dairy industry, presents significant operational challenges, increasing energy consumption and maintenance costs. Polymeric heat exchangers, with their favorable fouling mitigation behavior, offer a potential solution to reduce these impacts. A mechanistic and an empirical fouling model were developed to predict the unique detachment mechanism of whey protein concentrate (WPC) fouling layers on polyetheretherketone (PEEK) heat exchanger surfaces caused by boiling beneath the fouling deposits. Model parameters were estimated using experimental data of the total fouling mass. Fouling experiments were carried out for different process conditions. To identify the dependency of the model parameters on the process condition symbolic regression was applied. Previously unseen experimental data was used to validate the prediction capabilities of the models, which aim to predict fouling mass and in case of the mechanistic model thermal resistance. The results demonstrate that the empirical model predicts the fouling mass with an accuracy of  $\pm 20\%$  for untrained operating conditions within the boundaries of the training set. Larger deviations ( $< 70\%$ ) were observed for the mechanistic model. When predicting fouling mass outside the training data set, the empirical model fails to do so when extrapolating. While the mechanistic model provides better results compared to the empirical model when extrapolating, an error of  $< 130\%$  remains. The calculated thermal resistance shows discrepancies, particularly for high WPC concentrations and high heat flux. The findings suggest that PEEK heat exchangers may significantly reduce fouling-related downtime and energy costs in dairy processing.

## 4.1. Introduction

Milk fouling has been extensively researched and it is understood that  $\beta$ -lactoglobulin (BLG) is a key contributor to the formation of fouling [56, 57]. It is also known that the denaturation of BLG is contributing to fouling, however the exact mechanism has not been identified yet [58], as BLG can exist in many transient states before depositing [59]. When heated BLG exposes a free thiol group which can react with other thiol groups, similarly to free radicals in ordinary polymerization reactions such as ethene or ethylene monomers [59]. Therefore, a range of studies has been conducted to determine accurate denaturation models and to quantify reaction kinetics [60–62].

While most studies conclude that BLG fouling can be modeled by a two reactions approach, the first reaction being the denaturation of BLG and the second being agglomeration of BLG molecules, it remains unclear in which state BLG actually deposits and how the mass transfer takes place. Considerable work has been conducted on the models from de Jong [63] and Tolkach and Kulozik [64], while the model from de Jong providing easier implementation in modeling software due to the lack of discontinuous algebraic equations [65]. Besides the number of reaction models and kinetics several publications incorporated these models with success into heat exchanger simulations to predict fouling [50, 65–68]. Many publications validate the simulation, based on measurements, which can be fouling mass [66], fouling resistance [69] or thermal profiles [65].

Previously mentioned studies focus on the fouling behavior of metallic heat exchangers, while few publications covering the modeling of polymeric HX [67, 70], and no publication was found on modeling the fouling of WPC in polyetheretherketone (PEEK) based HX. PEEK can have significant fouling mitigating effects and can reduce cleaning times for various fouling components, such as  $\text{CaSO}_4$  (s. chapter 2) and  $\text{CaCO}_3$  [9, 10]. Chapter 3 showed that this is also the case for WPC fouling, with reduced fouling and better cleanability compared to benchmark stainless steel (SS). Furthermore, they found that the fouling layer partly detached from the polymer caused by nucleate boiling on the polymer surface and under the fouling layer. This detachment of the fouling layer results in a seemingly asymptotic fouling resistance (s. chapter 3), effectively limiting the heat transfer resistance despite the fact that the fouling layer continued to grow. This behavior was observed only for the two tested PEEK surfaces and not for SS.

This paper therefore aims to model the fouling phenomena of WPC on PEEK heat exchanger surfaces to predict the fouling layer mass and its impact on the heat transfer. This model can help dairy industries to find operating conditions that can minimize fouling and reduce the required energy to operate heating processes. Two approaches are compared based on their predictive accuracy: a purely empirical model and a mechanistic model, that aims to capture the physical dependencies based on first principles. While the empirical model is easy to use, implement and calculate, it may not be able to extrapolate as well as the mechanistic model and it cannot calculate any other parameters like the fouling induced thermal resistance  $R_f$ . Mechanistic models are computationally more demanding, but may be more suited to predict fouling behavior due to the underlying physical equations. Furthermore, the mechanistic model

describes not only the deposit mass but also unobservable parameters like the concentration of denatured and aggregated protein species and thereby they help to get a deeper understanding of the occurring processes. Due to the distinct fouling behavior of WPC on PEEK existing mechanistic models are modified to reflect the observed behavior. Experimental deposit mass data from chapter 3 as well as additionally conducted experiments are used to gain the best model parameters. The experiments were carried out under different process conditions of inlet concentration of WPC and heat flux. The parameters of both the mechanistic and the empirical model were estimated for each experiment so that the parameters were obtained as functions of the process conditions. Symbolic regression was performed to describe these functions. The regressions are then used to predict fouling mass and heat resistance (mechanistic model only) both within and outside the boundaries of the training data, which are validated with experimental data. Furthermore, the fouling related heat resistance  $R_f$  is used to validate results of the mechanistic model. Comparing the results of the two models reveals their respective advantages and disadvantages.

## 4.2. Modeling

### 4.2.1. Mechanistic model

The mechanistic fouling model used in this work is a one-dimensional model along the flow direction of the fluid  $x$  and is based mainly on the publications of Georgiadis and Macchietto [69], but also includes elements of de Jong, Choi, Jun, Nguyen, Rungraeng, Yi, Balasubramanian, Puri, and Lee, as well as adjustments which were needed to implement the observed boiling behavior (s. Sec. 4.2.1). This section focuses mainly on the modifications required to accommodate the fouling behavior of PEEK within the existing models and only briefly describes the basic principles of fouling modeling. The fundamental principles of fouling modeling are detailed in the previously cited sources, which the authors recommend for further reading.

The model encompasses the fluid volume over the heat transferring surface, which is divided into a small thermal boundary layer and the main bulk domain. The thermal layer forms at the interface to the HX wall and is of height  $\delta_T$  [13]:

$$\delta_T = \lambda_l / \alpha_0 \quad (4.1)$$

leaving a height of  $h_{\text{gap}} - \delta_T$  for the bulk flow, where  $h_{\text{gap}}$  is the height of the channel gap. The reaction scheme used in this work to model fouling is shown in Fig. 4.1. BLG reacts in both domains (boundary layer and bulk) in two reactions: first, native BLG (N) unfolds (U), exposing reactive thiol groups, which polymerize in a second reaction to form aggregates (A). Both reactions are assumed to be irreversible, with the first reaction being a first order reaction and the second reaction being a second order reaction [63]. The thermal boundary layer differs from the bulk domain in two ways: (i) the reactions (N\*, U\*, A\*) take place at the interface temperature  $T_I$  and (ii) deposits (D) are only formed from U\* inside the thermal boundary layer.

In contrast to Georgiadis and Macchietto [69], who considered deposition as mass transfer, it is modeled as a reaction in accordance with [67, 71]. Also, the component that deposits is the denatured BLG, as proposed by Choi, Jun, Nguyen, Rungraeng, Yi, Balasubramanian, Puri, and Lee, Pan, Chen, Mercadé-Prieto, and Xiao, instead of aggregated BLG, which was used in the model of Georgiadis and Macchietto [69]. An Arrhenius approach is used to model the reactions, parameters  $k_{0,i}$  and  $E_i$  can be found in Tab. 4.1.

$$k_i = k_{0,i} \exp\left(-\frac{E_i}{RT_K}\right), \quad \text{with } i = \text{N,U,A,D} \quad (4.2)$$

While [63] also estimated deposition parameters, these were found to not match with experimental data. This was also observed by [67, 71], who proposed that the rate constant  $k_D$  is a parameter that depends strongly on process conditions. Therefore, the rate constant is a parameter, denoted as  $p_1$ , that is estimated using measurement data. Similarly,  $E_D$  is estimated based on the experimental data. In contrast to  $p_1$ , its estimation relies solely on data from standard operating conditions (s. Sec. 4.3.3), which offers the largest dataset. Consequently,  $E_D$  is set to a fixed value of  $10.3 \text{ kJ mol}^{-1}$  across all operating conditions. Mass transfer between bulk and thermal layer is modeled for each species, using

$$k_{\text{MT},i} = D_i/\delta, \quad i = \text{N,U,A} \quad (4.3)$$

where  $D_i$  are the diffusion coefficients, which can be estimated using Wilke-Chang-Equation [69]

$$D_i = 1.31^{-17} \frac{T}{\mu V_i^{0.6}}, \quad i = \text{N,U,A} \quad (4.4)$$

where the molecular volume  $V_i$  can be calculated using the respective molecule diameters  $d_i$  and the Avogadro constant  $N_{\text{AV}}$

$$V_i = N_{\text{AV}}\pi d_i^3/6, \quad i = \text{N,U,A} \quad (4.5)$$

The molecule diameters can also be found in Table 4.1. The fluid boundary layer  $\delta$  (not to be confused with the thermal boundary layer  $\delta_T$ ) is dependent on Reynold (Re), Schmidt (Sc) and Sherwood number (Sh):

$$\delta = d_h/\text{Sh} \quad (4.6)$$

$$d_h = 4A_{\text{cr}}/C \quad (4.7)$$

$$\text{Sh} = 0.214(\text{Re}^{0.662} - 3.2)\text{Sc}^{0.4}, \quad \text{Re} = \frac{d_h \cdot v_x \cdot \rho_f}{\eta}, \quad \text{Sc} = \frac{\eta}{\rho_f D} \quad (4.8)$$

where  $d_h$  is the hydraulic diameter,  $A_{\text{cr}}$  is the cross-sectional flow area of the HX,  $C$  is the wetted circumference,  $v_x$  is the average velocity inside the channel,  $\eta$  is the dynamic viscosity and  $D$  is the diffusion coefficient of BLG in water.

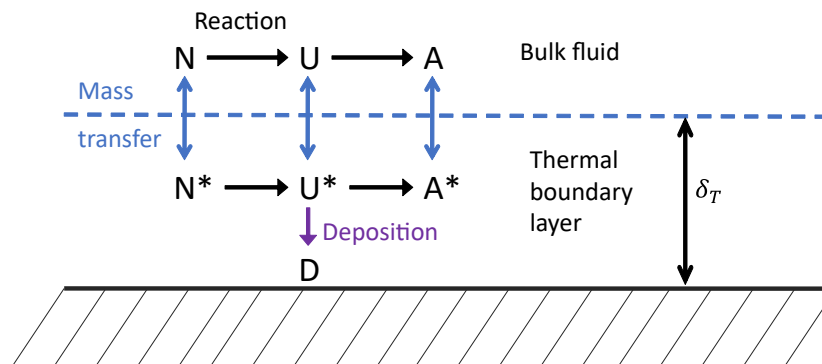


**Figure 4.1.:** Schematic illustration reaction and transport mechanism, adopted from Georgiadis and Macchietto [69] and Choi, Jun, Nguyen, Rungraeng, Yi, Balasubramanian, Puri, and Lee [67].

**Table 4.1.:** Parameters for the mechanistic fouling model, data from <sup>\*</sup>[63], <sup>†</sup> [72] and <sup>‡</sup> [55].

Description	Variable	Value	Unit
Native	$E_N^*$	261.4	$\text{kJ mol}^{-1}$
	$k_{N,0}^*$	$\exp(86.41)$	$\text{s}^{-1}$
	$D_N^\dagger$	$29 \times 10^{-10}$	m
Unfolding	$E_U^*$	288.5	$\text{kJ mol}^{-1}$
	$k_{U,0}^*$	$\exp(91.32)$	$\text{m}^3\text{kg}^{-1}\text{s}^{-1}$
	$D_U^\dagger$	$37 \times 10^{-10}$	m
Aggregation	$D_A^\dagger$	$77 \times 10^{-10}$	m
Deposition	$E_D$	10.3	$\text{kJ mol}^{-1}$
	$k_{D,0}$	$p_1$	$\text{s}^{-1}$
Fouling layer	$\lambda_f^\ddagger$	0.27	$\text{W}/(\text{mK})$
	$\rho_f$	307	$\text{kg m}^{-3}$

### Energy and material balances

The heat exchanger consists of a single, flat surface that is being heated. The model is based on the following assumptions:

- The flow rate and temperature profiles are uniform across the channel and plate width (plug flow).
- Heat losses to the environment are negligible.
- Changes in the composition of the inlet stream due to recirculation are negligible.
- The reaction of native BLG can be modeled with a first order reaction and the reaction of unfolded BLG can be modeled with a second order reaction [69].
- The fouling layer thickness is not considered and therefore does not impede fluid flow ( $v = \text{const.}$ ) or volume ( $h_{\text{gap}} = \text{const.}$ ).

The resulting equations based on the energy and mass conservation law are partial differential equations (PDE) :

$$V_x \rho_{l,x} c_{p,l} \left( \frac{\partial T}{\partial t} + v_x \frac{\partial T}{\partial x} \right) = U A_x (T_w - T) \quad (4.9)$$

where  $t$  denotes time,  $x$  is the position along the HX length  $L$ , which is also the flow direction and  $T$  is the bulk temperature.  $U$  is the overall heat transfer, which is calculated from its clean state  $U_0$  and the local Biot number  $Bi_i$

$$U(x) = U_0 / (1 + Bi(x)) = \left( \frac{1}{\alpha_1} + \frac{d_P}{\lambda_P} + \frac{d_f(x)}{\lambda_f} \right)^{-1}, \quad Bi(x) = \frac{d_f(x) U_0}{\lambda_f} \quad (4.10)$$

$$U_0 = \left( \frac{1}{\alpha_1} + \frac{d_P}{\lambda_P} \right)^{-1} \quad (4.11)$$

$d_f(x)$  is the local thickness and  $\lambda_f$ ,  $\lambda_P$  are the heat conductivities of the fouling layer and PEEK.  $\alpha_1$  can be experimentally calculated, using the measured wall temperature  $T_w(t=0)$

$$\alpha_1 = \frac{1}{\frac{T_w(t=0) - T_{Bulk}}{\dot{q}} - \frac{d_P}{\lambda_P}} \quad (4.12)$$

$U_0$  and  $U(x)$  can be used to determine the fouling resistance  $R_f$ , which is commonly used to quantify the impact of fouling on the thermal HX performance

$$R_f = \frac{1}{U_0} - \frac{1}{U(x)} \quad (4.13)$$

For the mass balances the following assumptions are made:

- No diffusion is considered in the axial direction (plug-flow).
- Concentrations are uniform across the channel and plate width (ideally mixed).
- Changes in the inlet concentration due to recirculation are negligible.
- The reaction of native BLG can be modeled with a first order reaction and the reaction of unfolded BLG can be modeled with a second order reaction [69].

This leads to the following partial differential equations (PDE) for each component in the bulk layer :

$$\frac{\partial C_N}{\partial t} + v_x \frac{\partial C_N}{\partial x} = -k_{N,0} \exp\left(-\frac{E_N}{RT_i}\right) C_N - \frac{k_{MT,N}}{h_{gap} - \delta_t} (C_N - C_N^*) \quad (4.14)$$

$$\begin{aligned} \frac{\partial C_U}{\partial t} + v_x \frac{\partial C_U}{\partial x} = & +k_{N,0} \exp\left(-\frac{E_U}{RT_i}\right) C_{Ni} - k_{U,0} \exp\left(-\frac{E_U}{RT_i}\right) C_{Ui}^2 \\ & - \frac{k_{MT,U}}{h_{gap} - \delta_t} (C_U - C_U^*) \end{aligned} \quad (4.15)$$

$$\frac{\partial C_A}{\partial t} + v_x \frac{\partial C_A}{\partial x} = k_{U,0} \exp\left(-\frac{E_U}{RT_i}\right) C_{Ui}^2 - \frac{k_{MT,A}}{h_{gap} - \delta_t} (C_A - C_A^*) \quad (4.16)$$

Similarly, for the thermal boundary layer (denoted by \*) the balances are:

$$\frac{\partial C_N^*}{\partial t} + v_x \frac{\partial C_N^*}{\partial x} = -k_{N,0} \exp\left(-\frac{E_N}{RT_I}\right) C_N^* + \frac{k_{MT,N}}{h_{\text{gap}} - \delta_t} (C_N - C_N^*) \quad (4.17)$$

$$\begin{aligned} \frac{\partial C_U^*}{\partial t} + v_x \frac{\partial C_U^*}{\partial x} &= k_{N,0} \exp\left(-\frac{E_U}{RT_I}\right) C_{Ni}^* - k_{U,0} \exp\left(-\frac{E_U}{RT_I}\right) C_{Ui}^{*2} \\ &+ \frac{k_{MT,U}}{h_{\text{gap}} - \delta_t} (C_U - C_U^*) - k_{D,0} \exp\left(-\frac{E_D}{RT_I}\right) C_{Ui}^* \end{aligned} \quad (4.18)$$

$$\frac{\partial C_A^*}{\partial t} + v_x \frac{\partial C_A^*}{\partial x} = k_{U,0} \exp\left(-\frac{E_U}{RT_I}\right) C_{Ui}^{*2} + \frac{k_{MT,A}}{h_{\text{gap}} - \delta_t} (C_A - C_A^*). \quad (4.19)$$

The local deposition mass flow  $\dot{m}_D(x)$  and local thickness growth rate  $\dot{d}_f(x)$  can be calculated directly from Eq. (4.18)

$$\dot{m}_D = A_x \delta_t k_{D,0} \exp\left(-\frac{E_D}{RT_I}\right) C_{Ui}^* \quad (4.20)$$

$$\dot{d}_f = \frac{\dot{m}_D}{\rho_f} \quad (4.21)$$

where  $\rho_f = 307 \text{ kg m}^{-3}$  is the apparent fouling layer density (solid mass per total volume, excluding any mass contribution from the liquid). This value is low compared to other publications, where a density around  $\rho_f = 1000 \text{ kg m}^{-3}$  [66, 68] is used. It is not specified which specific density this value represents. The lower density value in this work is used to calculate the fouling mass from the solid deposition concentration, which requires the apparent density. It provided better agreement with experimental data compared to  $\rho_f = 1000 \text{ kg m}^{-3}$ .

### Initial and boundary conditions

At the beginning of the simulation it is assumed that a constant thermal profile has been established with a non-fouling fluid, which was experimentally also the case using deionized water. Furthermore, WPC has just been added to the system. Then the following initial conditions can be made:

$$T_i(t=0) = T_{\text{in}} \quad \forall x \in [0, \dots, L] \quad (4.22)$$

$$C_N(t=0) = C_N^*(t=0) = C_{\text{in}} \quad \forall x \in [0, \dots, L] \quad (4.23)$$

$$C_U(t=0) = C_U^*(t=0) = C_A(t=0) = C_A^*(t=0) = 0 \quad \forall x \in [0, \dots, L] \quad (4.24)$$

Since the thermostat keeps the bulk temperature constant, the depositing fouling mass is small in comparison to the whey protein mass in the plant and the bulk temperature is too low for denaturation [1], the following boundary conditions apply:

$$T(x=0) = 40^\circ\text{C} \quad \forall t \in [0, \dots, t_{\text{end}}] \quad (4.25)$$

$$C_j(x=0) = C_j^*(x=0) = 0 \quad \forall t \in [0, \dots, t_{\text{end}}], \quad \forall j = U, A \quad (4.26)$$

$$C_N(x=0) = C_N^*(x=0) = C_{\text{in}} \quad \forall t \in [0, \dots, t_{\text{end}}] \quad (4.27)$$

## Boiling

In chapter 3 falling or constant  $R_f$  values at high WPC concentrations and heat fluxes were observed. This was found to be due to boiling of liquid underneath parts of the fouling layer, which led to constant block temperatures  $T_w = T_{w,\text{boil}}$  and allowed heat to be transferred without being impeded by fouling. It was found that  $120^\circ\text{C} \leq T_{w,\text{boil}} \leq 135^\circ\text{C}$  depends on  $\dot{q}$  and its calculation requires information about the detached area on the HX, channel size of the fouling layer, fluid temperature inside the detached area, liquid flow and other parameters, which are all unknown. Therefore, the maximum temperature of  $T_w$  in the model is set to the experimentally observed  $T_{w,\text{boil}}$  for each operating condition. It was also found that the layer grew at a decreased rate in the boiling state compared to the growth at non boiling conditions. This means that the fouling resistance  $R_f$  (s. Eq. (4.13)) and  $m_f$  are not proportional and modifications to the model are required in order to ensure an accurate replication of the observed behavior.

After an experiment has started, the fouling layer begins to grow and heat is transported to the fluid as shown for a single HX element  $i$  in Fig. 4.2 A). Since the constant heat flow has to pass the fouling layer,  $T_w$  has to increase over time to compensate for the increasing heat resistance caused by the growing fouling layer. The fouling layer traps fluid in its pores, which starts to boil when the wall temperature reaches  $T_{w,\text{boil}}$  (s. Fig. 4.2B). This detaches sections of the fouling layer, creating small volumes of boiling fluid between the PEEK material and the fouling layer. Over time, channels form in the direction of the bubbles ascent, which is along the direction of flow. This behavior was experimentally observed in chapter 3.

In order to be able to calculate the resulting fouling behavior a series of strong assumptions have to be made:

- Material properties of the fouling layer are constant ( $\lambda_f$ ) and the fouling surface area is the same as the heat exchanger surface ( $A_{f,i} = A_{\text{HX},i}$ ,  $\forall i$ ).
- Even though only a small part of the fouling layer detaches from the surface, it is assumed that all of  $\dot{Q}_{\text{const}}$  is used to boil liquid at  $T_{\text{boil}} = 100^\circ\text{C}$ .
- Only some part  $\dot{Q}_{\text{cond}}$  of  $\dot{Q}_{\text{const}}$  is conducted through the fouling layer.
- The remaining energy of  $\dot{H}_{\text{boil}} = \dot{Q}_{\text{const}} - \dot{Q}_{\text{cond}}$  bypasses the fouling layer by either passing through the pores or a lifted edge of the fouling layer as vapor or liquid.
- Mass transport through the pores increases the temperature in the layer and decreases the heat resistance provided by  $d_f/\lambda_f$ , which leads to an increased  $T_I$  compared to a heat transfer of only  $\dot{Q}_{\text{cond}}$ .
- Liquid is always present in the pores and replenished from the bulk medium. Since the required amount of liquid is small ( $<0.5\%$  of  $\dot{m}_{\text{bulk}}$ ) in comparison to the bulk flow, any effects on the main flow are neglected.

Changes in the heat transfer behavior can drastically effect fouling through its impact on the interfacial temperature  $T_I$ , which determines the temperature in the boundary layer (s.

Eq. (4.17)–(4.19)). Since  $T_I$  cannot be calculated directly, it is regressed using experimental data via

$$T_I = T_{\text{cond}} + p_2(T_{\text{boil}} - T_{\text{cond}}) \quad (4.28)$$

where  $p_2$  is a parameter that is estimated based on experimental data,  $T_{\text{boil}} = 100^\circ\text{C}$  is the highest possible temperature, meaning that the fouling layer did not pose a heat resistance at all and  $T_{\text{cond}}$ , which is the lowest possible temperature that  $T_I$  would be, if heat was only transferred through the fouling layer by conduction at  $T_{\text{boil}}$

$$T_{\text{cond}} = T_{\text{boil}} - \frac{\dot{Q}_{\text{cond}}}{\left(\frac{1}{\alpha_{\text{boil}}} + \frac{d_f}{\lambda_f}\right)^{-1} A_{\text{HX}}} \quad (4.29)$$

Assuming no interference of boiling, the unknown parameters of  $\dot{Q}_{\text{cond}}$  and  $\alpha_{\text{boil}}$  can be estimated.  $\dot{Q}_{\text{cond}} < \dot{Q}_{\text{const}}$  is a reduced heat flow of

$$\dot{Q}_{\text{cond}} = A_{\text{HX}} \left( \frac{1}{\alpha_{\text{boil}}} + \frac{d_f}{\lambda_f} + \frac{1}{\alpha_1} \right)^{-1} (T_{\text{boil}} - T_{\text{Bulk}}) \quad (4.30)$$

$\dot{Q}_{\text{const}}$  is completely transferred through the PEEK material and boils fluid on the surface at  $T_{\text{boil}}$ , therefore

$$\dot{Q}_{\text{const}} = A_{\text{HX}} \left( \frac{d_P}{\lambda_P} + \frac{1}{\alpha_{\text{boil}}} \right)^{-1} (T_w - T_{\text{boil}}) \quad (4.31)$$

From which  $\alpha_{\text{boil}}$  can be calculated as

$$\alpha_{\text{boil}} = \frac{1}{(T_w - T_{\text{boil}}) A_{\text{HX}} / \dot{Q}_{\text{const}} - d_P / \lambda_P} \quad (4.32)$$

Assuming the heat transfer coefficient  $\alpha_{\text{boil}}$  is identical on both interfaces of the boiling layer, the resulting heat flow  $\dot{Q}_{\text{cond}}$  can then be calculated using Eq. (4.30). The remaining heat flow  $\dot{H}_{\text{boil}} = \dot{Q}_{\text{const}} - \dot{Q}_{\text{cond}}$  bypasses the fouling layer by exiting at lifted edges of the fouling layer or by passing through the pores and increasing  $T_I$  according to Eq.(4.28).

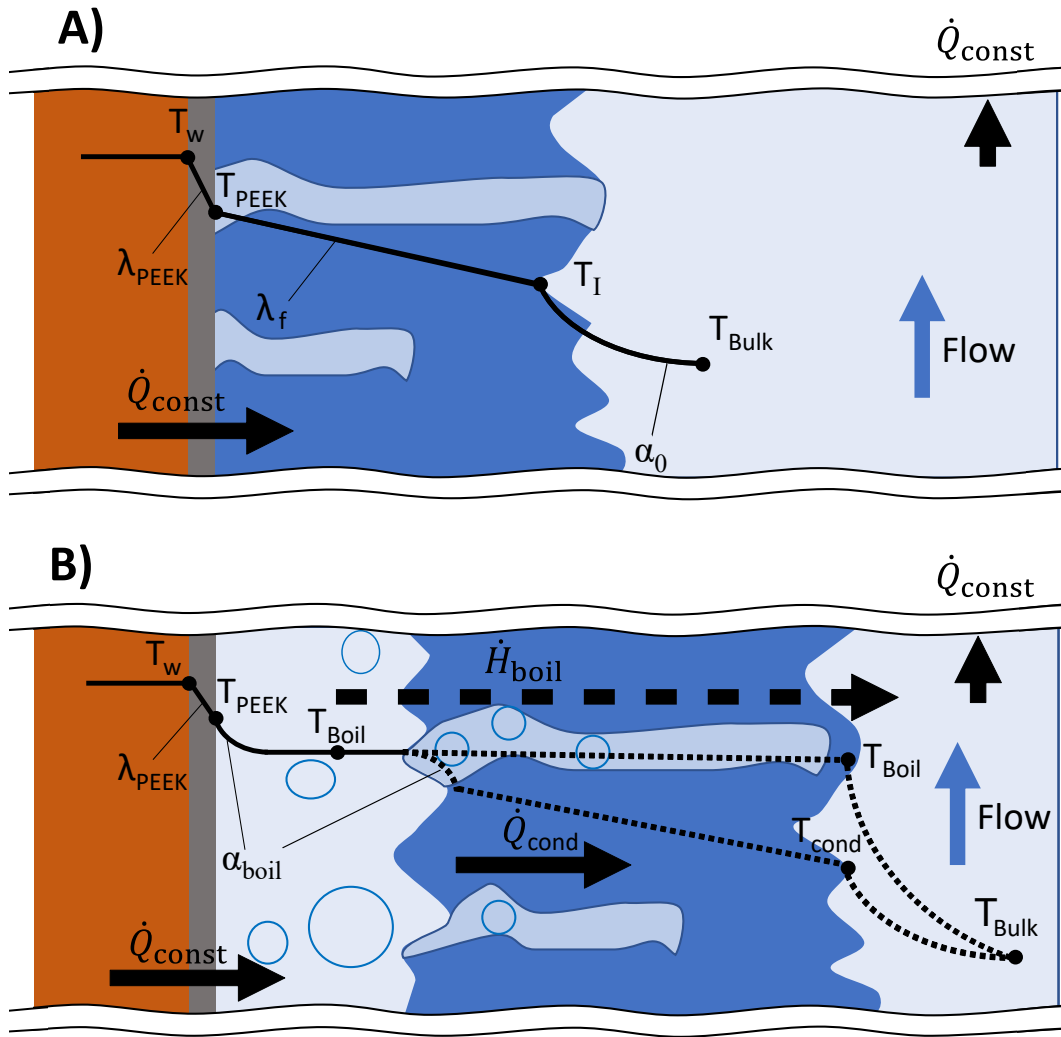


**Figure 4.2.:** Schematic illustration of heat transfer through fouling layer without (A) and with (B) boiling.

#### 4.2.2. Empirical model

The empirical model describes the observed deposit mass (starting from a clean surface) as a function of time, see Eq. (4.33). Two parameters  $A$  and  $B$  are employed to fit the model for each operating conditions to the corresponding measurements. This form of function was chosen due to its simplicity and good agreement with the observed data.

$$m_{f,emp} = A \log_{10}(Bt + 1) \quad (4.33)$$

### 4.3. Experimental data

#### 4.3.1. Experimental setup

The experimental setup in Section 2.3.1, comprising a screening and a scale-up channel, is used for additional experiments beyond those in chapter 3. Heat exchanger parameters can be found in Table 4.2.

**Table 4.2.:** Heat exchanger parameters

Symbol	Description	Value	Unit
$L$	Length of HX & copper block	0.08	m
$L_w$	Width of copper block	0.02	m
$T_{\text{boil}}$	Boiling temperature	373.15	K
$\dot{V}$	Volumetric flow rate	$8.17 \times 10^{-5}$	$\text{m}^3 \text{s}^{-1}$
$T_{\text{in}}$	Inlet temperature (bulk)	313.15	K
$h_{\text{gap}}$	Height of fluid volume	$7 \times 10^{-3}$	m
$L_{w,\text{channel}}$	Width of HX channel	0.116	m
$A_{\text{cr}}$	HX cross-sectional area	$8.12 \times 10^{-4}$	$\text{m}^2$
$A_x$	HX area of discretization element	$1.6 \times 10^{-4}$	$\text{m}^2$

#### 4.3.2. Methods and materials

The investigated heat transfer materials were SS, PEEK and TKT, which were obtained as described in Section 2.3.2. High grade whey protein was used for the experiments as detailed in Section 3.4.

#### 4.3.3. Operating procedure

The experiments followed the operating procedure outlined in Section 3.5. All investigated operating conditions were conducted with a Reynolds number of  $\text{Re} = 2000$  and  $T_{\text{Bulk}} = 40$  °C. Varied operating conditions were WPC concentration and heat flux. The most extensively tested operating condition of  $\dot{q} = 45 \text{ kW/m}^2$ ,  $c_{\text{wpc}} = 2 \text{ g/L}$  is hence forth called standard operating condition (SOC). A comprehensive list of all operating conditions can be found in Tab. 4.3.

**Table 4.3.:** List of experimental data, where (\*) marks data that has been taken from Chapter 3.

No.	$c_{wpc}$ $\text{g L}^{-1}$	$\dot{q}$ $\text{kW m}^{-2}$	$t$ h	$m_f$ $\text{g m}^{-2}$	No.	$c_{wpc}$ $\text{g L}^{-1}$	$\dot{q}$ $\text{kW m}^{-2}$	$t$ h	$m_f$ $\text{g m}^{-2}$
1*	2	45	3.0	57.4	22*	4	55	3.0	91.9
2*	2	45	4.6	72.8	23*	4	55	3.0	87.5
3*	2	45	4.6	75.4	24*	4	55	3.6	112.4
4*	2	45	14.9	122.2	25*	4	55	3.6	103.5
5	2	45	0.5	6.9	26*	4	55	2.8	83.7
6	2	45	1.0	14.1	27*	4	55	2.8	96.0
7	2	45	2.0	37.2	28*	6	55	4.2	168.1
8	2	45	4.1	66.8	29*	6	55	4.2	181.2
9	2	45	7.0	73.1	30	6	55	2.0	85.0
10	2	45	11.0	110.2	31	2	65	2.0	46.5
11*	4	45	6.0	64.1	32	2	65	5.0	88.5
12*	4	45	5.5	96.7	33	2	65	7.0	114.8
13	4	45	2.0	38.6	34	4	65	2.0	85.6
14*	6	45	5.5	79.1	35	4	65	4.9	384.1
15*	6	45	4.2	115.5	36	6	65	2.0	146.0
16*	6	45	3.3	113.1	37	6	65	5.0	429.0
17	6	45	2.0	68.4					
18*	2	55	3.3	62.5			Validation Data		
19*	2	55	3.3	61.9	38	5	50	5.0	177.4
20*	2	55	3.3	62.4	39	3	60	5.0	94.5
21	2	55	7.0	96.1	40	10	65	5.0	548.4

#### 4.3.4. Data post-processing

Post-processing of data is necessary to be able to compute and compare experimental fouling heat resistance  $R_{f,\text{exp}}$  with the mechanistic model prediction  $\hat{R}_{f,\text{mech}}$ . Equation (2.7) is used to evaluate  $R_{f,\text{exp}}$  during the experiments.

#### 4.3.5. Accuracy of the measurements

Measurement accuracy of  $m_f$  and  $R_f$  for the experimental setup has been detailed in Section 3.6. It is noteworthy that only the final measurements were utilized for reproducibility testing, rather than the entire dataset. Consequently, the observed low standard deviation may not fully capture potential variations occurring throughout the duration of the experiment.

**Table 4.4.:** Accuracy of  $R_f$  and  $m_f$  measurements as well as respective standard deviation at SOC (s. Chapter 3).

Type	Mean	Standard Deviation
$R_f / \text{m}^2 \text{K kW}^{-1}$	1.04	0.066
$m_f / \text{kg m}^{-2}$	0.05505	0.01814

#### 4.3.6. Optimization

The model parameters were estimated by solving the minimization problem given in Eq. (4.34)–(4.35). The mean squared error was used as objective function. The parameter estimation was carried out for each set of experimental data. Therefore, for each operating condition a set of model parameters is obtained. In order to accurately calculate the fouling behavior, the model parameters are optimized based on experimental  $m_f$  data. As conducting experiments is time-consuming and cost-intensive, the number of experiments had to be kept to a minimum. However, a relatively high number of data points is needed to robustly perform the optimization.

The error functions  $f$ , are calculated using mean squared error (MSE):

$$\min_p f(m_f(t), \hat{m}_{f,\text{emp}}(t, A, B)) = \min_p \frac{1}{n} \sum_{j=1}^n (m_{fj}(t) - \hat{m}_{f,\text{emp}j}(t, p))^2 \quad (4.34)$$

$$\min_{A,B} f(m_{f,\text{emp}}(t), \hat{m}_{f,\text{mech}}(t, A, B)) = \min_{A,B} \frac{1}{n} \sum_{j=1}^n (m_{f,\text{emp}j}(t) - \hat{m}_{f,\text{mech}j}(t, A, B))^2 \quad (4.35)$$

where  $n$  is the number of observations,  $m_{fj}$  is the  $j$ th experimental value,  $\hat{m}_{f,\text{emp}j}$ ,  $\hat{m}_{f,\text{mech}j}$  is the  $j$ th simulated value. The parameters of the mechanistic model that were fitted to the experimental data are the deposition constant  $k_{0,D}$ , see Eq. (4.2) (in the following denoted with  $p_1$ ) and the parameter  $p_2$  that determines the surface temperature after boiling occurs according to Eq. (4.28). It is noteworthy that the influence of temperature and WPC concentration is already incorporated into the Arrhenius equation. The need for adjustable parameters  $p$  indicates that this model can not fully explain the impact of these operating conditions alone. A possible cause is that the reaction order of the used model does not fit well with experimental results. For the empirical model the optimization parameters are  $A$  and  $B$ . To quantify the goodness of fit, the range-based normalized root mean squared error (NRMSE) is used:

$$\text{NRMSE} = \frac{\sqrt{\text{MSE}}}{m_{f,\text{max}} - m_{f,\text{min}}} \quad (4.36)$$

where  $m_{f,\text{max}}$ ,  $m_{f,\text{min}}$  are the maximum and minimum observed values. Due to its normalization, NRSME allows the comparison between simulation and experimental data for different variables types such as  $m_f$  and  $R_f$ . The fouling resistance, which is calculated according to Eq. (2.7), is used to compare the mechanistic optimization with experimental data.

### 4.3.7. Symbolic regression

As previously outlined, the model parameters were estimated for each operating condition (for details s. Section 4.3.8). The preliminary studies did not yield any evident and straightforward trends regarding the dependence of the model parameters on the operating conditions. Additionally, there are currently no established physical laws that can adequately describe these relationships. However, to enable the prediction of fouling behavior for operating conditions that have not been subjected to experimental investigation, a symbolic regression was conducted to describe the model parameters as a function of the operating conditions across a broad parameter range.

Unlike traditional regression methods, which assume a specific model form (such as linear, polynomial, or exponential) and estimate the parameters of that model, symbolic regression searches for both the model and its parameters. This means that the output is an interpretable model, which can quantify dependencies of the input variables. After a regression function has been found for the model parameters,  $m_f$  can be calculated either by means of the mechanistic or the empirical model directly for untested operating conditions by using the values of the model parameters provided by the regression functions.

A disadvantage of symbolic regression is that it can easily lead to overfitting, which must be controlled by limiting the complexity of the output functions. This can be done by adjusting the regression setup. The used settings can be found in Section 4.3.9. Finally, the accuracy of the approaches is evaluated by comparing the predicted  $\hat{m}_f$  values with measured  $m_f$  values that were not used for the parameter estimation.

### 4.3.8. Parameter estimation

The modeling procedure applied in this study is shown in Figure 4.3. Parameters of the models are estimated using an experimental training dataset (s. Tab 4.3). For the empirical model, the experimental  $m_{f,\text{exp}}$  results are used directly for this optimization. Since conducting experiments is time-consuming and cost-intensive, the number of experiments had to be kept to a minimum, which means that  $m_{f,\text{exp}}$  is not equidistantly spaced and contains experimentally induced deviations. The numerical solver (s. Section 4.3.9) would overemphasize areas that contain more data points compared to areas where few data points are available if that data would be passed directly. Despite generating more data per run due to its online measurement,  $R_f$  values are not utilized for model optimization. This is due to the error-prone measurement and external influences that can affect the measurement. For example, degassing air bubbles on the surface of the heat exchanger can add an additional heat transfer resistance, suggesting a higher fouling rate which is a known problem [73–75], or inaccurate fouling properties such as  $\lambda_f$  which is reasonable when considering the range of reported values of  $0.084 \text{ W}/(\text{mK}) < \lambda_f < 3 \text{ W}/(\text{mK})$  in literature [50, 54]. Therefore, the mechanistic model needs post-processed  $m_{f,\text{exp}}$  data as input for the optimization. This data is provided by the empirical model output  $m_{f,\text{emp}}$ . Consequently, the mechanistic model can only reflect the training set as well as the empirical model. The model output is then compared to the training data. Furthermore, for validation of the models with unseen experimental data, symbolic regressions are performed

on the respective model parameters. The parameters are then used to predict  $\hat{m}_f$  and  $\hat{R}_f$  (mechanistic model only). In order to be able to determine  $\hat{R}_f$ , the mechanistic model must be provided with the  $T_{w,boil}$  of the respective operating condition (s. Sec. 4.2.1). Since this information is not available in the model validation procedure,  $T_{w,boil}$  is estimated using interpolation. Results are then compared to the measured values for validation. The following sections describe the individual steps of the procedure as well as their implementation in detail.

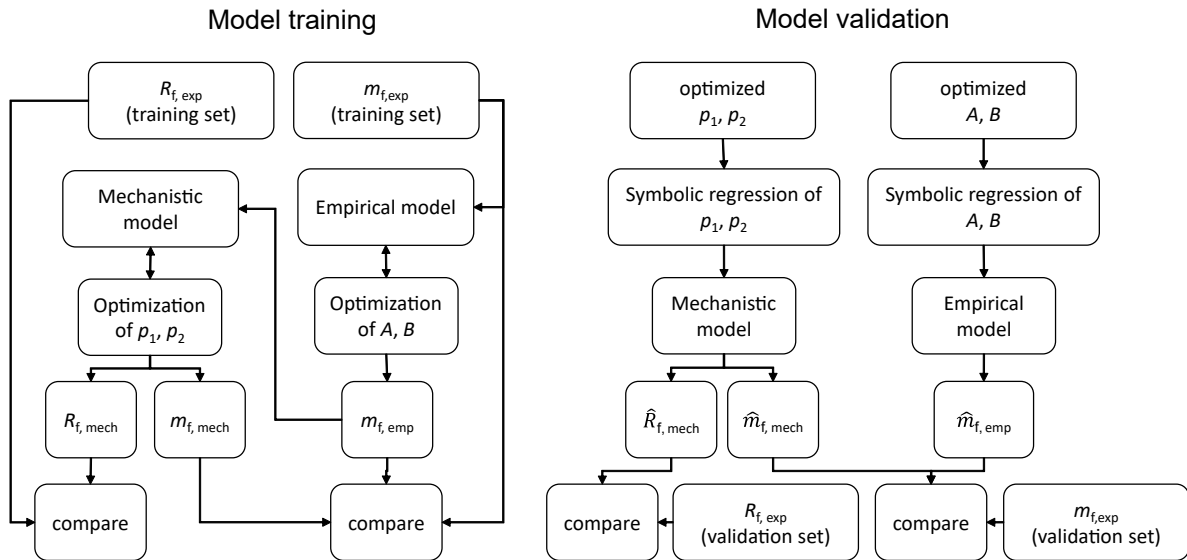


Figure 4.3.: Schematic illustration of the model training and validation strategy.

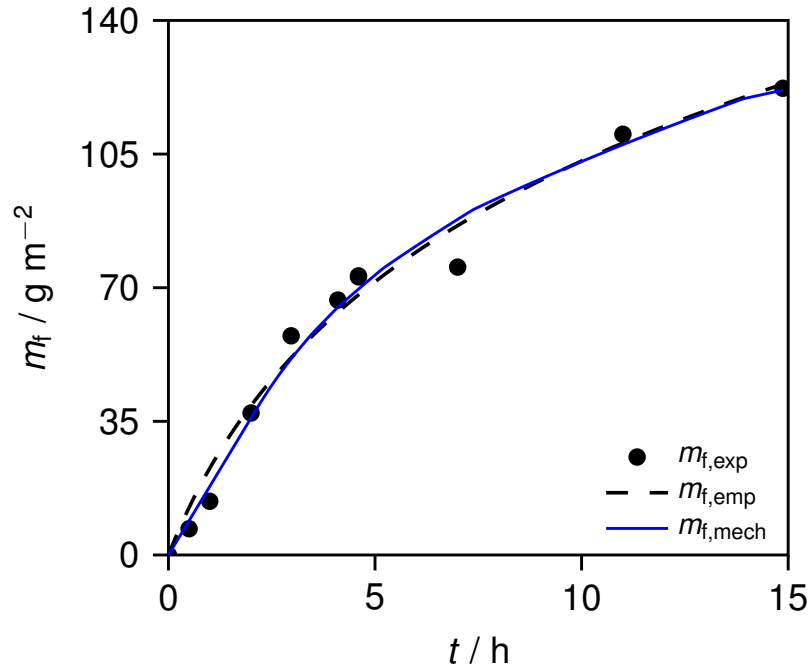
#### 4.3.9. Implementation

In order to solve the PDE of the mechanistic model detailed in Section 4.2.1, the equations are discretized along the spatial coordinate  $x$  using backward differences. Thereby, a set of ordinary differential equations (ODE) is obtained. The number of elements used was  $n = 10$ . This results in an ODE system with 80 equations, consisting of  $6n$  material balances,  $n$  energy balances and  $n$  calculations for  $\dot{d}_f$ . As stated in Section 4.2.1, the boiling temperature  $T_{w,boil}$  cannot be calculated from the underlying physical equations. All calculations were performed in Version 1.10 of the Julia programming language [76]. A complete list of used packages can be found in Table C.1. The ODEs were solved using the TRBDF2 solver of the DifferentialEquations.jl package. The empirical model parameters  $A$  and  $B$  were fitted to experimental data using the `curve_fit` function from the LsqFit.jl package. Optimization parameters  $p_1$  and  $p_2$  were calculated using NelderMead algorithm of the Optim.jl package. Symbolic regressions were performed using the `EquationSearch` and `calculate_pareto_frontier` functions of packages SymbolicUtils.jl and SymbolicRegression.jl with options listed in Table C.2.

## 4.4. Results

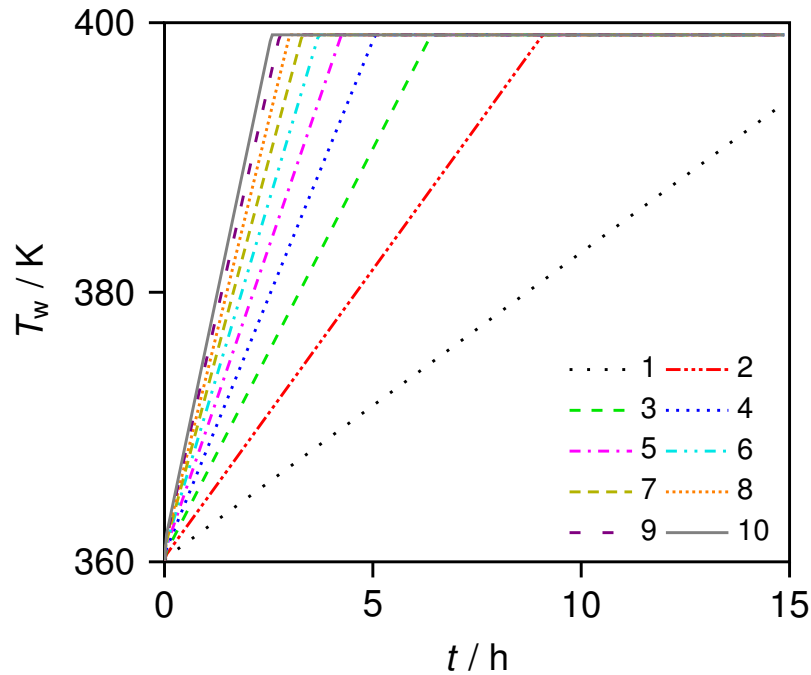
Figure 4.4 shows a comparison of the fouling mass growth over time for experimental results and model prediction at SOC. Results show that the models are able to predict fouling mass

accurately. The corresponding  $\text{NRMSE} = 0.05$  for the empirical and  $\text{NRMSE} = 0.047$  for the mechanistic model support that the optimizations of both models are in good agreement with experimental data. The kinks in the curve for the mechanistic model are caused by the regime change to boiling at the respective position along the HX.



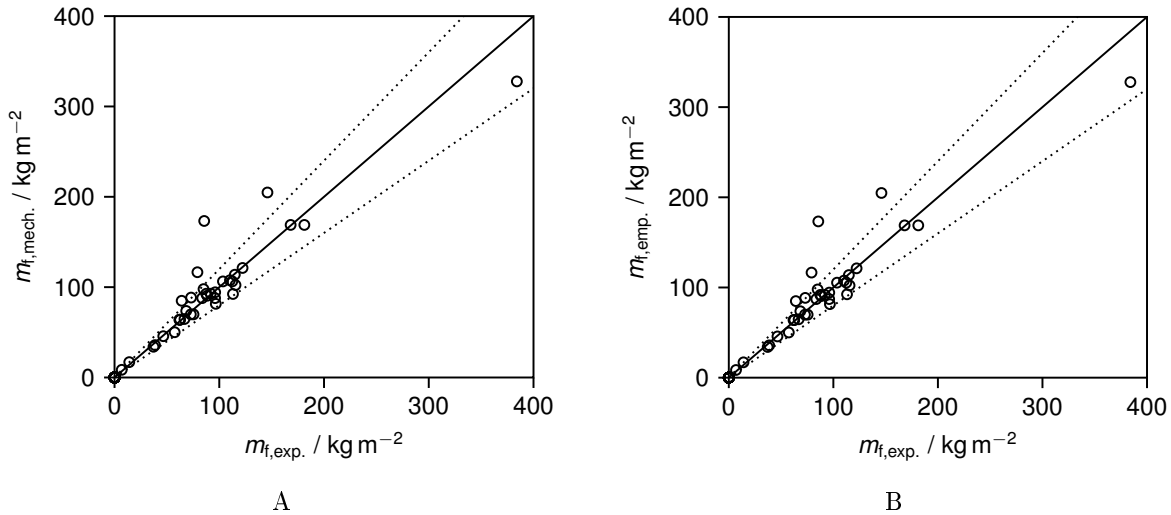
**Figure 4.4.:** Comparison of the experimental data and the model prediction of the fouling deposit mass for the standard operating conditions (SOC). Symbols: experimental data. Solid line: mechanistic model. Dashed line: empirical model.

Figure 4.5 visualizes the wall temperature  $T_w$  along the length of the HX over time. Results show that  $T_{w,\text{boil}} = 393\text{K}$  is not reached simultaneously across the length of the HX. Instead, the onset of boiling initially occurs at the terminal section of the heat exchanger and subsequently propagates upstream towards the inlet section.



**Figure 4.5.:** Prediction of the wall temperature for different axial positions ( $1 = L/10$ ,  $2 = 2L/10$ , ...,  $10 = L$ ) as a function of time at standard operating conditions.

For other operating conditions low NRMSE values were also obtained for both models in regard to  $m_{f,\text{exp}}$  (s. Tab. C.5). This means that the optimizations worked well across all tested operating conditions. Figure 4.6 compares each measured deposit mass to the mechanistic (Fig.4.6A) and empirical model (Fig.4.6B). Results show that both models deliver almost identical values for each operating condition. Except for 4 measurements all points lie well within a margin of  $\pm 20\%$ , which is marked by the dotted lines. However, it is important to note that due to variation in the data and the relatively small amount of experimental points for some operating conditions low ( $4 \text{ kg m}^{-3}$ ,  $55 \text{ kW m}^{-2}$ ) or very high ( $2 \text{ kg m}^{-3}$ ,  $55 \text{ kW m}^{-2}$ )  $R^2$  values were obtained for the empirical model fit (s. Tab. C.3). This is problematic for low  $R^2$  values as higher deviations are to be expected for both models when comparing results with experimental data. Parameter values for each operating condition can be found in Table C.3 and C.4.



**Figure 4.6.:** Comparison of  $m_{f,exp}$  with  $m_{f,mech}$  (A) and  $m_{f,emp}$  (B) for all experimental runs in the test dataset. The dotted lines mark  $\pm 20\%$   $m_{f,exp}$

A comparison of the fouling resistance between experimental and model values for SOC is shown in Figure 4.7. It is important to acknowledge that the simulated results for fouling heat resistance are purely predictive in nature, as no experimental data of the fouling heat resistance were utilized during the parameter estimation procedure.

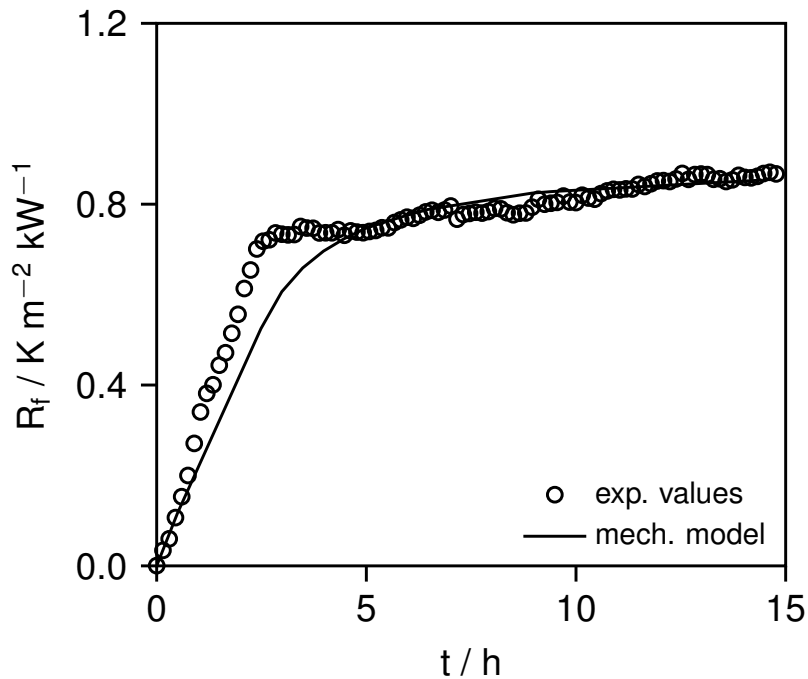


**Figure 4.7.:** Comparison of experimental data (symbols) and model prediction (line) of the fouling heat resistance for the standard operation conditions.

The experimental curve is characterized by two distinct areas: a steep linear growth phase followed by an almost flat linear phase, which indicates the boiling phase. The model behavior also starts with a linear slope, but deviations occur due to a lower incline compared to the experimental data. The model does not show the clear distinction between the linear slope and

the boiling phase, but instead predicts a smoother transition between regimes. This is caused by the wall temperature  $T_w$  not reaching  $T_{w,\text{boil}}$  simultaneously across the HX length (s. Fig. 4.5) and is directly impacting  $R_{f,\text{mech.}}$  considering Eq. (2.7). Therefore, fouling thickness must be unevenly distributed in the modeled HX, which was not experimentally observed and is most likely result of the depositing concentration  $c_U^*$  distribution across the elements. This indicates that deposition is controlled by the denaturation reaction ( $N^* \rightarrow U^*$ ). Overall a good agreement between estimated and measured  $R_f$  was reached for SOC.

For other operating conditions larger deviations in  $R_f$  were found, with the highest NRMSE=0.26 for operating conditions of  $2 \text{ kg m}^{-3}$ ,  $65 \text{ kW m}^{-2}$ . Figure 4.8 shows the comparison between measured and predicted  $R_f$  values, with experimental  $R_f$  increasing sharply at the beginning of the experiment until staying almost constant at  $R_f = 0.6 \text{ K m}^2 \text{ kW}^{-1}$ . The model correctly predicts that the boiling regime is reached earlier compared to SOC, but fails to replicate the fast experimental behavior at the initial phase. This may be due to external influences on experimental  $R_f$  as described in Section 4.3.6.

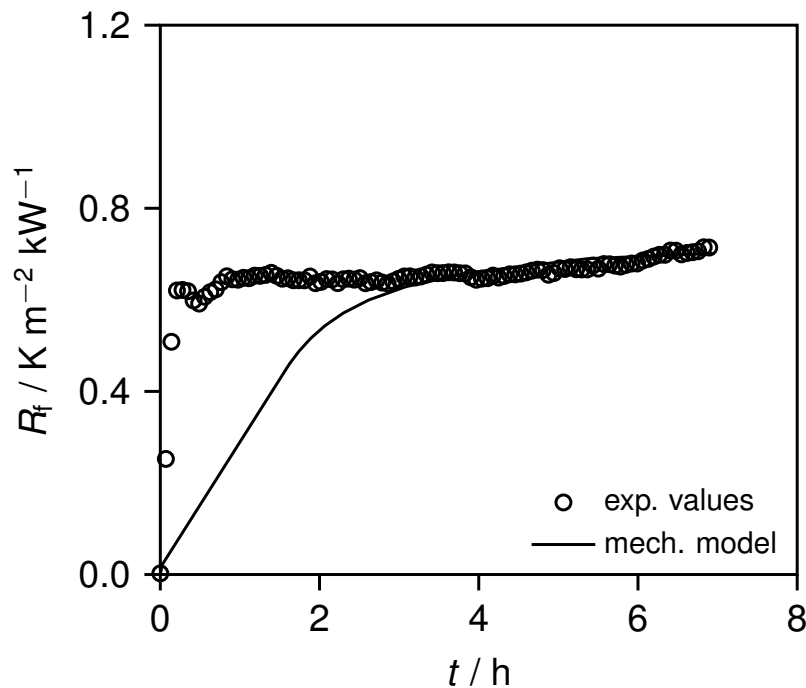


**Figure 4.8.:** Comparison of experimental and model  $R_f$  for operating conditions of  $2 \text{ kg m}^{-3}$ ,  $65 \text{ kW m}^{-2}$ .

A complete list of the estimated parameters for all operating conditions can be found in Table C.4.

Figure 4.9 shows the optimized and regressed parameter values for both models over the WPC concentration and heat flux. The black points in Figure 4.9 are the parameters, that were obtained through optimization of measured data. Results show that the mechanistic model parameter  $p_2$  (s. Fig 4.9B) increases almost exclusively with increasing heat flux and shows no dependency of WPC concentration for  $55$  and  $65 \text{ kW m}^{-2}$ . Since the deposition increases with higher heat flux, increased surface temperatures must be reached to allow for enough

deposition, regardless of whey concentration. This means that the surface temperature cannot drop too far once the boiling regime is reached resulting in higher  $p_2$ . The only exception of this is at low  $\dot{q} = 45 \text{ kW}/(\text{m}^2)$  where a higher  $p_2$  value was recorded for  $c_{\text{wpc}}$  of  $2 \text{ kg m}^{-3}$  compared to 4 and  $6 \text{ kg m}^{-3}$ . A more diverse result is obtained for  $p_1$  where the highest value was recorded for high WPC concentrations and low heat flux and the lowest value at low WPC concentrations and high heat flux. This behavior might be due the low impact of  $p_2$  at lower heat flux, as the boiling regime is reached late in the experiments and  $p_2$  has no effect on the solution before the regime change. At higher heat flux,  $p_2$  has a stronger impact on the solution, which means that the range of  $p_1$  can be lower. This also indicates that  $p_2$  has a stronger influence on the results than  $p_1$ . Subfigures 4.9C and D show that heat flux and WPC concentration also influence parameters  $A$  and  $B$  of the empirical model. Parameter  $A$  exhibits an increase with both elevated heat flux and concentration, with similar rates of change observed between these two factors. In contrast, Parameter  $B$  remains relatively stable across most variations in heat flux and concentration, with the exception of a heat flux of  $45 \text{ kW m}^{-2}$  at a concentration of  $6 \text{ kg m}^{-3}$ , where it reaches significantly higher values than under other operating conditions.

Symbolic regression was performed for both models, where  $p$  (mechanistic model) or  $A$  and  $B$  parameters (empirical model) were regressed to the training data. The resulting equations are listed in Table 4.6 for both models. Figure 4.9 shows the estimated parameter values using the obtained regression functions for all operating conditions as a surface plot. Interestingly, in the mechanistic model the  $p_2$  prediction equation is only dependent on heat flux but not on whey protein concentration and  $p_1$  is also mostly dependent on  $\dot{q}$ , while the empirical model parameter show more diverse behavior. All equations feature different terms and therefore behave differently in regard to the operating conditions. This is also visualized in Figure 4.9, where the surfaces represent the symbolic regression functions as a function of operating conditions. Results show that the functions closely match the optimized behavior, especially for  $p_1$  and  $A$ .

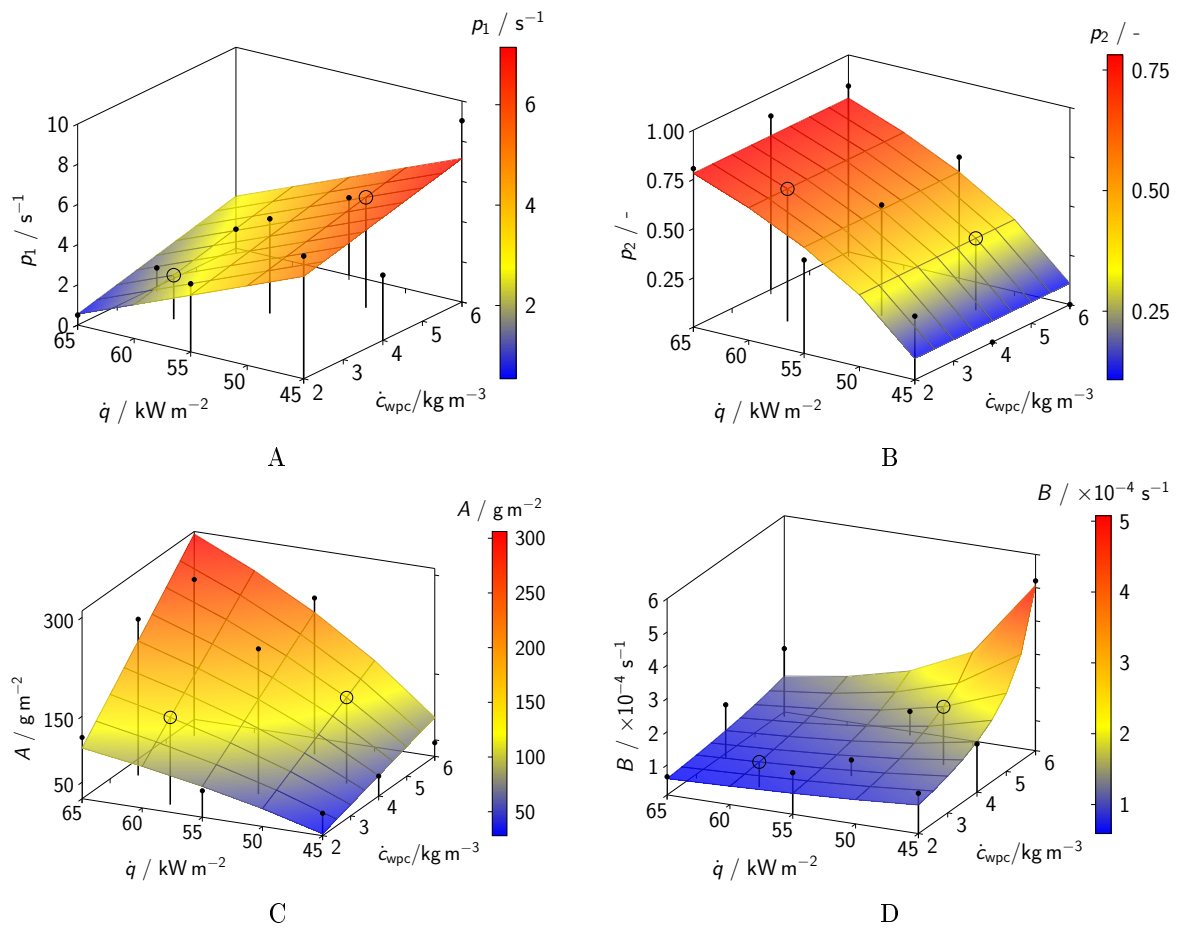


**Figure 4.9.:** Impact of process conditions (heat flux and concentration of protein) on estimated model parameters, Top row: model parameters  $p_1$  and,  $p_2$  of the empirical model. Bottom row: parameters A and B of the mechanistic model. Symbols: (●) – training data used for the symbolic regression, (○) – validation data. Surface plot: predictions using the functions obtained by symbolic regression (s. Tab. 4.6).

**Table 4.5.:** Measured and predicted values of  $m_f$

No.	$m_{f,meas.}$ $\text{g m}^{-2}$	$\hat{m}_{f,emp}$ $\text{g m}^{-2}$	$\hat{m}_{f,mech}$ $\text{g m}^{-2}$
38	177.0	184.871	112.221
39	94.5	114.030	161.853
40	548.0	4327.950	1251.986

**Table 4.6.:** Regression equations, where  $x_1 = c_{\text{WPC}}$  in  $\text{kg m}^{-3}$  and  $x_2 = \dot{q}$  in  $\text{W m}^{-2}$ .

Parameter	Equation
$p_1$	$-2.278 \times 10^{-4} x_2 + x_1 + 14.324$
$p_2$	$\left( \frac{-98206.370}{x_2} + 2.241 \right)^{0.785}$
$A$	$x_1 (-1.057 \times 10^7 x_2^{-1} + 262.264)$
$B$	$3.072 \left( x_2 - \left( \frac{x_1}{7.887 \times 10^{-5}} \right) \right)^{-1}$

The regression functions allow to predict the fouling mass  $\hat{m}_f$  for previously unseen validation points (s. Tab. 4.3). Results for both models are shown in Figure 4.10. When comparing predicted and measured fouling mass for the mechanistic model deviations of up to 71% were found for operating conditions inside the boundaries of the trained dataset (experiment 38 and 39). This may result from the inaccuracies in estimating  $p_2$  (s. Fig 4.9B), where larger deviations occur compared to  $p_1$  regression (s. Fig 4.9A). Unsurprisingly, an even higher deviation of 128 % was recorded when extrapolating outside the training set for experiment 40 (s. Tab. 4.5).

The empirical model delivers more reasonable  $\hat{m}_{f,\text{emp}}$  (s. Fig. 4.10) for operating conditions within the boundary of the training set, with deviations within the  $\pm 20\%$  that were obtained from the training dataset. However, when trying to extrapolate data in the last validation point (experiment 40), a mass of  $\hat{m}_{f,\text{emp}} = 4327 \text{ g m}^{-2}$  is predicted, resulting in an error of almost 700%. This outlier results from the predicted  $B = 3.5 \times 10^{-2}$ , which is roughly 2 orders of magnitude larger compared to the values obtained from the training data. This means that further data is required to generalize the obtained symbolic functions outside the boundaries of the training data. This is especially true for the empirical model, which lags the underlying physical connections, resulting in a poorer prediction quality compared to the mechanistic model.

When comparing  $R_f$  values between mechanistic model and experimental data, similar deviations can be seen to those already observed for the training dataset (s. Fig. 4.11). For the first validation point, the model calculates a lower growth rate compared to the experimental results. However, the values converge with the transition to evaporation, so that a good agreement could be achieved for this area. For the second validation point, no satisfactory agreement between model and experiment can be determined. This is mainly due to the unusually low experimental data, which may have been caused by external disturbances, such as a lack of bubble formation. For the third validation point, the data again show a predominantly good agreement. It is noteworthy that the model predicts a higher growth rate than was measured in the experiment. The experimental data also show increased thermal resistance at the beginning and end. At the beginning of the experiment, this is due to a delay in the removal of the fouling layer. At the end of the experiment, the sporadic collapse of the evaporation layer may be due to the strong growth, resulting in an increase in the thermal

resistance coefficient. This could indicate the limitations of the boiling model described above.

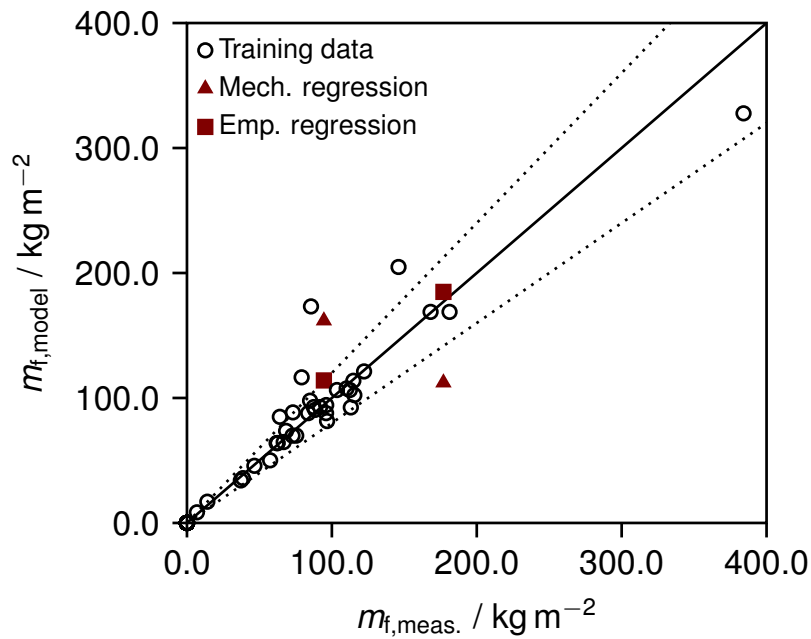


**Figure 4.10.:** Comparison of predicted training and validation data with experimental results.

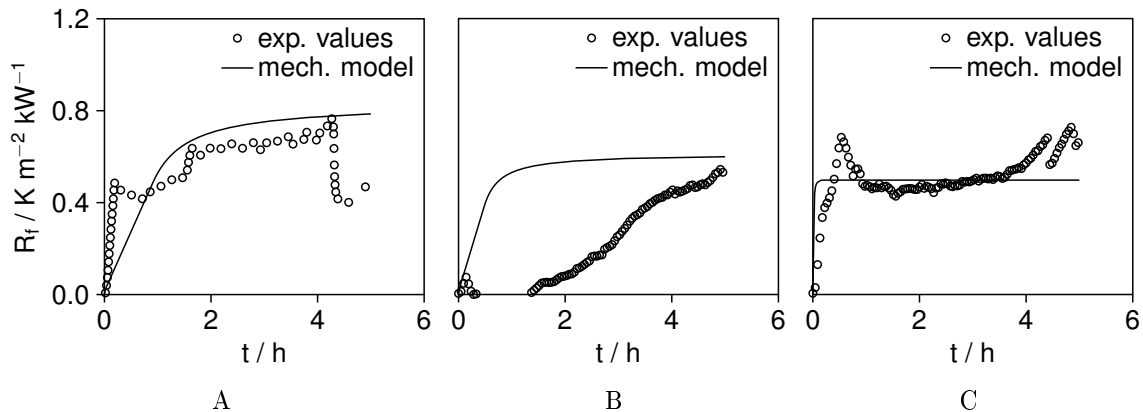


**Figure 4.11.:** Comparison of the experimental data and the model prediction of the fouling heat resistance as a function of time for the three different validation points: 1 (A), 2 (B) and 3 (C).

## 4.5. Conclusions

In this study, a mechanistic model for predicting the fouling behavior of WPC on PEEK heat exchangers was developed and compared to a simple empirical model based on experimental data. The mechanistic model incorporated modifications of existing heat exchanger models to account for the unique fouling characteristic of layer detachment due to boiling under the fouling layer. Optimization of model parameters allowed for good agreement with experimental fouling mass for both models. The mechanistic model is able to predict the fouling resistance

$R_f$ , but its accuracy was inconsistent across various operating conditions. Symbolic regressions were performed on the optimization parameters of both models and the predictive quality of the regressions was validated using values not seen during model training. While regression of the optimization parameters for the mechanistic model was not satisfactory, the empirical model regression was found to be as accurate as model results of previously optimized data points. However, for operating conditions outside the training data boundaries, the empirical model failed to predict fouling mass accurately, while the mechanistic model performed somewhat better. Both models showed room for improvement, which indicates that further experimental data is necessary to be able to generalize beyond the training set. For the mechanistic model strong assumptions had to be made in order to model the observed behavior. Future studies should aim to understand the boiling phenomena in detail, which might help to increase the predicting accuracy. Overall, both models show promise for optimizing heat exchanger design in dairy processing, reducing the need for extensive experiments and mitigating fouling-related downtime.

## 5. Conclusion and Outlook

This thesis is focused on utilizing PEEK-based heat exchangers to mitigate fouling, which can severely impair the operation of chemical or food processing plants when using common heat exchanger materials like stainless steel. The main challenges are increasing the operating time of heat exchangers, reducing the equipment cleaning times and to predict when and how much fouling will occur for untested operating conditions.

In Chapter 2 the fouling behavior of PEEK heat exchangers in  $\text{CaSO}_4$  solutions was investigated and compared to stainless steel. A comparison between two experimental setups of different size allowed investigating the scalability of results. Cleaning times were examined by rising with deionized water. Key findings highlight that the amount of deposit is correlated with material roughness and inversely correlated with surface shear force, which can be increased through higher bulk fluid velocities. This has resulted in significantly reduced fouling of pure PEEK material compared to stainless steel, as well as reduced cleaning time for PEEK compared to stainless steel. However it also meant a larger amount of fouling on TKT material, which has a higher roughness than stainless steel and pure PEEK.

In Chapter 3 the same materials were used to investigate the fouling behavior of WPC solutions. Again, it was shown that the use of PEEK materials resulted in lower heat resistance due to fouling compared to SS. The reason for this is that boiling occurred underneath the fouling layer, which partially detaches from the PEEK and limits the fouling induced heat resistance. PEEK materials were also shown to clean faster than SS and to allow cleaning in process.

These findings were used in Chapter 4 to predict the deposition behavior of WPC by developing a mechanistic model. The models results were compared to an empirical model. Both models were able to predict the results well, but major deviations between the experimental data and the model predictions were found when the behavior outside available data had to be determined.

Despite the successes achieved in this thesis, three limitations restrict the use of PEEK in heat exchangers

- For  $\text{CaSO}_4$ , the limited scalability of the results poses significant challenges in extrapolating the system's behavior to larger scales, such as industrial applications.
- The mechanism of WPC fouling could not be related to surface properties of the materials, which makes it difficult to optimize fouling mitigation.
- The mechanistic model failed to accurately predict the fouling behavior outside the tested range, indicating that the strong assumptions underlying the model are likely responsible for the observed deviations.

However, the findings of this thesis provide valuable insights into the fouling process, which is crucial for the design and optimization of PEEK heat exchangers. For this purpose, experiments successfully demonstrated the fouling mitigation potential of PEEK materials compared to traditional stainless steel, while modeling the fouling behavior provided valuable insights into its mechanism.

# Nomenclature

## Latin Letters

$A$	Heat transfer area	$\text{m}^2$
$A_{\text{cr}}$	Cross-sectional area of the heat exchanger	$\text{m}^2$
$A_x$	Surface area of heat exchanger element	$\text{m}^2$
$A_s$	Surface area	$\text{m}^2$
$B$	Fit parameter for logarithmic fouling model	
$C$	Circumference	$\text{m}$
$C_A$	Concentration of aggregated BLG	$\text{mol m}^{-3}$
$C_A^*$	Concentration of aggregated BLG in thermal boundary layer	$\text{mol m}^{-3}$
$C_N$	Concentration of native BLG	$\text{mol m}^{-3}$
$C_U$	Concentration of unfolded BLG	$\text{mol m}^{-3}$
$C_N^*$	Concentration of native BLG in thermal boundary layer	$\text{mol m}^{-3}$
$C_U^*$	Concentration of unfolded BLG in thermal boundary layer	$\text{mol m}^{-3}$
$D$	Diffusion coefficient of BLG in water	$\text{m}^2 \text{s}^{-1}$
$D_A$	Molecular diameter of aggregated BLG	$\text{m}$
$D_N$	Molecular diameter of native BLG	$\text{m}$
$D_U$	Molecular diameter of unfolded BLG	$\text{m}$
$d$	Diameter	$\text{m}$
$d_f$	Fouling layer thickness	$\text{m}$
$\dot{d}_f$	Fouling thickness growth rate	$\text{m s}^{-1}$
$d_h$	Hydraulic diameter	$\text{m}$
$d_m$	Material thickness	$\text{m}$
$d_b$	Copper block thickness	$\text{m}$
$d_p$	Thickness of PEEK material	$\text{m}$
$E_N$	Activation energy for the denaturation reaction	$\text{J mol}^{-1}$
$E_U$	Activation energy for the unfolding reaction	$\text{J mol}^{-1}$
$h_{\text{gap}}$	Height of channel	$\text{m}$
$I$	Current	$\text{A}$
$k_1$	Proportional constant	-
$K$	Proportional constant	-
$k_{N,0}$	Pre-exponential factor for the denaturation reaction	$\text{s}^{-1}$
$k_{U,0}$	Pre-exponential factor for the unfolding reaction	$\text{m}^3 \text{kg}^{-1} \text{s}^{-1}$

$L$	Length of heat exchanger	m
$L_w$	Width of heat exchanger	m
$m$	Mass	kg
$\dot{m}_d$	Deposition rate	$\text{kg m}^{-2} \text{s}^{-1}$
$\dot{m}_r$	Removal rate	$\text{kg m}^{-2} \text{s}^{-1}$
$\dot{m}_D$	Local deposition mass flow rate	$\text{kg m}^{-2} \text{s}^{-1}$
$m_f$	Deposit mass	$\text{kg m}^{-2}$
$\hat{m}_f$	Predicted deposit mass	$\text{kg m}^{-2}$
$\dot{Q}$	Heat flow	kW
$\dot{Q}_{\text{const}}$	Constant heat flow	kW
$\dot{q}$	Heat flux	$\text{kW m}^{-2}$
$\dot{q}_{\text{const}}$	Constant heat flux	$\text{kW m}^{-2}$
$R$	Ideal gas constant	$\text{J mol}^{-1} \text{K}^{-1}$
$R_f$	Thermal fouling resistance	$\text{m}^2 \text{K kW}^{-1}$
$S$	Stickability	-
$S_a$	Average surface roughness	$\mu\text{m}$
$S_a$	Arithmetic average height	$\mu\text{m}$
$S_q$	Mean square root height	$\mu\text{m}$
$T_{\text{boil}}$	Boiling temperature	K
$T_w$	Wall temperature	K
$T_{\text{bulk}}$	Bulk fluid temperature	K
$T_{\text{cond}}$	Temperature through conduction during boiling	K
$t$	Time	s
$U$	Overall heat transfer coefficient	$\text{kW}/(\text{m}^2\text{K})$
$U_0$	Overall heat transfer coefficient in the clean state	$\text{W}/(\text{m}^2\text{K})$
$U_t$	Overall heat transfer coefficient at time $t$	$\text{W}/(\text{m}^2\text{K})$
$V$	Voltage	$\text{kg m}^2 \text{s}^{-3} \text{A}$
$\dot{V}$	Volumetric flow rate	$\text{m}^3 \text{s}^{-1}$
$v$	Velocity	$\text{m s}^{-1}$
$x$	Position along the heat exchanger length	m

## Greek Letters

$\alpha$	Convective heat transfer coefficient	$\text{W}/(\text{m}^2\text{K})$
$\alpha_0$	Heat transfer coefficient in the clean state	$\text{W}/(\text{m}^2\text{K})$
$\delta$	Boundary layer thickness	m
$\eta$	Dynamic viscosity	Pa s
$\lambda$	Heat conductivity coefficient	$\text{W}/(\text{mK})$
$\lambda_f$	Thermal conductivity of fouling layer	$\text{W m}^{-1} \text{K}$
$\lambda_P$	Thermal conductivity of PEEK material	$\text{W m}^{-1} \text{K}$
$\nu$	Kinematic viscosity	$\text{m}^2 \text{s}^{-1}$
$\rho_f$	Density of fouling layer	$\text{kg}/\text{m}^3$

## Subscripts

0	Quantity related to the initial condition
A	Quantity related to aggregated BLG species
boil	Quantity at boiling condition
const	Constant
cr	Cross-section
D	Quantity related to depositing BLG species
emp	Quantity resulting from the empirical model
exp	Quantity resulting from an experiment
f	Fouling
fl	Flow / fluid
gap	Height of channel
h	Hydraulic
HX	Quantity related to heat exchanger geometry
I	Quantity at the liquid interface
i	Index of species or grid point
in	Inlet-related quantity
max	Upper bound or maximum value
mech	Quantity resulting from the mechanistic model
min	Lower bound or minimum value
MT	Mass transfer
N	Quantity related to native BLG species
P	Quantity related PEEK material
t	Thermal boundary layer
U	Quantity related to unfolded BLG species
w	Wall
w	Width

## Abbreviations

BLG	$\beta$ -lactoglobulin
FDA	US Food and Drug Administration
HX	Heat exchanger
MSE	Mean squared error
NRMSE	Normalized root mean square error
ODE	Ordinary differential equation
PDE	Partial differential equation
PEEK	Polyether ether ketone
PMMA	Polymethylmethacrylate
PVDF	Polyvinylidene fluoride
Re	Reynolds number
Sc	Schmidt number
Sh	Sherwood number
SS	Stainless steel
TKT	Talcum added PEEK
WPC	Whey protein concentrate



## References

- [1] B. Bansal and X. D. Chen, “A critical review of milk fouling in heat exchangers,” *Comprehensive Reviews In Food Science And Food Safety*, 2006. DOI: 10.1111/j.1541-4337.2006.tb00080.x.
- [2] H. Müller-Steinhagen, M. R. Malayeri, and A. P. Watkinson, “Heat exchanger fouling: Environmental impacts,” *Heat Transfer Engineering*, vol. 30, no. 10-11, 2009. DOI: 10.1080/01457630902744119.
- [3] T. R. Bott, *Fouling of Heat Exchangers* (Chemical engineering monographs). Amsterdam and New York: Elsevier, 1995, vol. vol. 26, ISBN: 0444821864.
- [4] Q. Zhao, Y. Liu, C. Wang, S. Wang, and H. Müller-Steinhagen, “Effect of surface free energy on the adhesion of biofouling and crystalline fouling,” *Chemical Engineering Science*, vol. 60, no. 17, pp. 4858–4865, 2005. DOI: 10.1016/j.ces.2005.04.006.
- [5] S. N. Kazi, G. G. Duffy, and X. D. Chen, “Fouling and fouling mitigation on heated metal surfaces,” *Desalination*, vol. 288, 2012. DOI: 10.1016/j.desal.2011.12.022.
- [6] J. Berce, M. Zupančič, M. Može, and I. Golobič, “A review of crystallization fouling in heat exchangers,” *Processes*, vol. 9, no. 8, p. 1356, 2021. DOI: 10.3390/pr9081356.
- [7] H. Müller-Steinhagen, M. R. Malayeri, and A. P. Watkinson, “Heat exchanger fouling: Mitigation and cleaning strategies,” *Heat Transfer Engineering*, vol. 32, no. 3-4, pp. 189–196, 2011. DOI: 10.1080/01457632.2010.503108.
- [8] H.-J. Bart and S. Scholl, Eds., *Innovative Heat Exchangers*. Springer International Publishing, 2018, ISBN: 978-3-319-71639-8.
- [9] H. Kiepfer, W. Omar, T. Schröder, and H.-J. Bart, “Polymer film heat transfer surfaces in seawater desalination: Fouling layer formation and technology,” *Chemical Engineering & Technology*, vol. 43, no. 6, pp. 1205–1213, 2020. DOI: 10.1002/ceat.201900492.
- [10] A. Ataki, H. Kiepfer, and H.-J. Bart, “Investigations on crystallization fouling on peek films used as heat transfer surfaces: Experimental results,” *Heat and Mass Transfer*, vol. 56, no. 5, pp. 1443–1452, 2020. DOI: 10.1007/s00231-019-02769-w.
- [11] C. Dreiser and H.-J. Bart, “Mineral scale control in polymer film heat exchangers,” *Applied Thermal Engineering*, vol. 65, no. 1-2, pp. 524–529, 2014. DOI: 10.1016/j.applthermaleng.2014.01.018.
- [12] X. Huang, P. Jiang, and T. Tanaka, “A review of dielectric polymer composites with high thermal conductivity,” *IEEE Electrical Insulation Magazine*, vol. 27, no. 4, pp. 8–16, 2011. DOI: 10.1109/MEI.2011.5954064.
- [13] Verein Deutscher Ingenieure, *VDI Heat Atlas*. Berlin, Heidelberg: Springer Berlin Heidelberg, 2013, ISBN: 978-3-642-19980-6. DOI: 10.1007/978-3-642-19981-3.

- [14] M. W. Bohnet, “Crystallization fouling on heat transfer surfaces - 25 years of research in braunschweig,” in *Proceedings of 6th International Conference on Heat Exchanger Fouling and Cleaning - Challenges and Opportunities*, H. Müller-Steinhagen, M. R. Malaryi, and A. P. Watkinson, Eds., Irsee: Heat Transfer Engineering, 2005.
- [15] C. Dreiser, L. J. Krätz, and H.-J. Bart, “Kinetics and quantity of crystallization fouling on polymer surfaces: Impact of surface characteristics and process conditions,” *Heat Transfer Engineering*, no. 7-8, pp. 715–720, 2015. DOI: 10.1080/01457632.2015.954954.
- [16] H. U. Zettler, M. Wei, Q. Zhao, and H. Müller-Steinhagen, “Influence of surface properties and characteristics on fouling in plate heat exchangers,” *Heat Transfer Engineering*, vol. 26, no. 2, pp. 3–17, 2005. DOI: 10.1080/01457630590897024.
- [17] C. Meyer, P.-L. Pelz, K. Jasch, H.-J. Bart, E. von Harbou, and S. Scholl, “A screening apparatus for comparing the fouling resistance of heat exchanger surfaces,” *Chemie Ingenieur Technik*, 2024. DOI: 10.1002/cite.202300210.
- [18] A. Helalizadeh, H. Müller-Steinhagen, and M. Jamialahmadi, “Mathematical modelling of mixed salt precipitation during convective heat transfer and sub-cooled flow boiling,” *Chemical Engineering Science*, vol. 60, no. 18, pp. 5078–5088, 2005. DOI: 10.1016/j.ces.2005.03.040.
- [19] F. Fahiminia, A. P. Watkinson, and N. Epstein, “Early events in the precipitation fouling of calcium sulphate dihydrate under sensible heating conditions,” *The Canadian Journal of Chemical Engineering*, vol. 85, no. 5, pp. 679–691, 2007. DOI: 10.1002/cjce.5450850515.
- [20] E. Lee, J. Jeon, H. Kang, and Y. Kim, “Thermal resistance in corrugated plate heat exchangers under crystallization fouling of calcium sulfate (CaSO<sub>4</sub>),” *International Journal of Heat and Mass Transfer*, vol. 78, pp. 908–916, 2014. DOI: 10.1016/j.ijheatmasstransfer.2014.07.069.
- [21] S. H. Najibi, H. Müller-Steinhagen, and M. Jamialahmadi, “Calcium sulphate scale formation during subcooled flow boiling,” *Chemical Engineering Science*, vol. 52, no. 8, pp. 1265–1284, 1997. DOI: 10.1016/S0009-2509(96)00505-2.
- [22] M. G. Mwaba, M. R. Golriz, and J. Gu, “A semi-empirical correlation for crystallization fouling on heat exchange surfaces,” *Applied Thermal Engineering*, vol. 26, no. 4, pp. 440–447, 2006. DOI: 10.1016/j.applthermaleng.2005.05.021.
- [23] David Hasson/Joseph Zahavi, “Mechanism of calcium sulfate scale deposition on heat transfer surfaces,” *Industrial & Engineering Chemistry Fundamentals*, vol. 1970, no. 9 (1), 1970. DOI: 10.1021/i160033a001.
- [24] S. Schilling, H. Glade, and T. Orth, “Investigation of crystallization fouling on novel polymer composite heat exchanger tubes,” *Heat Transfer Engineering*, vol. 43, no. 15-16, pp. 1326–1336, 2022. DOI: 10.1080/01457632.2021.1963533.

- [25] D. Yang, J. Liu, X. E, and L. Jiang, “Model for seawater fouling and effects of temperature, flow velocity and surface free energy on seawater fouling,” *Chinese Journal of Chemical Engineering*, vol. 24, no. 5, pp. 658–664, 2016. DOI: 10.1016/j.cjche.2016.01.012.
- [26] D. Q. Kern and R. E. Seaton, “A theoretical analysis of thermal surface fouling,” *British Chemical Engineering*, 1959.
- [27] M. M. Awad, “Influence of surface temperature on surface fouling - theoretical approach,” *Life Science Journal*, no. 9 (3), pp. 1733–1741, 2012. DOI: 10.7537/marsljsj090312.252.
- [28] A. Herz, M. R. Malayeri, and H. Müller-Steinhagen, “Fouling of roughened stainless steel surfaces during convective heat transfer to aqueous solutions,” *Energy Conversion and Management*, vol. 49, no. 11, pp. 3381–3386, 2008. DOI: 10.1016/j.enconman.2007.09.034.
- [29] S. N. Kazi, G. G. Duffy, and X. D. Chen, “Mineral scale formation and mitigation on metals and a polymeric heat exchanger surface,” *Applied Thermal Engineering*, vol. 30, no. 14-15, 2010. DOI: 10.1016/j.applthermaleng.2010.06.005.
- [30] D. J. Gunn, “Effect of surface roughness on the nucleation and growth of calcium sulfate metal surfaces,” *Journal of Crystal Growth*, no. 50, 1980. DOI: 10.1016/0022-0248(80)90104-9.
- [31] G. P. Demopoulos, “Aqueous precipitation and crystallization for the production of particulate solids with desired properties,” *Hydrometallurgy*, vol. 96, no. 3, pp. 199–214, 2009. DOI: 10.1016/j.hydromet.2008.10.004.
- [32] OECD/FAO, *OECD-FAO Agricultural Outlook 2023-2032*. OECD, 2023. DOI: 10.1787/08801ab7-en.
- [33] A. Sharma and S. Macchietto, “Fouling and cleaning of plate heat exchangers: Dairy application,” *Food and Bioproducts Processing*, vol. 126, pp. 32–41, 2021. DOI: 10.1016/j.fbp.2020.12.005.
- [34] M. Indumathy, S. Sobana, and R. C. Panda, “Modelling of fouling in a plate heat exchanger with high temperature pasteurisation process,” *Applied Thermal Engineering*, vol. 189, p. 116674, 2021. DOI: 10.1016/j.applthermaleng.2021.116674.
- [35] C. Spiegel, M. Kraut, G. Rabsch, C. Küsters, W. Augustin, and S. Scholl, “Fouling detection in an optically accessible microstructured heat exchanger,” *Chemical Engineering & Technology*, vol. 42, no. 10, 2019. DOI: 10.1002/ceat.201900161.
- [36] M. Saget, C. F. de Almeida, V. Fierro, A. Celzard, G. Delaplace, V. Thomy, Y. Coffinier, and M. Jimenez, “A critical review on surface modifications mitigating dairy fouling,” *Comprehensive Reviews In Food Science And Food Safety*, vol. 20, no. 5, 2021. DOI: 10.1111/1541-4337.12794.
- [37] C. Bär, M. Sutter, C. Kopp, P. Neuhaus, R. Portmann, L. Egger, B. Reidy, and W. Bisig, “Impact of herbage proportion, animal breed, lactation stage and season on the fatty acid and protein composition of milk,” *International Dairy Journal*, vol. 109, p. 104785, 2020. DOI: 10.1016/j.idairyj.2020.104785.

- [38] E. Hayes, D. Wallace, C. O'Donnell, D. Greene, D. Hennessy, N. O'Shea, J. T. Tobin, and M. A. Fenelon, "Trend analysis and prediction of seasonal changes in milk composition from a pasture-based dairy research herd," *Journal of Dairy Science*, vol. 106, no. 4, pp. 2326–2337, 2023. DOI: 10.3168/jds.2021-21483.
- [39] M. Timlin, J. T. Tobin, A. Brodkorb, E. G. Murphy, P. Dillon, D. Hennessy, M. O'Donovan, K. M. Pierce, and T. F. O'Callaghan, "The impact of seasonality in pasture-based production systems on milk composition and functionality," *Foods (Basel, Switzerland)*, vol. 10, no. 3, 2021. DOI: 10.3390/foods10030607.
- [40] C. Boxler, *Fouling by milk constituents and cleaning of modified surfaces*. Technische Universität Braunschweig, Göttingen: Cuvillier Verlag, 2015, ISBN: 9783736990289.
- [41] T. Huppertz and H. Nieuwenhuijse, "Constituent fouling during heat treatment of milk: A review," *International Dairy Journal*, vol. 126, 2022. DOI: 10.1016/j.idairyj.2021.105236.
- [42] M. Zhu, F. L. Santamaria, and S. Macchietto, "A general dynamic model of a complete milk pasteuriser unit subject to fouling," in *30th European Symposium on Computer Aided Process Engineering*, ser. Computer Aided Chemical Engineering, vol. 48, Elsevier, 2020, pp. 247–252, ISBN: 9780128233771. DOI: 10.1016/B978-0-12-823377-1.50042-2.
- [43] A. E. Guerrero-Navarro, A. G. Ríos-Castillo, C. Ripolles-Avila, X. Felipe, and J. J. Rodríguez-Jerez, "Microscopic analysis and microstructural characterization of the organic and inorganic components of dairy fouling during the cleaning process," *Journal of Dairy Science*, vol. 103, no. 3, pp. 2117–2127, 2020. DOI: 10.3168/jds.2019-16957.
- [44] S. Prakash, N. Datta, and H. C. Deeth, "Methods of detecting fouling caused by heating of milk," *Food Reviews International*, vol. 21, no. 3, pp. 267–293, 2005. DOI: 10.1080/FRI-200061609.
- [45] E. Sadeghinezhad, S. N. Kazi, M. Dahari, M. R. Safaei, R. Sadri, and A. Badarudin, "A comprehensive review of milk fouling on heated surfaces," *Critical Reviews in Food Science and Nutrition*, vol. 55, no. 12, pp. 1724–1743, 2015. DOI: 10.1080/10408398.2012.752343.
- [46] S. Pohl, M. Madzgalla, W. Manz, and H. J. Bart, "Biofouling on polymeric heat exchanger surfaces with e. coli and native biofilms," *Biofouling*, vol. 31, no. 9-10, 2015. DOI: 10.1080/08927014.2015.1094691.
- [47] L. H. Beierer, M. Glyde, R. E. Day, and G. L. Hosgood, "Biomechanical comparison of a locking compression plate combined with an intramedullary pin or a polyetheretherketone rod in a cadaveric canine tibia gap model," *Veterinary Surgery : VS*, vol. 43, no. 8, 2014. DOI: 10.1111/j.1532-950X.2014.12254.x.
- [48] M. Mauermann, U. Eschenhagen, T. Bley, and J.-P. Majschak, "Surface modifications – application potential for the reduction of cleaning costs in the food processing industry," *Trends in Food Science & Technology*, vol. 20, 2009. DOI: 10.1016/j.tifs.2009.01.020.
- [49] Bayerische Milchindustrie eG, *Analysenzertifikat Bayolan P80*, 2023.

- [50] M. Khaldi, P. Blanpain-Avet, R. Guérin, G. Ronse, L. Bouvier, C. André, S. Bornaz, T. Croguennec, R. Jeantet, and G. Delaplace, “Effect of calcium content and flow regime on whey protein fouling and cleaning in a plate heat exchanger,” *Journal of Food Engineering*, vol. 147, 2015. DOI: 10.1016/j.jfoodeng.2014.09.020.
- [51] W. Liu, X. D. Chen, R. Jeantet, C. André, S. Bellayer, and G. Delaplace, “Effect of casein/whey ratio on the thermal denaturation of whey proteins and subsequent fouling in a plate heat exchanger,” *Journal of Food Engineering*, vol. 289, 2021. DOI: 10.1016/j.jfoodeng.2020.110175.
- [52] A. Fickak, E. Hatfield, and X. Chen, “Influence of run time and aging on fouling and cleaning of whey protein deposits on heat exchanger surface,” *Journal of Food Research*, 2012. DOI: 10.5539/jfr.v1n1p212.
- [53] C. R. Gillham, P. J. Fryer, A. Hasting, and D. I. Wilson, “Cleaning-in-place of whey protein fouling deposits,” *Food and Bioproducts Processing*, vol. 77, no. 2, 1999. DOI: 10.1205/096030899532420.
- [54] L. Schnöing, R. N. Shahnazari, I. Hohlen, A. J. van Asselt, W. Augustin, and S. Scholl, “Alkaline cleaning of ultra-high temperature dairy fouling in a laminar flow regime,” *International Dairy Journal*, vol. 117, 2021. DOI: 10.1016/j.idairyj.2021.105014.
- [55] T. R. Tuladhar, W. R. Paterson, and D. I. Wilson, “Investigation of alkaline cleaning-in-place of whey protein deposits using dynamic gauging,” *Food and Bioproducts Processing*, vol. 80, no. 3, 2002. DOI: 10.1205/096030802760309223.
- [56] R. L. J. Lyster, “The denaturation of  $\alpha$ -lactalbumin and  $\alpha$ -lactoglobulin in heated milk,” *Journal of Dairy Research*, vol. 37, no. 2, 1970. DOI: 10.1017/S0022029900013297.
- [57] S. M. Gotham, P. J. Fryer, and A. M. Pritchard, “ $\alpha$ -lactoglobulin denaturation and aggregation reactions and fouling deposit formation: A dsc study,” *International Journal of Food Science & Technology*, vol. 27, no. 3, 1992. DOI: 10.1111/j.1365-2621.1992.tb02033.x.
- [58] S. Jun and V. M. Puri, “Fouling models for heat exchangers in dairy processing: A review,” *Journal of Food Engineering*, no. 28, 2005. DOI: 10.1111/j.1745-4530.2005.00473.x.
- [59] S. P. Roefs and K. G. de Kruif, “A model for the denaturation and aggregation of beta-lactoglobulin,” *European Journal of Biochemistry*, vol. 226, no. 3, pp. 883–889, 1994. DOI: 10.1111/j.1432-1033.1994.00883.x.
- [60] S. G. Anema and A. B. McKenna, “Reaction kinetics of thermal denaturation of whey proteins in heated reconstituted whole milk,” *Journal of Agricultural and Food Chemistry*, vol. 44, no. 2, pp. 422–428, 1996. DOI: 10.1021/jf950217q.
- [61] Z. Qin, S. K. Balasubramanian, W. F. Wolkers, J. A. Pearce, and J. C. Bischof, “Correlated parameter fit of arrhenius model for thermal denaturation of proteins and cells,” *Annals of Biomedical Engineering*, vol. 42, no. 12, pp. 2392–2404, 2014. DOI: 10.1007/s10439-014-1100-y.

- [62] A. Barbiroli, S. Iametti, and F. Bonomi, "Beta-lactoglobulin as a model food protein: How to promote, prevent, and exploit its unfolding processes," *Molecules (Basel, Switzerland)*, vol. 27, no. 3, 2022. DOI: 10.3390/molecules27031131.
- [63] P. de Jong, *Modelling and optimization of thermal processes in the dairy industry: PhD Thesis*. 1996, ISBN: 90-9009034-7.
- [64] A. Tolkach and U. Kulozik, "Reaction kinetic pathway of reversible and irreversible thermal denaturation of  $\alpha$ -lactoglobulin," *Le Lait*, vol. 87, no. 4-5, pp. 301–315, 2007. DOI: 10.1051/lait:2007012.
- [65] S. Alhuthali, G. Delaplace, S. Macchietto, and L. Bouvier, "Whey protein fouling prediction in plate heat exchanger by combining dynamic modelling, dimensional analysis, and symbolic regression," *Food and Bioprocesses Processing*, vol. 134, pp. 163–180, 2022. DOI: 10.1016/j.fbp.2022.05.009.
- [66] M. C. Georgiadis, G. E. Rotstein, and S. Macchietto, "Optimal design and operation of heat exchangers under milk fouling," *AIChE Journal*, vol. 44, no. 9, 1998. DOI: 10.1002/aic.690440917.
- [67] W. Choi, S. Jun, L. T. Nguyen, N. Rungraeng, H. Yi, S. Balasubramanian, V. M. Puri, and J. Lee, "3-d milk fouling modeling of plate heat exchangers with different surface finishes using computational fluid dynamics codes," *Journal of Food Process Engineering*, vol. 36, no. 4, pp. 439–449, 2013. DOI: 10.1111/j.1745-4530.2012.00684.x.
- [68] S. Jun and V. M. Puri, "A 2d dynamic model for fouling performance of plate heat exchangers," *Journal of Food Engineering*, vol. 75, no. 3, pp. 364–374, 2006. DOI: 10.1016/j.jfoodeng.2005.03.064.
- [69] M. C. Georgiadis and S. Macchietto, "Dynamic modelling and simulation of plate heat exchangers under milk fouling," *Chemical Engineering Science*, no. 55, 2000. DOI: 10.1016/S0009-2509(99)00429-7.
- [70] F. Ceglia, A. Macaluso, E. Marrasso, M. Sasso, and L. Vanoli, "Modelling of polymeric shell and tube heat exchangers for low-medium temperature geothermal applications," *Energies*, vol. 13, no. 11, p. 2737, 2020. DOI: 10.3390/en13112737.
- [71] F. Pan, X. D. Chen, R. Mercadé-Prieto, and J. Xiao, "Numerical simulation of milk fouling: Taking fouling layer domain and localized surface reaction kinetics into account," *Chemical Engineering Science*, vol. 197, pp. 306–316, 2019. DOI: 10.1016/j.ces.2018.12.021.
- [72] B. Sengupta, N. Das, and P. Sen, "Monomerization and aggregation of  $\beta$ -lactoglobulin under adverse condition: A fluorescence correlation spectroscopic investigation," *Biochimica et Biophysica Acta. Proteins and Proteomics*, vol. 1866, no. 2, pp. 316–326, 2018. DOI: 10.1016/j.bbapap.2017.11.007.
- [73] T. Jeurnink, P. Walstra, and C. G. de Kruif, "Mechanisms of fouling in dairy processing," *Dairy Processing. Neth. Milk & Dairy Journal*, 1996.

- 
- [74] T. Skoglund, “Minimising bubble-related fouling: How to improve performance at lower cost and increased product quality—a theoretical proposal for ultra-high-temperature processing of milk,” *International Journal of Dairy Technology*, vol. 77, no. 2, pp. 594–603, 2024. DOI: 10.1111/1471-0307.13037.
- [75] H. A. E. Bennett, *Aspects Of Fouling In Dairy Processing*. Palmerston North, 2007.
- [76] J. Bezanson, A. Edelman, S. Karpinski, and V. B. Shah, “Julia: A fresh approach to numerical computing,” *SIAM Review*, vol. 59, no. 1, pp. 65–98, 2017. DOI: 10.1137/141000671.
- [77] L. Allen, A. O’Connell, and V. Kiermer, “How can we ensure visibility and diversity in research contributions? how the contributor role taxonomy (credit) is helping the shift from authorship to contributorship,” *Learned Publishing*, vol. 32, no. 1, pp. 71–74, 2019. DOI: 10.1002/leap.1210.



# A. Supplementary Information for Chapter 2

Velocity and streamline profiles were generated for various Reynolds numbers using Ansys Fluent. The velocity profiles were generated by visualizing values on a plane section across the channel, while the stream line profiles encompass the whole fluid domain.

## A.1. Velocity Profiles

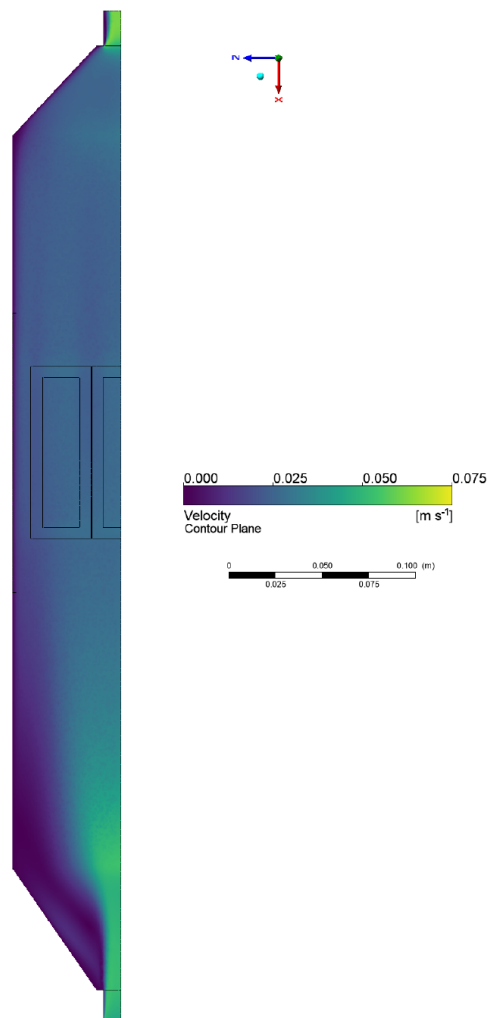
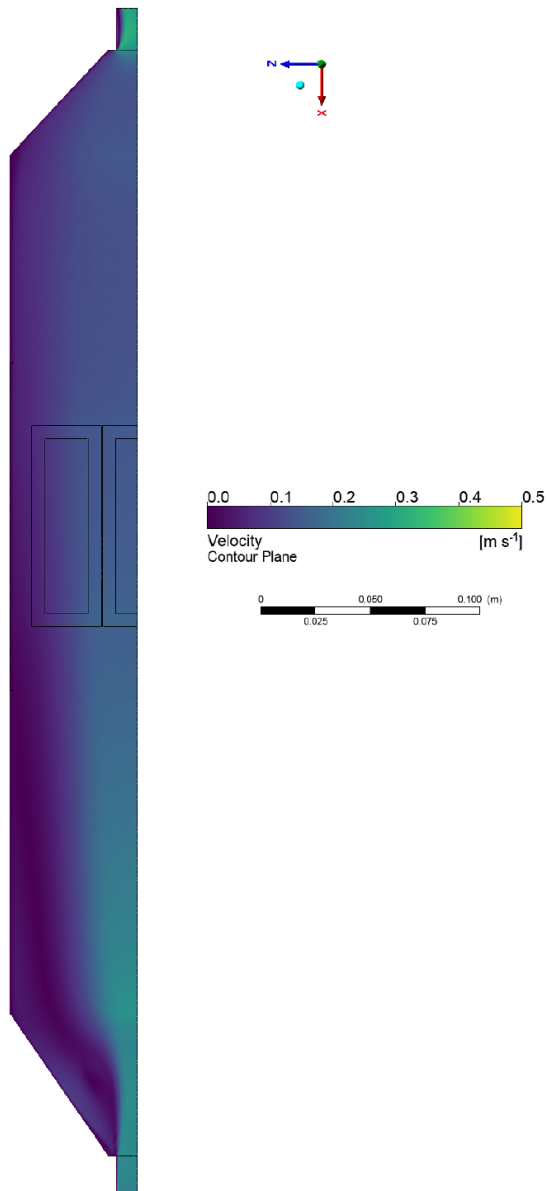
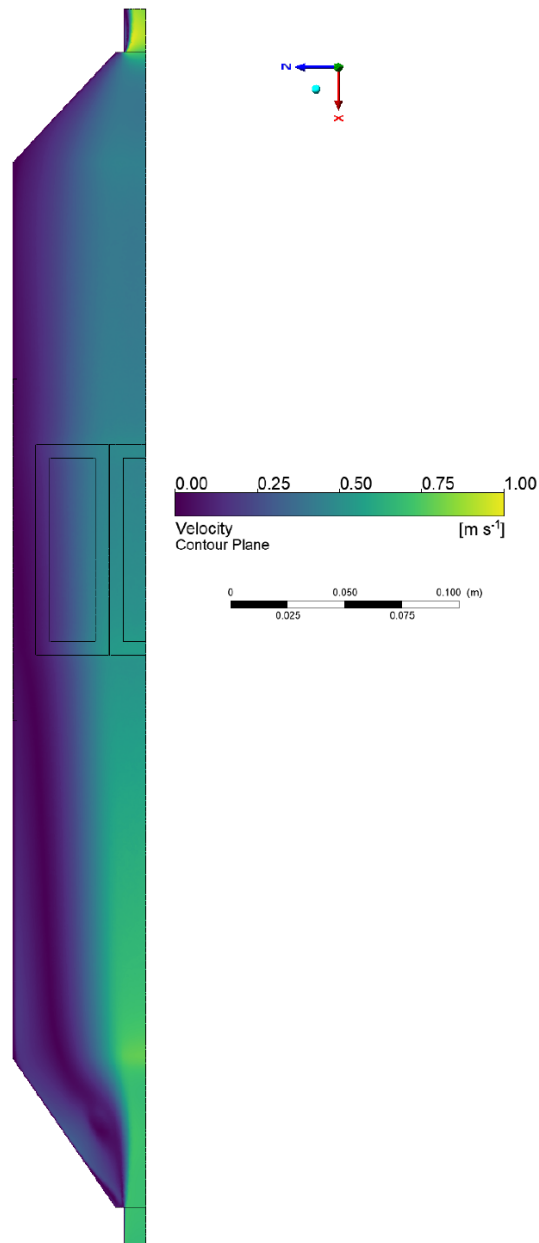


Figure A.1.: Velocity profile across channel width at  $Re = 200$ .



**Figure A.2.:** Velocity profile across channel width at  $Re = 1000$ .



**Figure A.3.:** Velocity profile across channel width at  $Re = 3000$ .

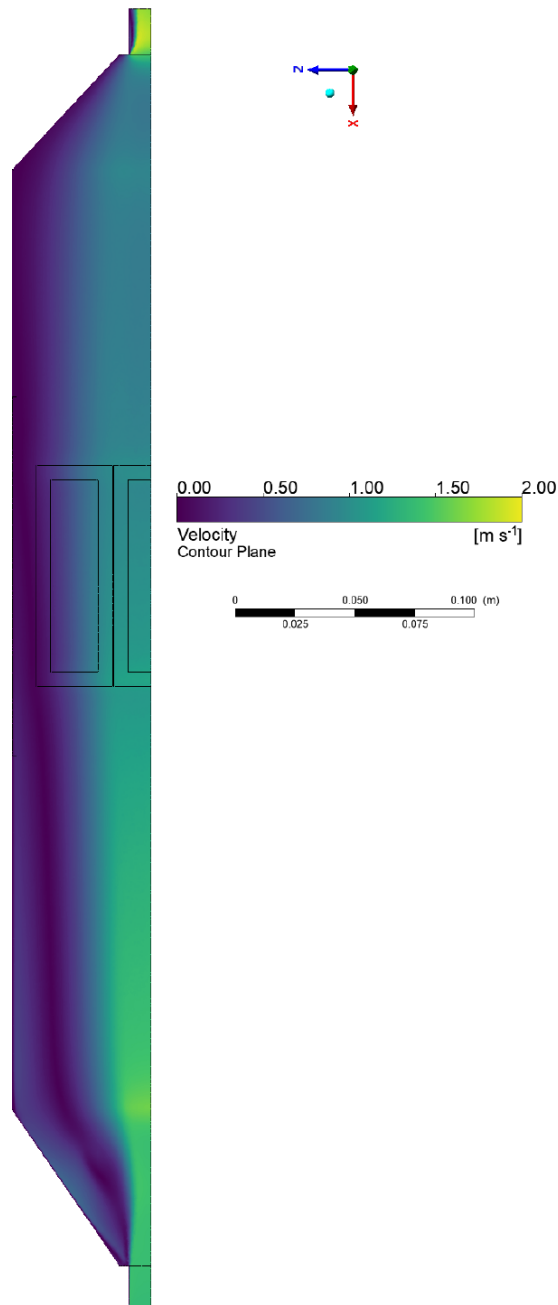


**Figure A.4.:** Velocity profile across channel width at  $Re = 6000$ .

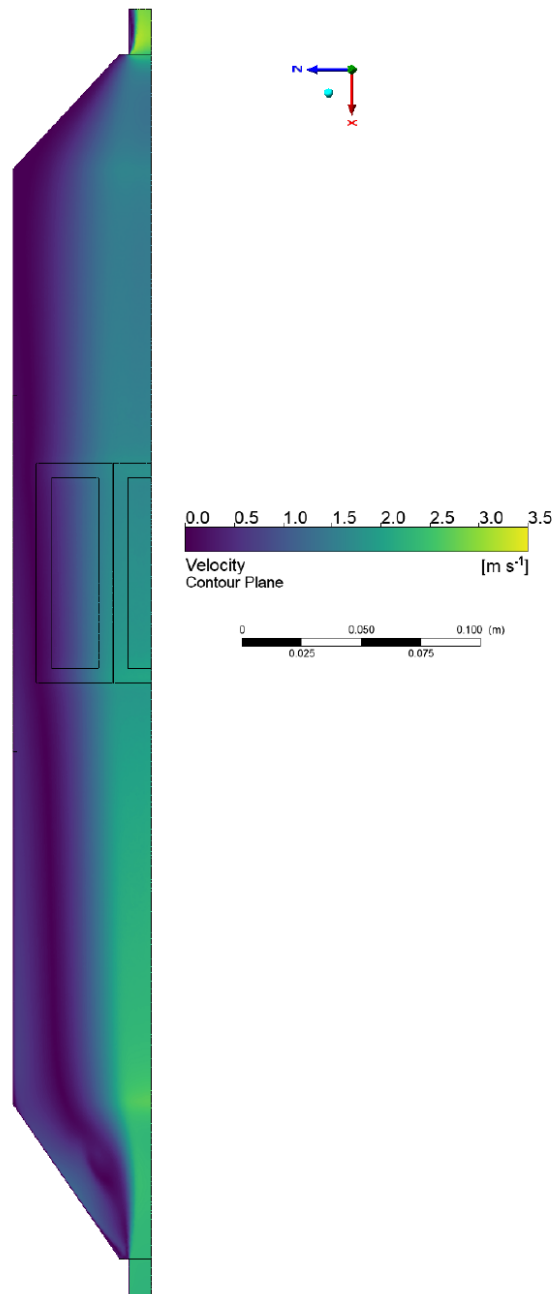


**Figure A.5.:** Velocity profile across channel width at  $\text{Re} = 10000$ .

## A.2. Streamlines

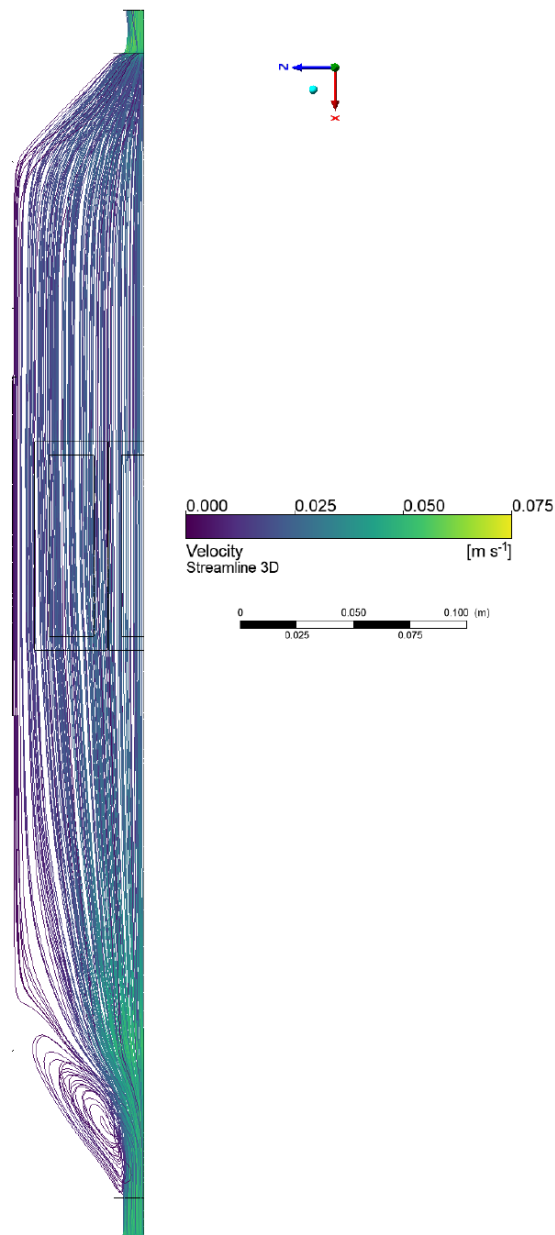
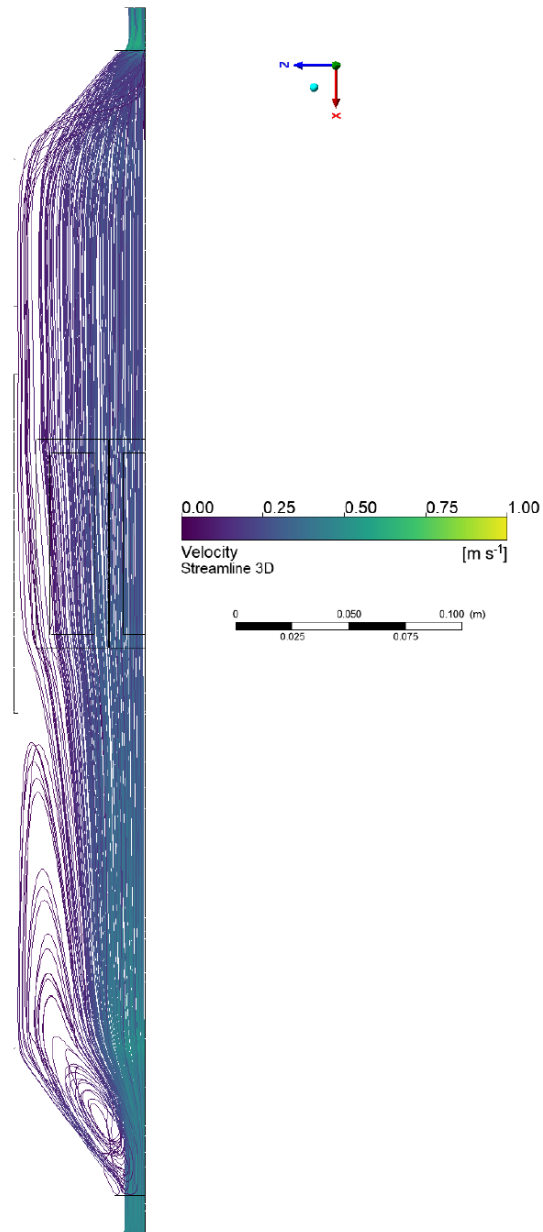
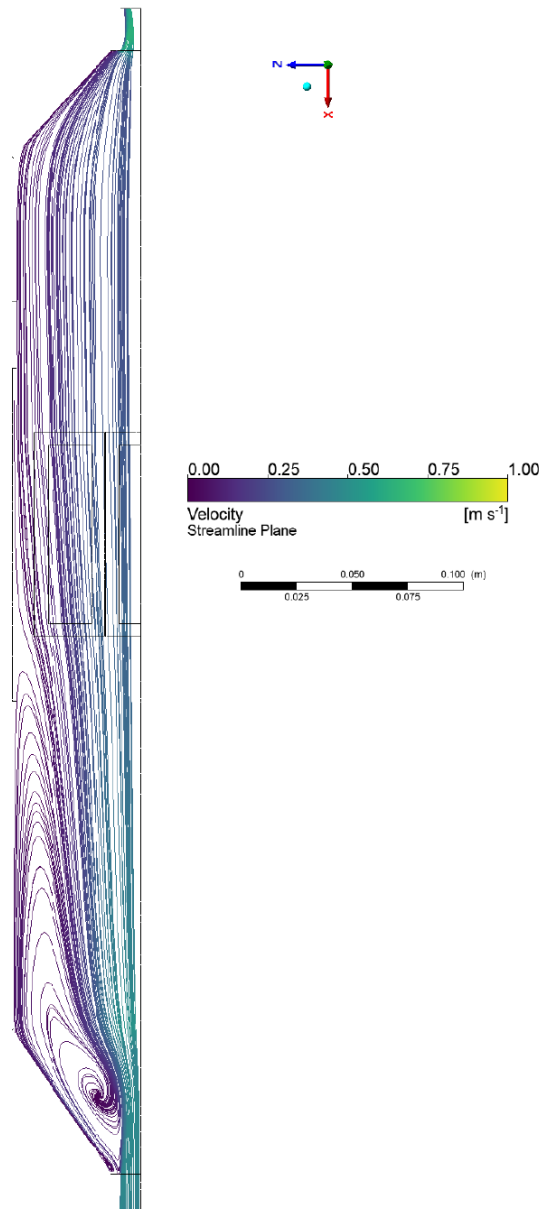


Figure A.6.: Velocity profile across channel width at  $Re = 200$ .



**Figure A.7.:** Streamline profile across channel width at  $Re = 1000$ .



**Figure A.8.:** Streamline profile across channel width at  $Re = 2000$ .

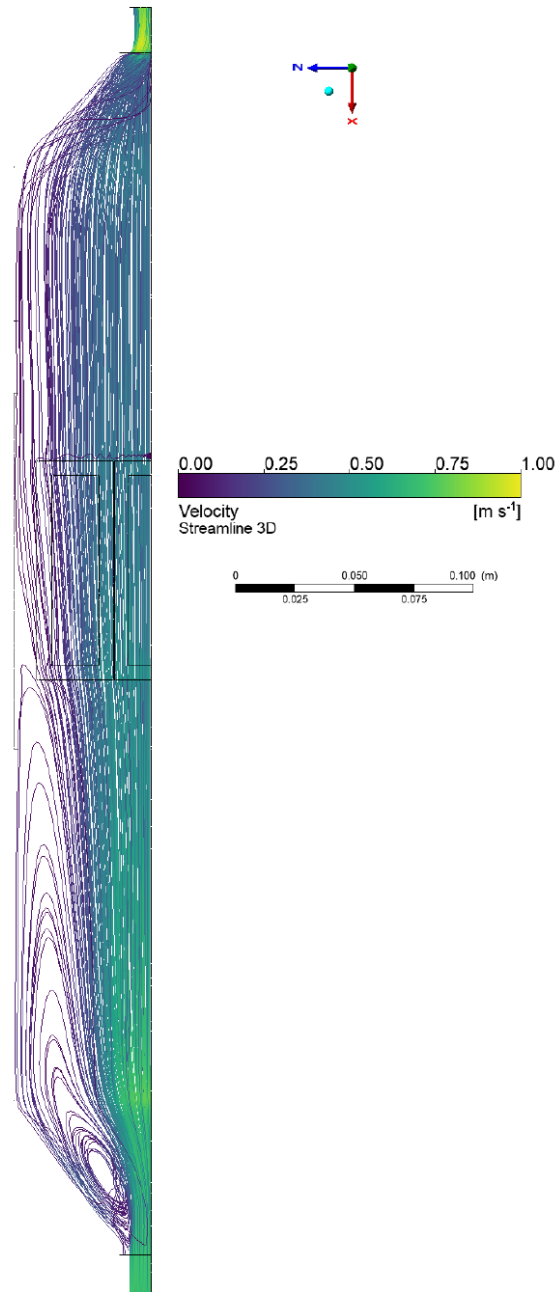


**Figure A.9.:** Streamline profile across channel width at  $Re = 3000$ .

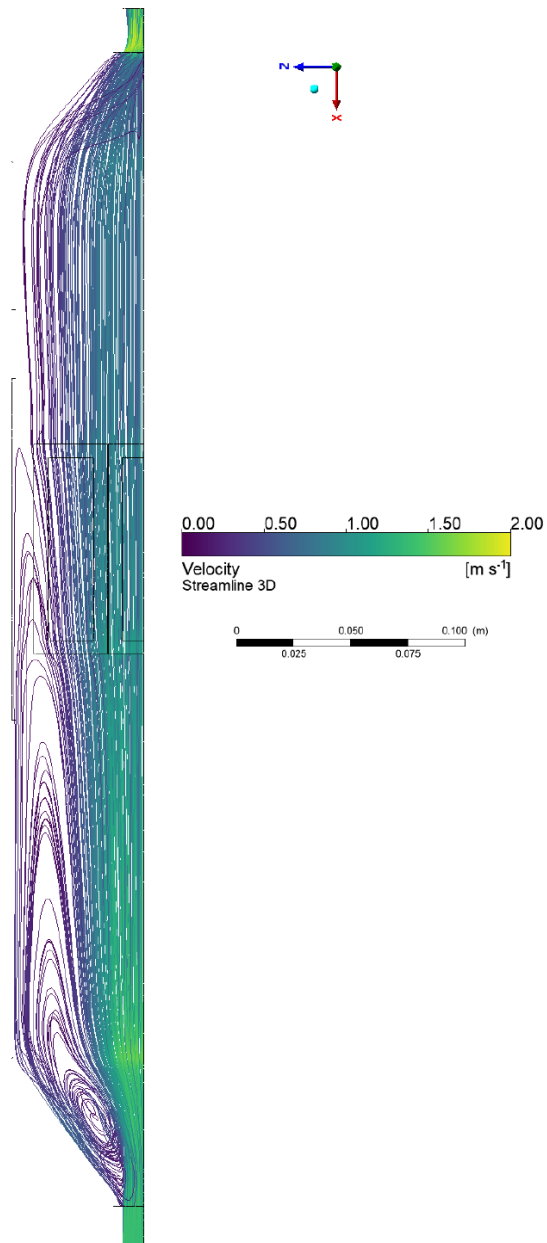


**Figure A.10.:** Streamline profile across channel width at  $\text{Re} = 6000$ .

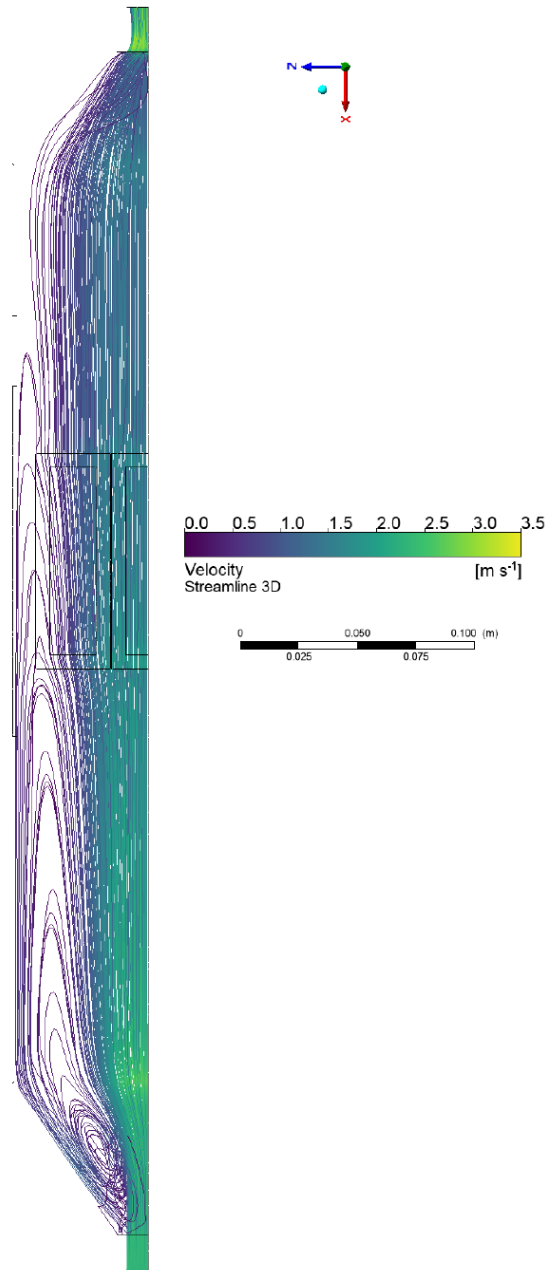


**Figure A.11.:** Streamline profile across channel width at  $Re = 10000$ .

### A.3. Mesh independence study

**Table A.1.:** Parameters of the mesh independence study in terms of element sizes at different locations for the screening channel.

Mesh	Element size	Element size on roundings	Element size on edges
Mesh_2	$2.73 \cdot 10^{-2}$	$2.00 \cdot 10^{-3}$	$2.50 \cdot 10^{-3}$
Mesh_1	$2.73 \cdot 10^{-2}$	$2.00 \cdot 10^{-3}$	$2.50 \cdot 10^{-3}$
Mesh_3	$2.50 \cdot 10^{-3}$	$2.00 \cdot 10^{-3}$	$2.50 \cdot 10^{-3}$
Mesh_4	$2.50 \cdot 10^{-3}$	$2.00 \cdot 10^{-3}$	$2.50 \cdot 10^{-3}$
Mesh_5	$2.50 \cdot 10^{-3}$	$1.00 \cdot 10^{-3}$	$1.00 \cdot 10^{-3}$
Mesh_6	$2.50 \cdot 10^{-3}$	$1.00 \cdot 10^{-3}$	$1.00 \cdot 10^{-3}$
Mesh_8	$9.00 \cdot 10^{-4}$	$9.00 \cdot 10^{-4}$	$9.00 \cdot 10^{-4}$
Mesh_9	$8.00 \cdot 10^{-4}$	$8.00 \cdot 10^{-4}$	$8.00 \cdot 10^{-4}$
Mesh_10	$7.00 \cdot 10^{-4}$	$7.00 \cdot 10^{-4}$	$7.00 \cdot 10^{-4}$
Mesh_11_2	$7.00 \cdot 10^{-4}$	$7.00 \cdot 10^{-4}$	$7.00 \cdot 10^{-4}$
Mesh_11	$7.00 \cdot 10^{-4}$	$7.00 \cdot 10^{-4}$	$7.00 \cdot 10^{-4}$
Mesh_12	$7.00 \cdot 10^{-4}$	$7.00 \cdot 10^{-4}$	$7.00 \cdot 10^{-4}$
Mesh_12_2	$7.00 \cdot 10^{-4}$	$7.00 \cdot 10^{-4}$	$7.00 \cdot 10^{-4}$
Mesh_13	$6.50 \cdot 10^{-4}$	$6.50 \cdot 10^{-4}$	$6.50 \cdot 10^{-4}$
Mesh_14	$6.20 \cdot 10^{-4}$	$6.20 \cdot 10^{-4}$	$6.20 \cdot 10^{-4}$
Mesh_15	$6.10 \cdot 10^{-4}$	$6.10 \cdot 10^{-4}$	$6.10 \cdot 10^{-4}$
Mesh_16	$6.10 \cdot 10^{-4}$	$6.10 \cdot 10^{-4}$	$6.10 \cdot 10^{-4}$
Mesh_17	$6.10 \cdot 10^{-4}$	$6.10 \cdot 10^{-4}$	$6.10 \cdot 10^{-4}$

### A.4. Experimental CFD validation using PIV Laser

The PIV system consisting of laser, camera and processing software has been purchased from LaVision GmbH (Göttingen, Germany) and is schematically depicted in Figure A.12. It utilizes a EverGreen Big Sky YAG-Laser (EVG00200), which was manufactured by Quantal Laser (Lannion, France). The laser's beam has a wavelength of 532 nm at a frequency of 15 Hz. The energy of the light was measured to be 200 mJ. The laser contains two light sources, A and B, with the intensity constrained to 45%.

A scientific Complementary Metal–Oxide–Semiconductor (sCMOS) camera with a  $f = -20$  mm lens and an opening angle of  $12^\circ$  captures the reflected laser light. The records two images at an interval of  $15 \mu\text{s}$  between shots. An image taken by the sCMOS camera is shown in Figure A.13, where the area for postprocessing has been marked in purple. Figure A.14 shows a picture of the seed particles reflecting laser light onto the camera. Results for Reynolds numbers of 200, 1000 and 2000 are shown in Figures A.15, A.16 and A.17 respectively.

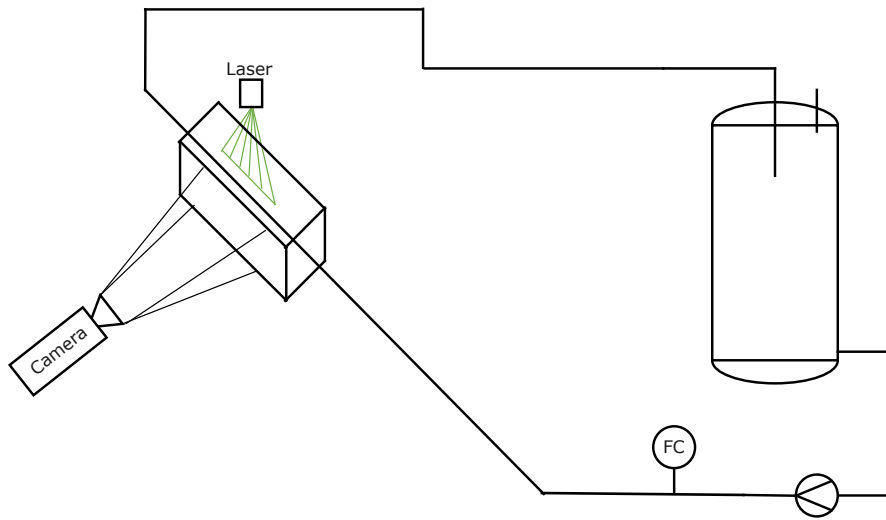


**Figure A.12.:** Schematic representation of the PIV setup.

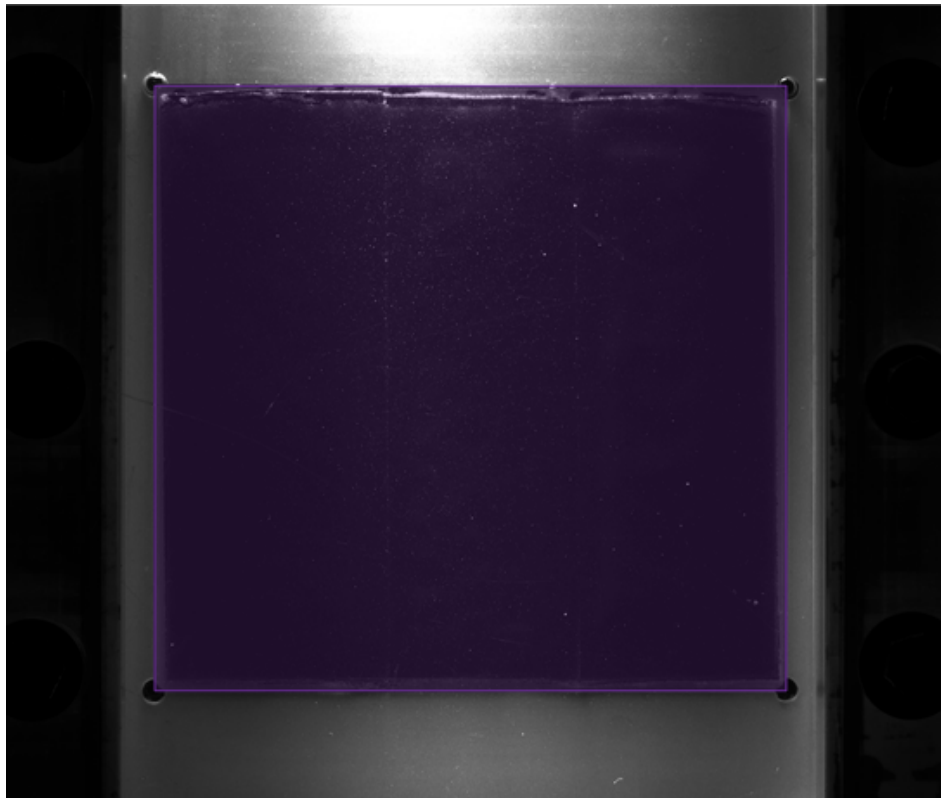


**Figure A.13.:** Example of PIV camera foto without seed particles, where the purple square indicates the area that is selected for postprocessing.

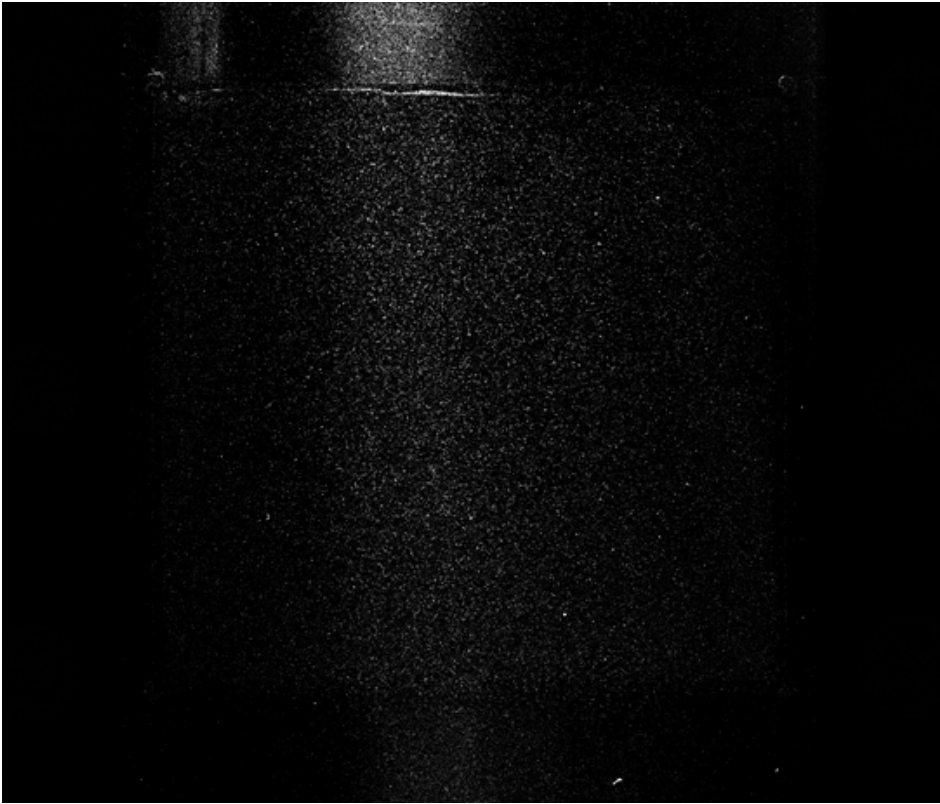


**Figure A.14.:** Image of laser light reflected from seed particles at  $Re = 2000$ .

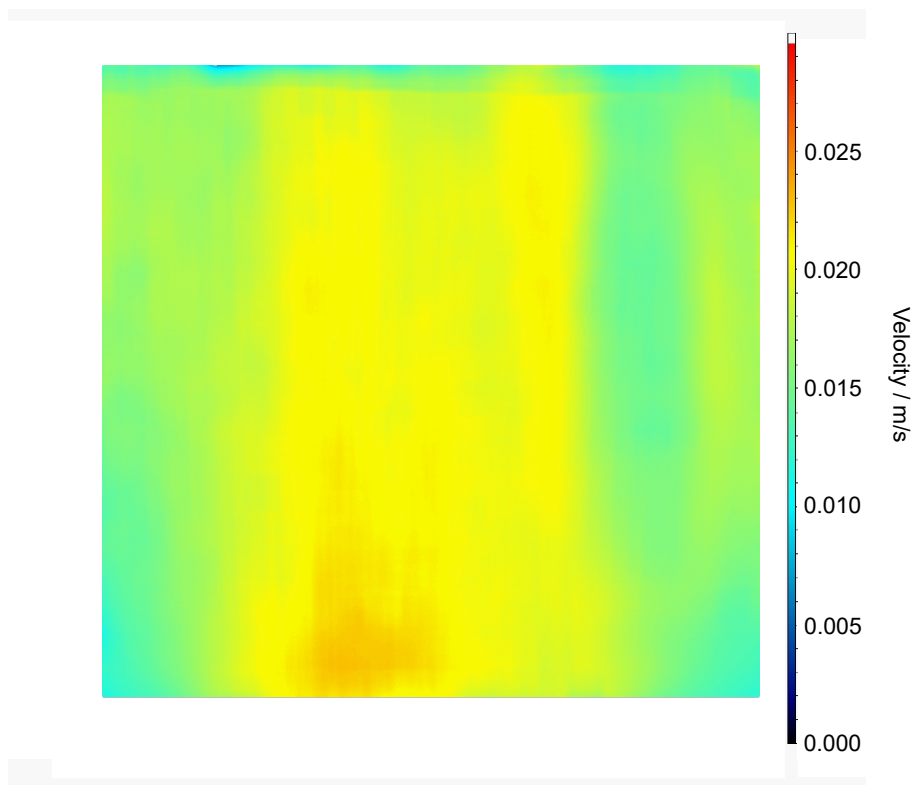


**Figure A.15.:** Post processed image of the velocity profile for  $Re = 200$ .

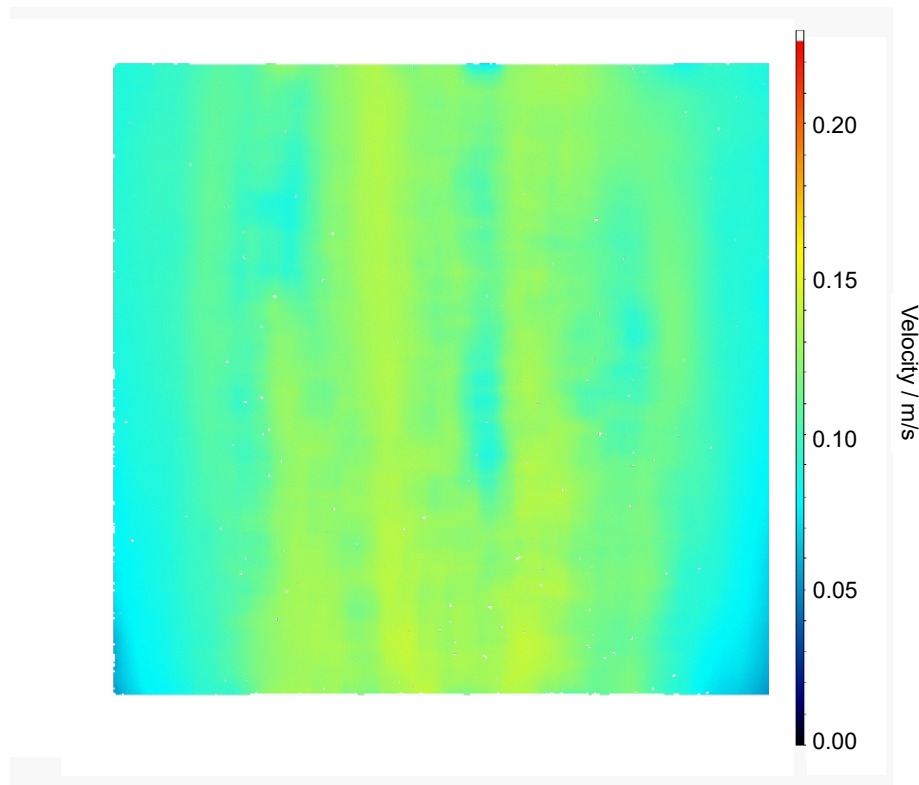


Figure A.16.: Post processed image of the velocity profile for  $Re = 1000$ .

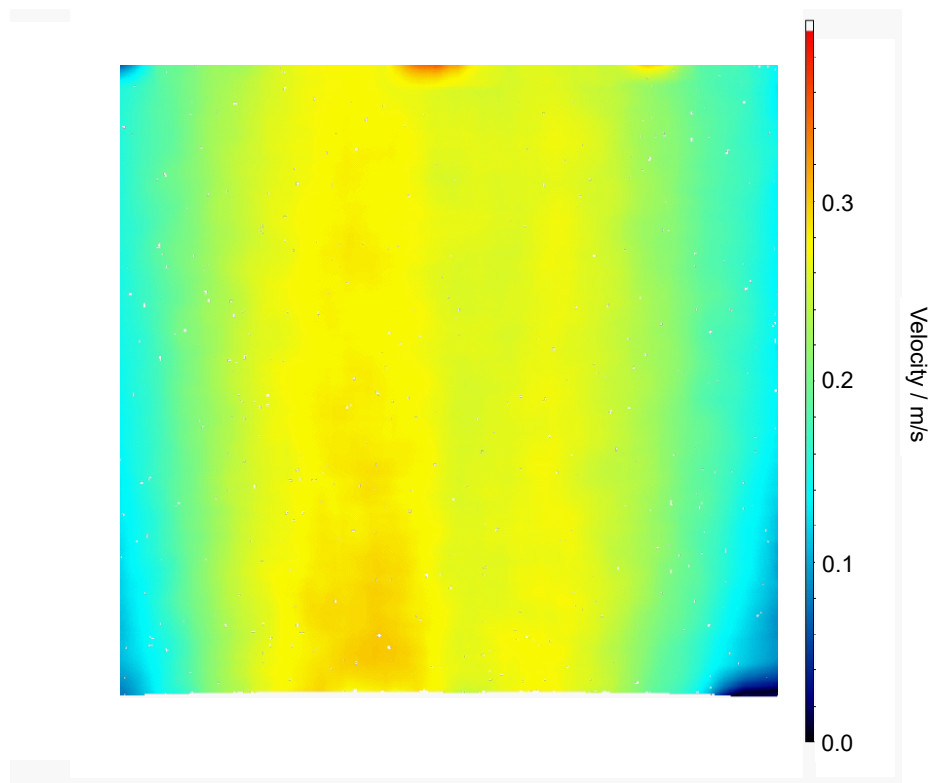
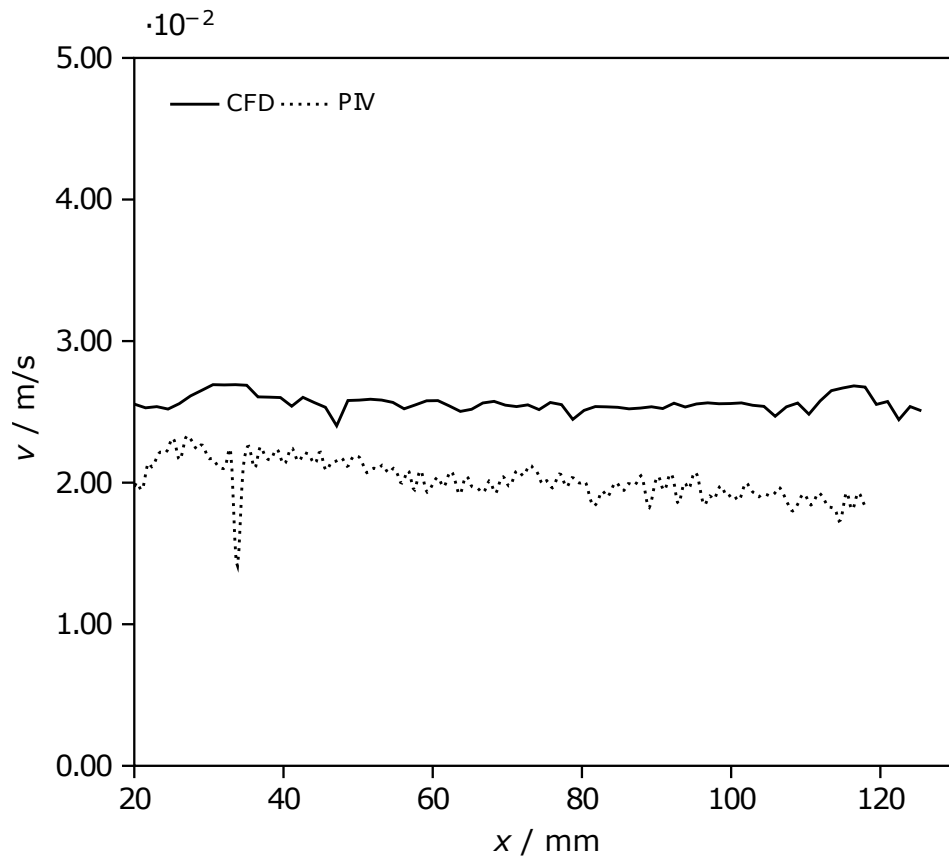
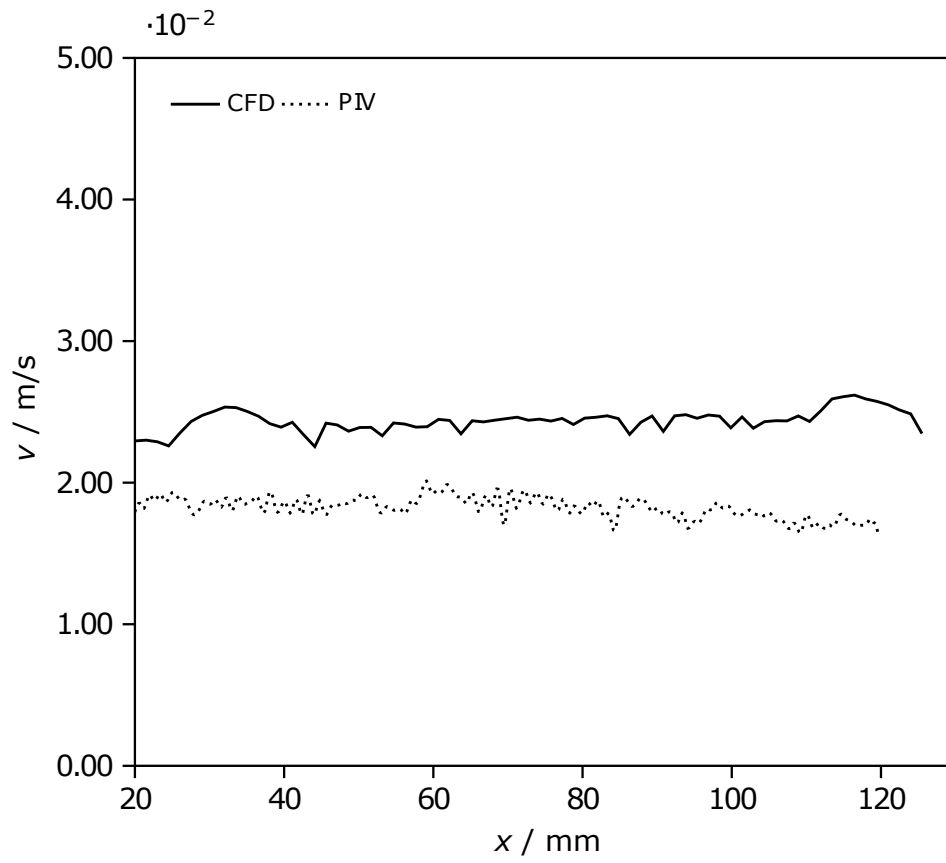


Figure A.17.: Post processed image of the velocity profile for  $Re = 2000$ .



**Figure A.18.:** Comparison between PIV and CFD values across a line above the center probe at  $Re = 200$ .



**Figure A.19.:** Comparison between PIV and CFD values across a line above the outer probe at  $Re = 200$ .

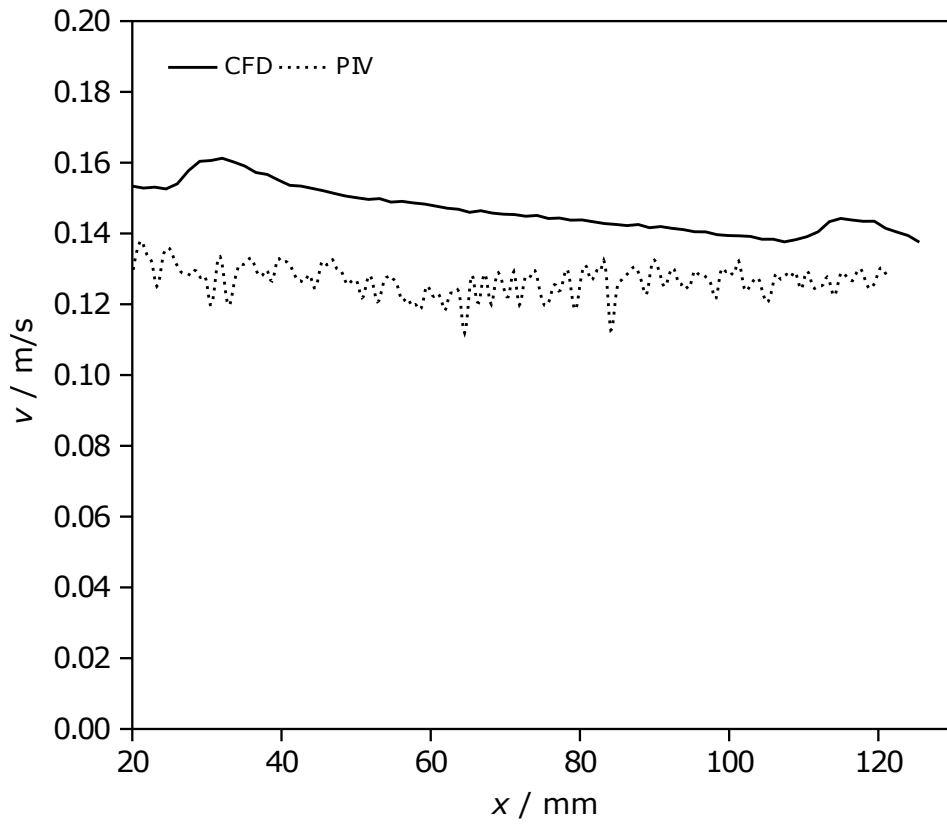


Figure A.20.: Comparison between PIV and CFD values across a line above the center probe at  $Re = 1000$ .

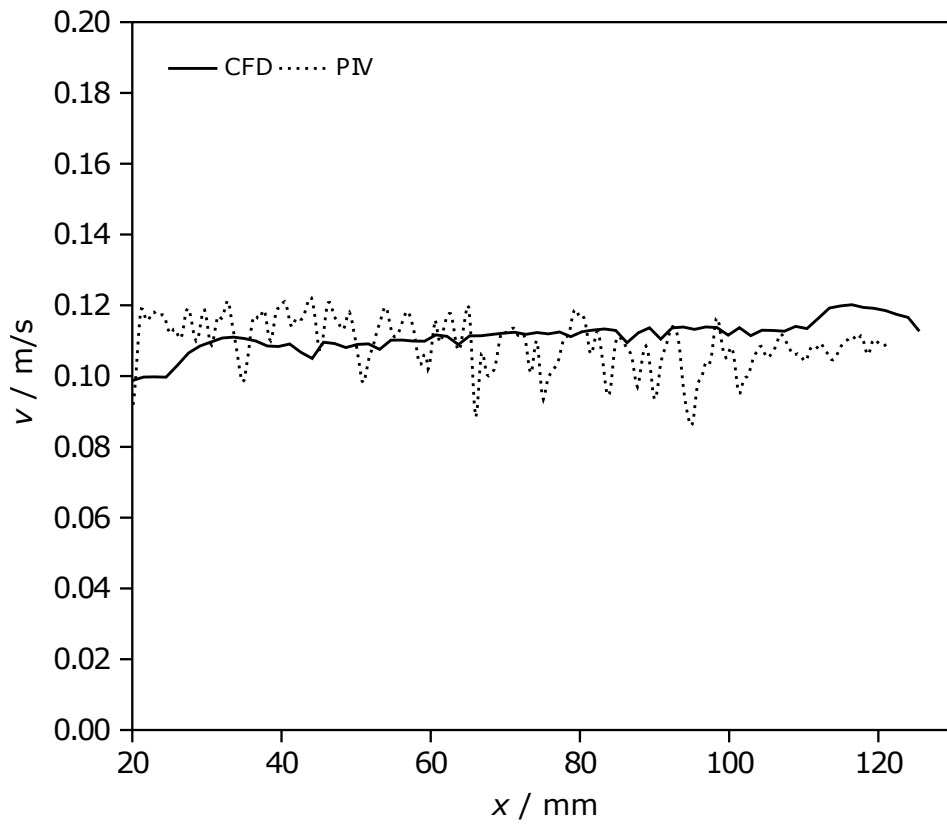
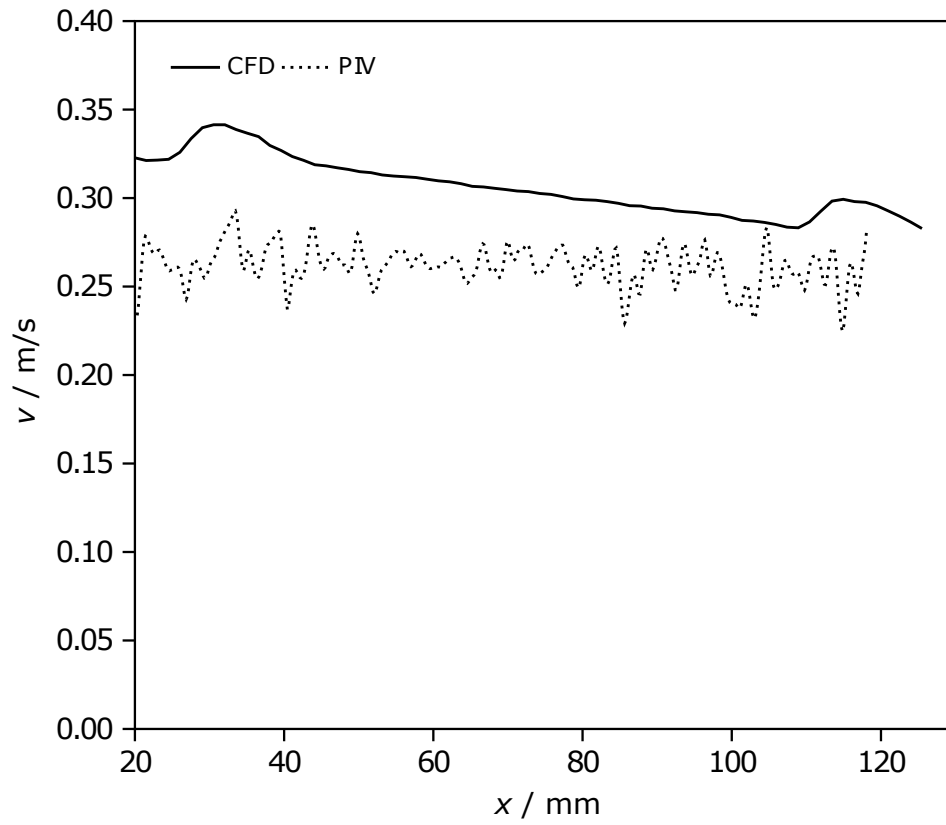
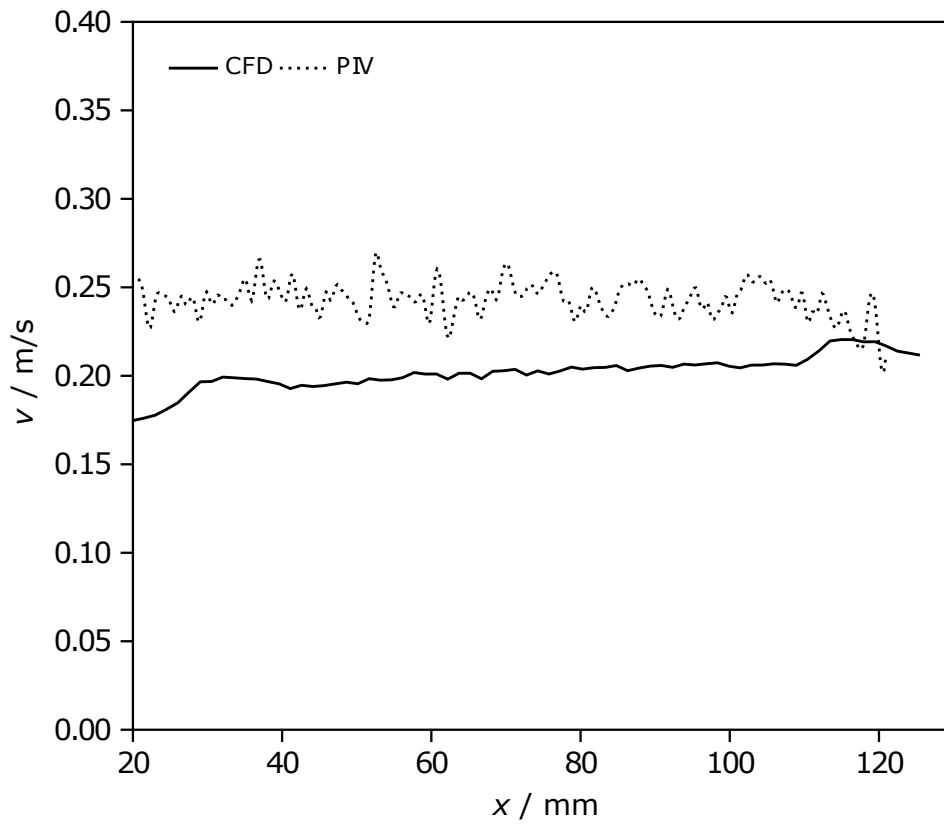


Figure A.21.: Comparison between PIV and CFD values across a line above the outer probe at  $Re = 1000$ .



**Figure A.22.:** Comparison between PIV and CFD values across a line above the center probe at  $Re = 2000$ .



**Figure A.23.:** Comparison between PIV and CFD values across a line above the outer probe at  $Re = 2000$ .



## B. Supplementary Information for Chapter 3

Analogues to Chapter A velocity and streamline profiles were generated for various Reynolds numbers using Ansys Fluent. However, the fluid is adapted to reflect the behavior of milk. Property data for milk can be found in Tab. B.1. The velocity profiles were generated by visualizing values on a plane section across the channel, while the stream line profiles encompass the whole fluid domain.

**Table B.1.:** Physical properties of milk.

<b>Parameter</b>	<b>Milk</b>
Density $\rho$ / kg/m <sup>3</sup>	1030
Viscosity $\eta$ / Pa·s	0.002

## B.1. Velocity Profiles

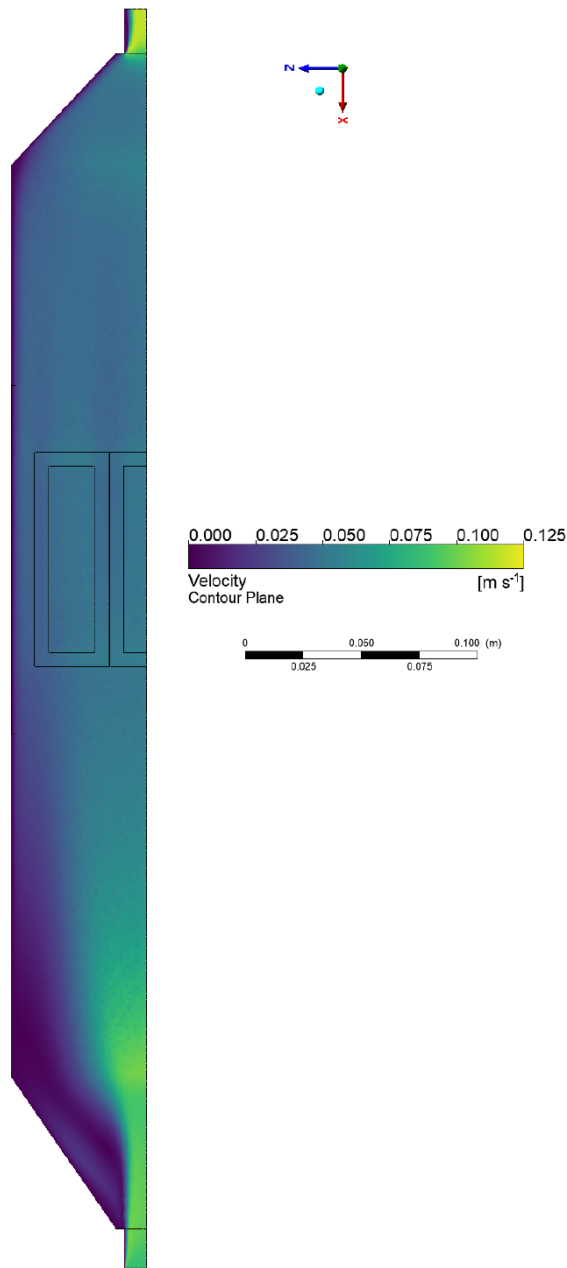


**Figure B.1.:** Velocity profile across channel width using milk as fluid (s. Tab. B.1) at  $Re = 200$ .

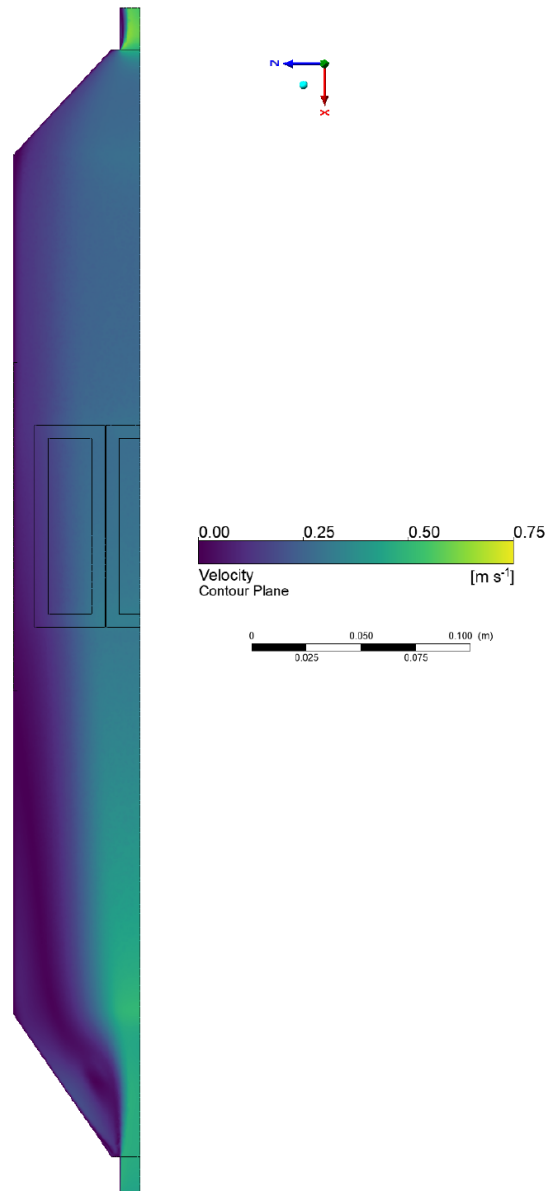


**Figure B.2.:** Velocity profile across channel width using milk as fluid (s. Tab. B.1) at  $Re = 1000$ .

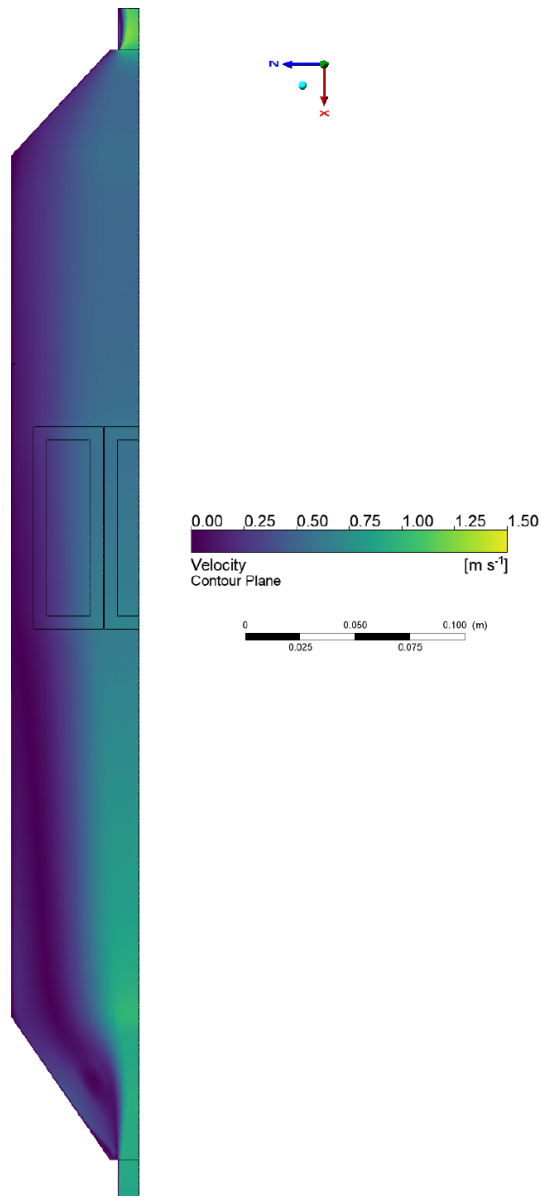


**Figure B.3.:** Velocity profile across channel width using milk as fluid (s. Tab. B.1) at  $Re = 2000$ .

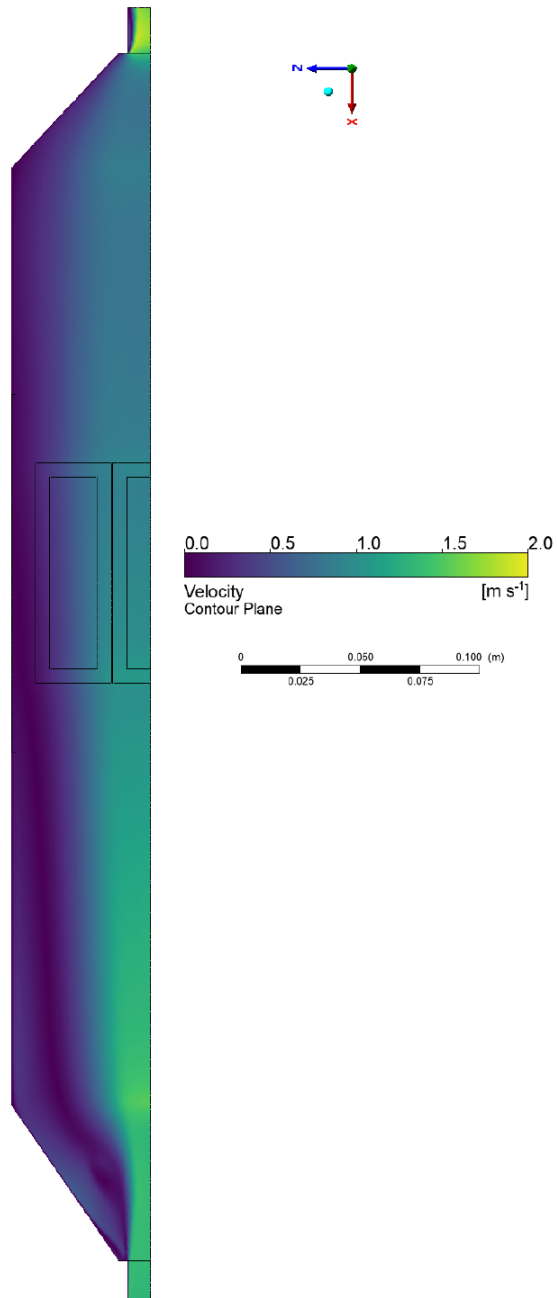


**Figure B.4.:** Velocity profile across channel width using milk as fluid (s. Tab. B.1) at  $Re = 3000$ .

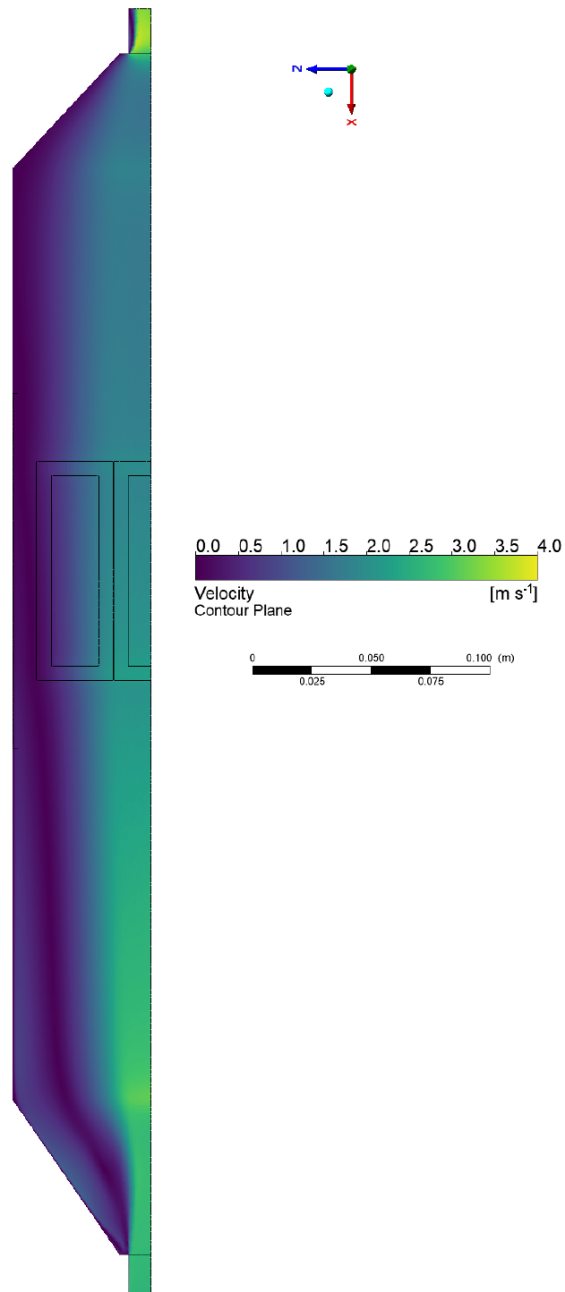


**Figure B.5.:** Velocity profile across channel width using milk as fluid (s. Tab. B.1) at  $Re = 6000$ .

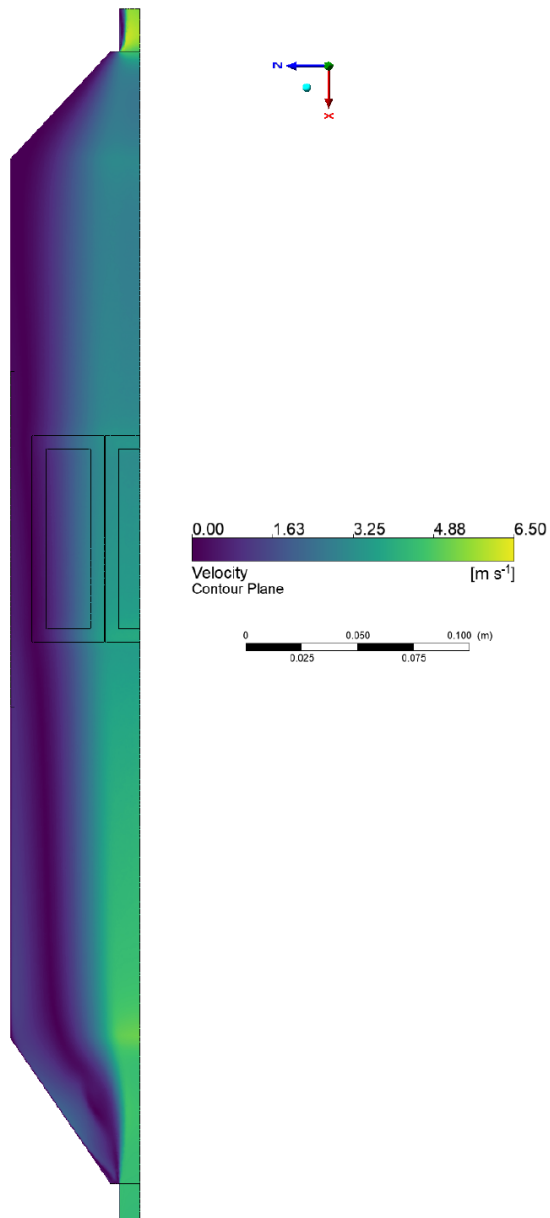


**Figure B.6.:** Velocity profile across channel width using milk as fluid (s. Tab. B.1) at  $\text{Re} = 10000$ .

## B.2. Streamlines

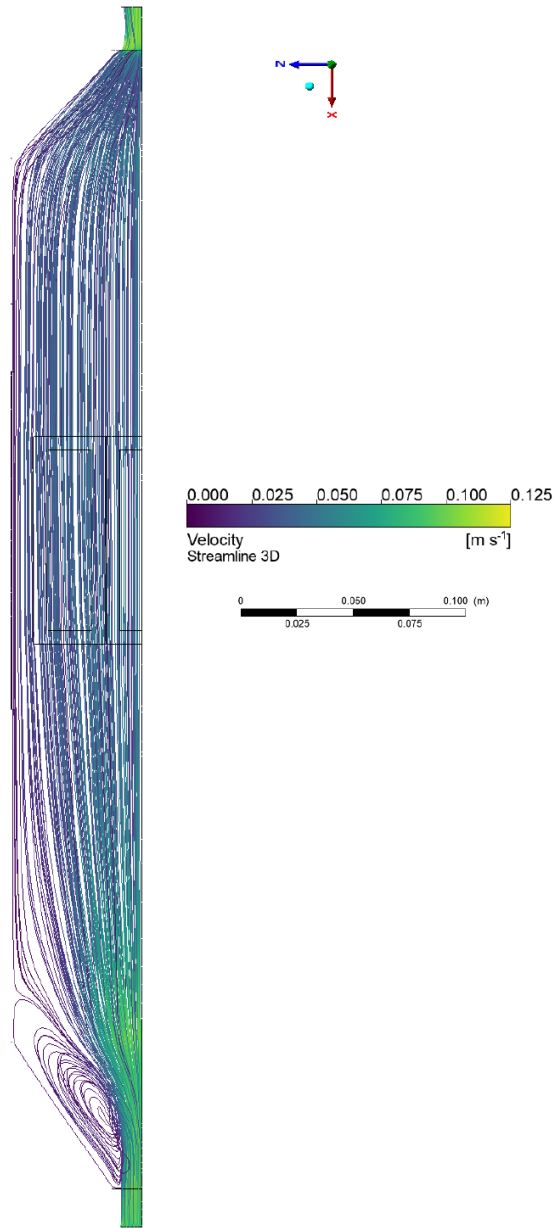


**Figure B.7.:** Velocity profile across channel width using milk as fluid (s. Tab. B.1) at  $Re = 200$ .

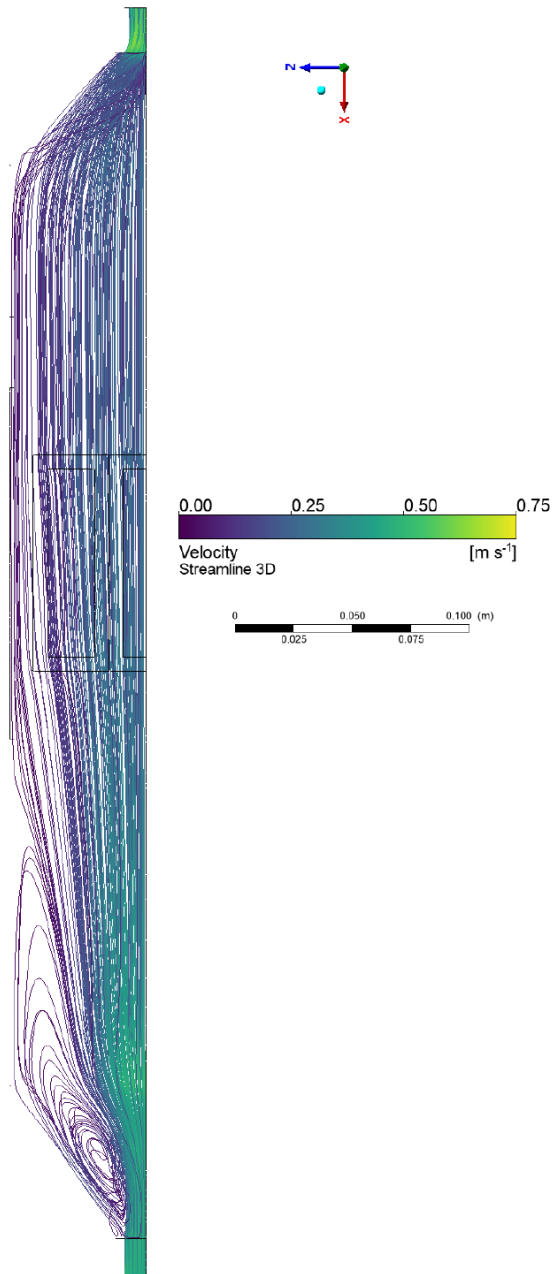


**Figure B.8.:** Streamline profile across channel width using milk as fluid (s. Tab. B.1) at  $Re = 1000$ .

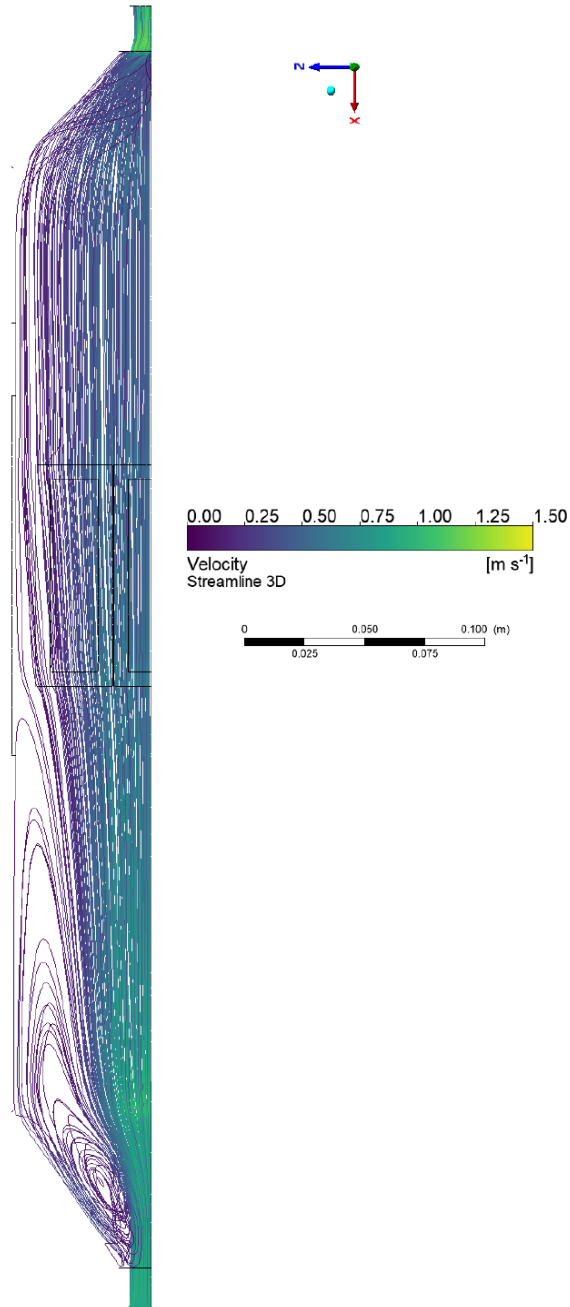


**Figure B.9.:** Streamline profile across channel width using milk as fluid (s. Tab. B.1) at  $Re = 2000$ .

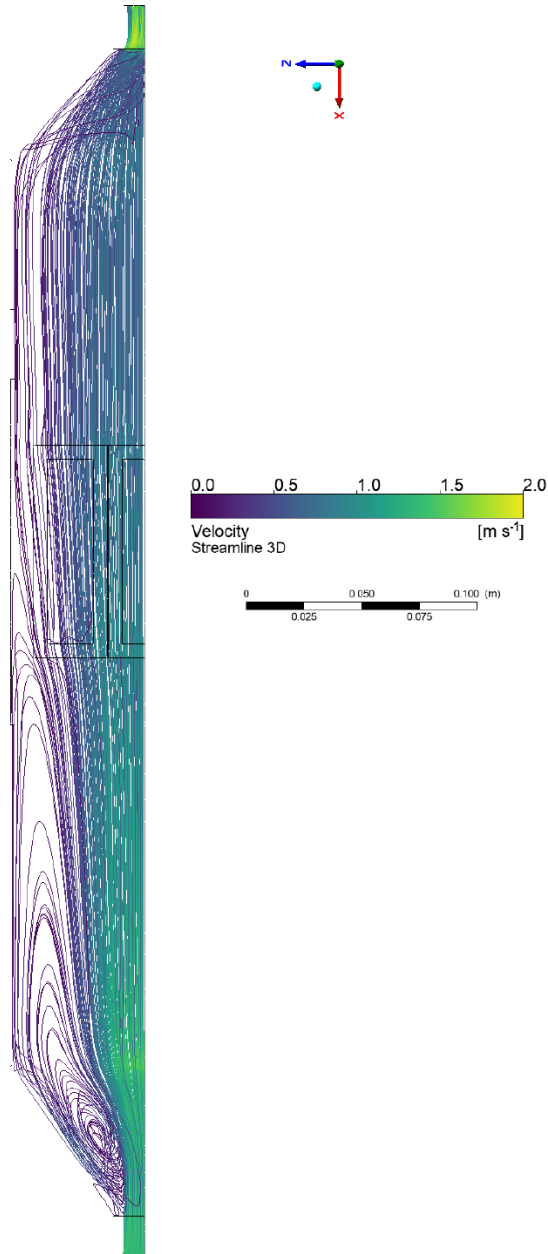


**Figure B.10.:** Streamline profile across channel width using milk as fluid (s. Tab. B.1) at  $Re = 3000$ .

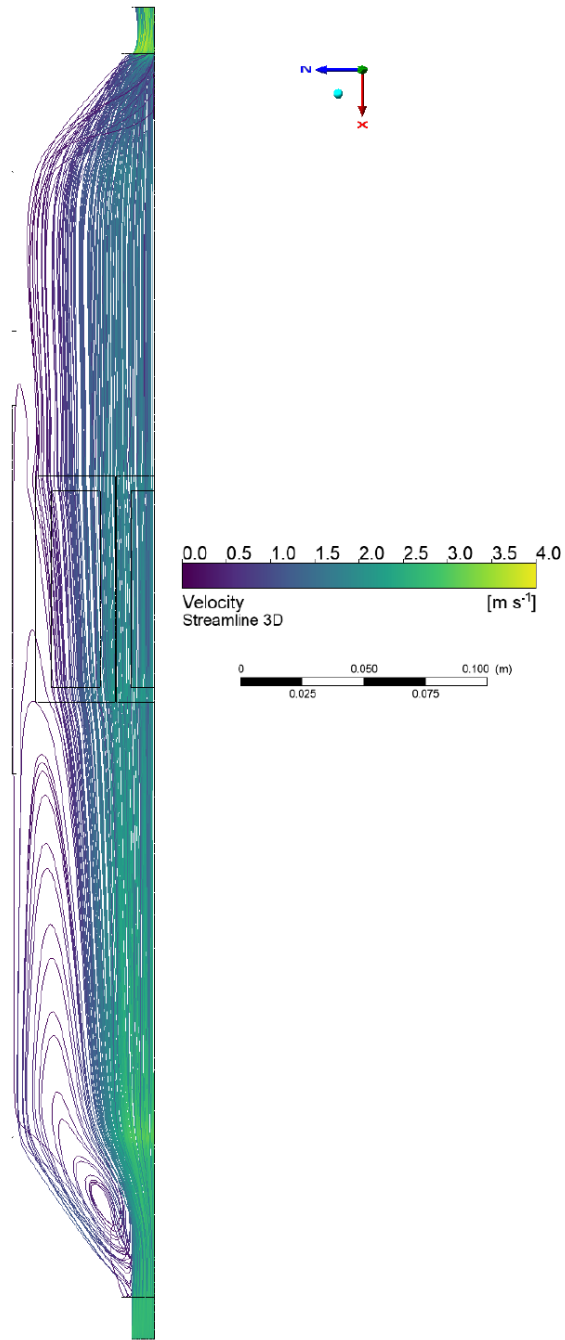


**Figure B.11.:** Streamline profile across channel width using milk as fluid (s. Tab. B.1) at  $Re = 6000$ .

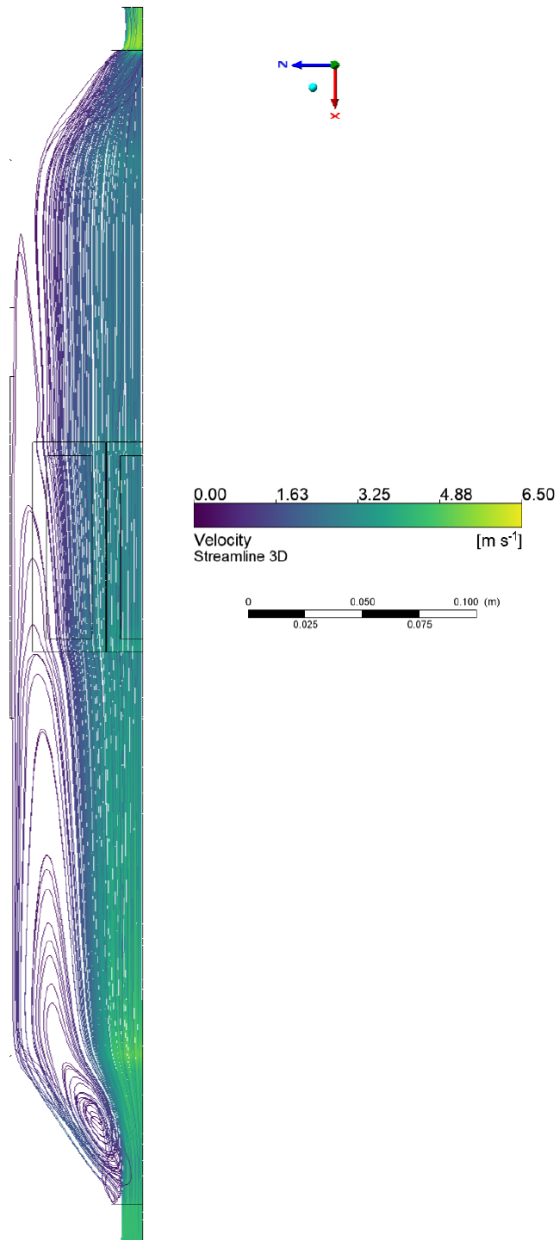


**Figure B.12.:** Streamline profile across channel width using milk as fluid (s. Tab. B.1) at  $\text{Re} = 10000$ .



## C. Supplementary Information for Chapter 4

**Table C.1.:** Used packages in the programming language Julia.

Package	Version
BangBang	v0.4.2
CSV	v0.10.14
DataFrames	v1.6.1
DelimitedFiles	v1.9.1
DifferentialEquations	v7.11.0
DiffEqParamEstim	v2.2.0
ForwardDiff	v0.10.36
Interpolations	v0.15.1
LineSearches	v7.2.0
LsqFit	v.015.0
Optim	v1.9.2
Optimization	v3.19.3
Parameters	v0.12.3
Plots	v1.40.1
Polynomials	v4.0.8
RecursiveArrayTools	v2.38.10
Revise	v3.5.14
Statistics	v1.10.0
SymbolicRegression	v0.24.5
SymbolicUtils	v1.4.0
Trapz	v2.0.3

**Table C.2.:** Option settings for the symbolic regression.

setting	Value
binary operators	+,-,*,/
unary operators	exp, log
number of operators	7
number of populations	25

**Table C.3.:** Optimization parameters and model accuracy of the empirical model.

$c_{\text{wpc}}$ $\text{kg m}^{-3}$	$\dot{q}$ $\text{kW}/(\text{m}^2)$	$R^2$	$A$ $\text{g m}^{-2}$	$B$ $\times 10^{-4} \text{ s}^{-1}$
2	45	0.975	59.023	1.313
2	55	1.000	65.101	1.349
2	65	0.999	117.977	0.646
4	45	0.867	55.241	1.547
4	55	0.982	220.200	0.484
4	65	0.839	237.137	1.562
6	45	0.796	45.566	5.205
6	55	0.988	237.137	0.698
6	65	0.906	237.137	2.004

**Table C.4.:** List of optimization parameters for all operating conditions of the mechanistic model.

$c_{\text{WPC}}$ $\text{kg m}^{-3}$	$\dot{q}$ $\text{kW}/(\text{m}^2)$	$p_1$ $\text{s}^{-1}$	$p_2$
2	45	6.106	3.230e-1
2	55	3.388	4.744e-1
2	65	0.493	8.047e-1
4	45	3.246	1.057e-5
4	55	4.712	5.629e-1
4	65	1.803	7.843e-1
6	45	8.401	2.299e-5
6	55	4.654	5.805e-1
6	65	1.789	7.533e-1

**Table C.5.:** List of NRMSE for all operating conditions.

$c_{\text{WPC}}$ $\text{kg m}^{-3}$	$\dot{q}$ $\text{kW}/(\text{m}^2)$	NRMSE			
		$(m_{\text{f,exp}}, m_{\text{f,emp}})$	$(m_{\text{f,exp}}, m_{\text{f,mech}})$	$(m_{\text{f,emp}}, m_{\text{f,mech}})$	$(R_{\text{f,exp}}, R_{\text{f,mech}})$
2	45	0.050	0.047	0.021	0.071
2	55	0.002	0.016	0.018	0.144
2	65	0.014	0.011	0.006	0.262
4	45	0.134	0.134	0.051	0.108
4	55	0.042	0.043	0.007	0.168
4	65	0.172	0.157	0.018	0.081
6	45	0.164	0.174	0.048	0.230
6	55	0.044	0.049	0.008	0.182
6	65	0.127	0.109	0.021	0.198

---

**Table C.6.:** Table with experimental and validation data.

$c_{wpc}$ $\text{g L}^{-1}$	$\dot{q}$ $\text{kW}/(\text{m}^2)$	$T_{w,0}$ K	$T_{w,\text{boil}}$ K
2	45	360.1	399.1
4	45	360.0	404.0
6	45	358.4	400.3
2	55	365.1	406.1
4	55	363.0	407.0
6	55	363.0	398.1
2	65	376.1	419.1
4	65	377.1	405.1
6	65	379.1	405.1
Validation Set			
5	50	365.1	403.1
3	60	373.1	406.1
10	65	373.1	412.1



# Detailed Contributor Roles Taxonomy

This chapter provides a detailed contributor roles taxonomy according to Allen, O'Connell, and Kiermer [77] of the publications and manuscripts redrafted in Chapters 2-4. The remaining chapters were written by the author of the thesis, using content of the mentioned manuscripts.

## Chapter 2: Calcium Sulfate fouling

Philipp Pelz: conceptualization; formal analysis; methodology; project administration; validation; visualization; writing - original draft; writing - review & editing

Julian Schulz: experimental work

Poorya Mavaddat: experimental work

Conrad Meyer: review & editing

Katharina Jasch: review & editing

Stephan Scholl: review & editing

Erik von Harbou: funding acquisition; resources; supervision; writing - review & editing

Hans-Jörg Bart: funding acquisition; resources; supervision; writing - review & editing

## Chapter 3: WPC fouling

Philipp Pelz: conceptualization; formal analysis; methodology; project administration; software; validation; visualization; writing - original draft; writing - review & editing

Jonas Noß: experimental work

Erik von Harbou: funding acquisition; resources; supervision; writing - review & editing

Hans-Jörg Bart: funding acquisition; resources; supervision; writing - review & editing

## Chapter 4: Modeling WPC fouling

Philipp Pelz: conceptualization; formal analysis; methodology; project administration; software; validation; visualization; writing - original draft; writing - review & editing

Paul Egorov: software, data curation; validation

Julian Schulz: data curation; validation

Dennis Lukas: data curation; validation

Sarah Brune: resources

Rebekka Biedendieck: resources

Erik von Harbou: funding acquisition; resources; supervision; writing - review & editing

Hans-Jörg Bart: funding acquisition; resources; supervision; writing - review & editing



# Publication List

The following list of scientific works were published by the author as part of his research.

## Journal Articles

- C. Meyer, P.-L. Pelz, K. Jasch, H.-J. Bart, E. von Harbou, and S. Scholl, “A screening apparatus for comparing the fouling resistance of heat exchanger surfaces,” *Chemie Ingenieur Technik*, 2024. DOI: 10.1002/cite.202300210.
- P. Pelz, J. Noß, E. von Harbou, and H.-J. Bart, “Whey protein fouling on polymeric heat exchangers,” *Heat Transfer*, vol. 53, no. 6, pp. 2948–2964, 2024. DOI: 10.1002/htj.23070.
- P. Pelz, J. Schulz, P. Mavaddat, C. Meyer, K. Jasch, S. Scholl, E. von Harbou, and H.-J. Bart, “Comparing calcium sulfate fouling on polymeric and metal heat transfer surfaces,” *Chemie Ingenieur Technik*, 2024. DOI: 10.1002/cite.202300216.

## Lectures and Speeches

- P. Pelz, E. von Harbou, and H.-J. Bart, Conference Lecture, Topic: “Whey protein fouling on polymeric heat exchangers”, Presented at: Heat Transfer and Fluid Flow 2024, Barcelona, Spain, Aug. 24, 2024.
- P. Pelz, C. Meyer, A. Klinkert, K. Jasch, H.-J. Bart, and S. Scholl, Conference Lecture, Topic: “Methods for the standardized generation and quantification of fouling in heat exchangers”, Presented at: Ausstellungstagung für chemisches Apparatewesen, Frankfurt a.M., Germany, Jun. 10, 2024.

## Conference Posters

- P. Pelz, J. Noß, E. von Harbou, and H.-J. Bart, “Fouling Of Whey Protein Concentrate (WPC) On Polymeric Heat Exchangers,” Presented at: European Congress of Chemical Engineering (ECCE), 2023-09-17, 2023.
- P. Pelz, E. von Harbou, and H.-J. Bart, “Fouling of calcium sulphate on polymeric heat exchangers,” Presented at: Jahrestreffen der DECHEMA-Fachgruppen Computational Fluid Dynamics und Wärme- und Stoffübertragung, 2023-03-06, 2023.



# Supervised Student Theses

The following student theses were prepared under the supervision of the author.

- J. Vida, “Construction and commissioning of a screening apparatus to characterize the fouling of salt and wpc solutions during heat transfer,” Student Research Project, Laboratory of Reaction and Fluid Process Engineering, RPTU Kaiserslautern, Germany, 2023.
- J. Noss, “Quantifying deposits of aqueous whey protein solutions on polymeric heat exchanger surfaces,” Student Research Project, Laboratory of Reaction and Fluid Process Engineering, RPTU Kaiserslautern, Germany, 2023.
- J. Schulz, “Quantifying deposits of calcium sulfate solutions on polymeric heat exchanger surfaces,” Student Research Project, Laboratory of Reaction and Fluid Process Engineering, RPTU Kaiserslautern, Germany, 2022.
- C. Zipp, “Simulating the flow behavior of water-based solutions in a channel using ansys fluent,” Bachelor Thesis, Laboratory of Reaction and Fluid Process Engineering, RPTU Kaiserslautern, Germany, 2021.
- J. Dieing, “Experimental validation of a flow channel cfd simulation using a particle imaging velocimetry laser,” Master Thesis, Laboratory of Reaction and Fluid Process Engineering, RPTU Kaiserslautern, Germany, 2023.
- P. Egorov, “Modeling fouling behaviour of polymeric heat exchangers,” Bachelor Thesis, Laboratory of Reaction and Fluid Process Engineering, RPTU Kaiserslautern, Germany, 2024.
- P. Mavaddat, “Quantifying calcium sulfate fouling under degassed and evaporating operating conditions,” Master Thesis, Laboratory of Reaction and Fluid Process Engineering, RPTU Kaiserslautern, Germany, 2024.
- T. Keslov, “Quantifying the effects of particulate fouling on crystallization fouling in supersaturated calcium sulfate solutions,” Bachelor Thesis, Laboratory of Reaction and Fluid Process Engineering, RPTU Kaiserslautern, Germany, 2024.
- D. Lukas, “Comparing whey protein fouling in heat flux constant and temperature constant heat exchangers,” Master Thesis, Laboratory of Reaction and Fluid Process Engineering, RPTU Kaiserslautern, Germany, 2024.
- F. Herrada, “Simulating the flow behavior of water-based polymer dispersions in a channel using ansys fluent,” Student Research Project, Laboratory of Reaction and Fluid Process Engineering, RPTU Kaiserslautern, Germany, 2022.

- F. Bartzack, “Determining fouling behaviour of a vinylacetate-ethylene dispersion on polymeric and metallic heat exchanger surfaces,” Bachelor Thesis, Laboratory of Reaction and Fluid Process Engineering, RPTU Kaiserslautern, Germany, 2021.
- C. Fuchs, “Construction and commissioning of a screening apparatus for measuring fouling-prone material systems,” Bachelor Thesis, Laboratory of Reaction and Fluid Process Engineering, RPTU Kaiserslautern, Germany, 2022.
- E. Friedrich, “Beitrag zur maßstabsvergrößerung der veresterung von pyrolyseölen mit höheren alkoholen,” Master Thesis, Laboratory of Reaction and Fluid Process Engineering, RPTU Kaiserslautern, Germany, 2021.

# Acknowledgement

The author gratefully acknowledges the Federal Ministry for Economic Affairs and Climate Action of Germany (BMWK) (project SAMARA, FKZ 03 EN2007J) for financial support.

# Philipp Pelz



## Curriculum Vitae

---

### Work Experience

---

- 01/2021 - 10/2025    **Scientific Assistant**  
Laboratory of Reaction and Fluid Process Engineering  
University of Kaiserslautern-Landau, Kaiserslautern, Germany
- 10/2018 – 01/2021    **Process Engineer**  
Procter & Gamble, Groß-Gerau, Germany
- 05/2018 – 10/2018    **Consultant**  
InnoScripta GmbH, Munich, Germany

---

### Education

---

- 03/2013 – 03/2018    **Technische Universität Berlin**  
M.Sc. Energy and Process Engineering
- 07/2009 – 03/2013    **Technische Universität Berlin**  
B.Sc. Energy and Process Engineering
- 07/2000 – 07/2008    **Evangelisch-Stiftisches Gymnasium Gütersloh**  
University entrance qualification